Fundamental Studies of the Durability of Materials for Interconnects in Solid Oxide Fuel Cells

Final Report

Principal Investigators:
Frederick S. Pettit (pettit@engr.pitt.edu)
Gerald H. Meier (ghmeier@engr.pitt.edu)

Report Date: 30 September, 2006

DOE Award: DE FC26 02NT41578

Submitted by:
Department of Materials Science & Engineering
848 Benedum Hall
University of Pittsburgh
Pittsburgh, PA 15261

Subcontract Information:

Jack L. Beuth
Department of Mechanical Engineering
Carnegie Mellon University
5000 Forbes Avenue
Pittsburgh, PA 15213-3890
Phone: (412) 268-3873; Fax: (412) 268-3348
E-mail: (beuth@andrew.cmu.edu)

James R. Rakowski
ATI Allegheny Ludlum
Technical and Commercial Center
Alabama and Pacific Avenues
Brackenridge, PA 15014
Phone: (724) 226-6283; Fax:(724) 226-5067;
Email: JRakowski@AlleghenyLudlum.com

Bruce Kang
West Virginia University
Mechanical & Aerospace Engineering
P.O. Box 6106
Morgantown, WV 26506-6106
Phone: (304) 293-3111 x2316; Fax: (304) 293-6689
Email: bruce.kang@mail.wvu.edu

ABSTRACT

Ferritic stainless steels are a leading candidate material for use as an SOFC interconnect, but have the problem of forming volatile chromia species that lead to cathode poisoning. This project has focused both on optimization of ferritic alloys for SOFC applications and evaluating the possibility of using alternative materials.

The initial efforts involved studying the oxidation behavior of a variety of chromia-forming ferritic stainless steels in the temperature range 700-900°C in atmospheres relevant to solid oxide fuel cell operation. The alloys exhibited a wide variety of oxidation behavior based on composition.

A method for reducing the vaporization is to add alloying elements that lead to the formation of a thermally grown oxide layer over the protective chromia. Several commercial steels form manganese chromate on the surface. This same approach, combined with observations of TiO_2 overlayer formation on the chromia forming, Ni-based superalloy IN 738, has resulted in the development of a series of Fe-22 Cr-X Ti alloys (X=0–4 wt%). Oxidation testing has indicated that this approach results in significant reduction in chromia evaporation. Unfortunately, the Ti also results in accelerated chromia scale growth.

Fundamental thermo-mechanical aspects of the durability of solid oxide fuel cell (SOFC) interconnect alloys have also been investigated. A key failure mechanism for interconnects is the spallation of the chromia scale that forms on the alloy, as it is exposed to fuel cell environments. Indentation testing methods to measure the critical energy release rate (G_c) associated with the spallation of chromia scale/alloy systems have been evaluated. This approach has been used to evaluate the thermomechanical stability of chromia films as a function of oxidation exposure.

The oxidation of pure nickel in SOFC environments was evaluated using thermogravimetric analysis (TGA) to determine the NiO scaling kinetics and a four-point probe was used to measure the area-specific resistance (ASR) to estimate the electrical degradation of the interconnect. In addition to the baseline study of pure nickel, steps were taken to decrease the ASR through alloying and surface modifications. Finally, high conductivity composite systems, consisting of nickel and silver, were studied. These systems utilize high conductivity silver pathways through nickel while maintaining the mechanical stability that a nickel matrix provides.

3

TABLE OF CONTENTS

LIST OF GRAPHICAL MATERIALS

Figure 1.   Schematic diagram showing the apparatus to cyclically oxidize coupon specimens in gases with defined and controlled amounts of water vapor in air at a total pressure of 1 atm.

Figure 2.   Schematic diagram of the TGA apparatus for continuous measurement of mass during exposure.

Figure 3.   Schematic diagram of the dual atmosphere apparatus.

Figure 4.   Schematic diagram of the ASR apparatus and cartoon showing a close up of the specimen and electrode/lead attachments.

Figure 5.   Schematic diagram showing possible ways of using silver as a conducting path through nickel interconnects.

Figure 6.   Schematic diagram of dual atmosphere apparatus for exposing tubular specimens.

Figure 7.   Effect of titanium on the mechanical properties of a model Fe-22Cr alloy.

Figure 8.   Effect of titanium on the linear coefficient of thermal expansion of a model Fe-22Cr alloy.

Figure 9.   TGA data for Fe-Cr-Ti alloys, Crofer, and E-Brite at 900˚C in dry and moist atmospheres.

Figure 10.   Cyclic oxidation data for Fe-Cr-Ti alloys and Crofer, at 800˚C in dry and moist atmospheres.

Figure 11.   Cross – sectional and surface SEM micrographs of alloys exposed for 96 hrs at 900^oC in dry air containing 0.004% (a&b), 0.84% (c&d), 1.65% (e&f), 2.78% (g&h), and 3.98% (i&j) titanium.

Figure 12.   Long-term oxidation test results at 760°C in ambient air for Fe-22Cr alloys with added titanium (E-BRITE sample included for a reference).

Figure 13.   Long-term oxidation test results at 760°C in air containing 7% water vapor for Fe-22Cr alloys with added titanium (E-BRITE sample included for a reference).

Figure 14.   Comparison of weight gains after 3,000 hours at 760°C for Fe-22Cr alloys with added titanium – ratio of terminal weight gain in air containing 7% added water vapor to terminal weight gain in ambient air.

INTRODUCTION

Solid oxide fuel cells provide a potential way to generate electricity with high efficiency and low pollution. The operating principles of fuel cells have been known for over 100 years and low-temperature fuel cells provided the electric power on all the Gemini and Apollo spacecraft. However, fuel cells have not achieved widespread commercial use for a number of economic and technical reasons.

One of the most important technical challenges for solid oxide fuel cells, which operate in the temperature range 700°-900°C, is the design of interconnects (current collectors). These components, in addition to electrically connecting individual cells in a stack, must separate the anode compartment of one cell from the cathode compartment of the adjacent cell. This means that one side of an interconnect is exposed to the fuel, typically hydrogen or hydrocarbons in which the oxygen partial pressure is low, and the other side is exposed to the oxidant, which is typically air with some amount of water vapor. Metallic alloys have many attractive features as potential interconnect materials.

Oxidation resistant alloys are designed to form one of three protective oxides: alumina, silica, or chromia. Of these, the electrical resistivities of alumina and silica are much too high for interconnect applications. For metallic interconnects, interconnect system resistance can be greatly increased by oxide layer thickening and spallation. For chromia formers, evaporation of the chromia scale can severely degrade cathode performance. Thus chromia scale growth, scale spallation and scale evaporation are the three principal "failure mechanisms" for interconnects forming chromia scales on their surfaces. Because they are coupled, alloy changes to address one failure mechanism can affect one or more of the other failure mechanisms, making alloy design a complex task.

EXECUTIVE SUMMARY

This project had four objectives:

- To develop mechanism-based evaluation procedures for the stability of SOFC interconnect materials and to use these procedures to study and modify a group of alloys, which have already been identified as candidate interconnect materials, i.e. ferritic stainless steels.
- To study fundamental aspects underlying the thermomechanical behavior of interconnect materials and develop accelerated testing protocols. (CMU Subcontract)
- To investigate the potential for the use of "new" metals as interconnect materials.
- Development of a durable, conductive ceramic/metal (cermet) material, suitable for long-term use as a contacting material in the cathode chamber of SOFC. (WVU Subcontract)

The program consisted of four major tasks aligned with its four objectives.

Task 1: Mechanism-based Evaluation Procedures

A variety of chromia-forming interconnect alloys were subjected to thermal cycling in air, in simulated anode gas (Ar-H_2-H_2O) and with simultaneous exposure to air on one side and simulated anode gas on the other. Exposure temperatures range from 700°C to 900°C. Oxidation kinetics were tracked by mass change measurements and corresponding changes in oxide scale resistances were measured. Exposed specimens were examined in cross-section by scanning electron microscopy (SEM) to document changes in structure with exposure.

Methods were studied to slow the growth of chromia scales on Cr and Ferritic alloys upon exposure to oxidizing gases. The effect of alloying additions (e.g. Mn, Ti) to ferritic steels to reduce harmful CrO_3 and $CrO_2(OH)_2$ evaporation by forming a sealing outer layer over the chromia scale was evaluated. The ability of chromite coatings to reduce evaporation from chromia-forming interconnect alloys was investigated.

Task 2: Fundamental Aspects of Thermomechanical Behavior (CMU)

Understanding the resistance of growing chromia scales to spallation requires a fundamental understanding of the mechanics of chromia adhesion. From a fracture mechanics standpoint, the adherence of protective oxide scales to alloy substrates is governed by 1) the stored elastic energy in the scale, which drives delamination and 2) the fracture toughness of the alloy/oxide interface, which quantifies the resistance to fracture.

The stored elastic energy in the scale is increased by increases in the scale thickness and increases in the residual stress in the scale. In this task, x-ray diffraction (XRD) was used to measure stresses in chromia films formed on pure chromium and chromia-forming alloys after the exposures described for Task 1.

An indentation test was also used to measure the fracture toughness of chromia/alloy interfaces for the same exposures. In the test, the chromia scale is penetrated by the indenter and the plastic deformation of the underlying substrate induces compressive radial strains in the substrate. These strains are transferred to the coating and the associated coating stress drives the extension of a roughly axisymmetric interface

crack. The interfacial toughness can be determined from the results of a mechanics analysis of the indentation problem and a measurement of the delamination radius.

Task 3: Alternative Material Choices

Metallic materials other than chromia-formers are being considered for use as low temperature SOFC interconnects. Experiments similar to those described for Task 1 were performed on pure Ni. Its only oxide, NiO, has no vapor species with high partial pressures and it has a higher electrical conductivity than chromia. Also, NiO should not even form in the anode gas.   The doping of the NiO scale with SrO or CeO_2 was investigated as a way to slow the growth rate. Finally, the use of Ag conducting paths through Ni interconnects was studied.

Task 4: Development of Durable Contacting Material (WVU)

At present, candidate cermets have been developed by ball-milling of various oxide powders with silver or silver-oxide powders, followed by dry-pressing and sintering in a high-temperature furnace. The cermets were evaluated by SEM to determine the compatibility of silver with the candidate oxide materials, as well as the dispersion of silver throughout the cermet. The cermets were also tested for hardness/ductility using Vickers hardness testing. Conductivity was evaluated using a simple multimeter test to evaluate the resistance of the cermet. A thermomechanical analyzer was also used to evaluate the CTE of the materials to verify compatibility with other SOFC components. Lastly, cermets were placed in a high-temperature furnace to be exposed to the SOFC operating temperature (~800°C), while a high-volume air flow was introduced to simulate the cathode environment of the SOFC.

All measurements, conductivity, hardness, and mass were taken before and after exposure to the simulated cathode environment in order to make a determination of the effects on the cermet material.

Major accomplishments of this project include**:**
- Determined that even very small concentrations of Al or Si in ferritic alloys result in the formation of internal films with high electrical resistivity.
- Discovered that exposure under some fuel cell operating conditions (e.g. water vapor) accelerates sigma phase formation in some ferritic stainless steels. Alloy purity is also important for retarding sigma-phase formation.
- Discovered that it is possible to modify a ferritic steels to form an overlayer of TiO_2 which suppresses the evaporation from the underlying chromia scale.
- Determined that the growth rate of chromia on ferritic alloys can be greatly suppressed by surface doping with CeO_2.
- Adapted an indentation technique for measuring interfacial fracture toughnesses of oxides formed on interconnects and coatings applied to interconnects.
- Found that the growth rate of NiO can be slowed significantly by surface doping with SrO or CeO_2.
- Found that, unlike ferrous alloys, the oxidation of Ni is not altered significantly under dual atmosphere conditions.
- Showed that Ni interconnects containing Ag conduction paths are feasible.
- Completed three M.S. theses and six Senior Projects.

PROJECT DESCRIPTION

Objectives

- To develop mechanism-based evaluation procedures for the stability of SOFC interconnect materials and to use these procedures to study and modify a group of alloys, which have already been identified as candidate interconnect materials, i.e. ferritic stainless steels.
- To study fundamental aspects underlying the thermomechanical behavior of interconnect materials and develop accelerated testing protocols. (CMU Subcontract)
- To investigate the potential for the use of "new" metals as interconnect materials.
- To develop a durable, conductive ceramic/metal (cermet) material, suitable for long-term use as a contacting material in the cathode chamber of SOFC. (WVU Subcontract)

Approach

The program consists of four major tasks aligned with its four objectives.

Task 1: Mechanism-based Evaluation Procedures

A variety of commercial chromia-forming interconnect alloys have been subjected to thermal cycling in air, in simulated anode gas ($Ar-H_2-H_2O$) and with simultaneous exposure to air on one side and simulated anode gas on the other. Combined exposures have been shown at PNNL to often yield different behavior than exposures with the same gas on both sides of the specimen. Exposure temperatures range from 700°C to 900°C. Oxidation kinetics have been tracked by mass change measurements and corresponding changes in oxide scale resistances have been measured. Exposed specimens have been examined in cross-section by scanning electron microscopy (SEM) to document changes in structure with exposure.

Methods have been studied to slow the growth of chromia scales on Cr and ferritic alloys with exposure, to decrease the contribution of the scale to interconnect resistance. The effect of alloying additions (e.g. Mn, Ti) to ferritic steels to reduce harmful CrO_3 and $CrO_2(OH)_2$ evaporation by forming a sealing outer layer over the chromia scale has been evaluated. The ability of chromite coatings to reduce evaporation from chromia-forming interconnect alloys has also been investigated.

Task 2: Fundamental Aspects of Thermomechanical Behavior (CMU)

Understanding the resistance of growing chromia scales to spallation requires a fundamental understanding of the mechanics of chromia adhesion. From a fracture mechanics standpoint, the adherence of protective oxide scales to alloy substrates is governed by 1) the stored elastic energy in the scale, which drives delamination and 2) the fracture toughness of the alloy/oxide interface, which quantifies the resistance to fracture.

The stored elastic energy in the scale is increased by increases in the scale thickness (which can be measured by cross-section SEM) and increases in the residual

stress in the scale. In this task, x-ray diffraction (XRD) has been used to measure stresses in chromia films formed on pure chromium and chromia-forming alloys after the exposures described for Task 1.

An indentation test has also been used to quantify the fracture toughness of chromia/alloy interfaces for the same exposures. In the test, the chromia scale is penetrated by the indenter and the plastic deformation of the underlying substrate induces compressive radial strains in the substrate. These strains are transferred to the scale and the associated scale stress drives scale spallation. Scales can spall as intact coatings, with an interface crack propagating radially outward, or spallation can occur as the debonding of small flakes, with the density of flaking decreasing with distance from the indent. The interfacial toughness can be estimated from the results of a mechanics analysis of the indentation problem and a measurement of the extent of the delamination failures.

Task 3: Alternative Material Choices

Metallic materials other than chromia-formers are being considered for use as low temperature SOFC interconnects. Experiments similar to those described for Task 1 have been performed on pure Ni. Its only oxide, NiO, has no vapor species with high partial pressures and it has a higher electrical conductivity than chromia. Also, NiO should not even form in the anode gas.   Also, the doping of the NiO scale with SrO or CeO_2 has been investigated as a way to slow the growth rate. Finally, the use of Ag conducting paths through Ni interconnects has been studied.

Task 4: Development of Durable Contacting Material (WVU)

At present, candidate cermets have been developed by ball-milling of various oxide powders with silver or silver-oxide powders, followed by dry-pressing and sintering in a high-temperature furnace. The cermets have been evaluated by SEM to determine the compatibility of silver with the candidate oxide materials, as well as the dispersion of silver throughout the cermet. The cermets have also been tested for hardness/ductility using Vickers hardness testing. Conductivity has been evaluated using a simple multimeter test to evaluate the resistance of the cermet. A thermomechanical analyzer has also been used to evaluate the CTE of the materials to verify compatibility with other SOFC components. Lastly, cermets have been placed in a high-temperature furnace to be exposed to the SOFC operating temperature (~800˚C), while a high-volume air flow is introduced to simulate the cathode environment of the SOFC.

All measurements, conductivity, hardness, and mass were taken before and after exposure to the simulated cathode environment in order to make a determination of the effects on the cermet material.

EXPERIMENTAL

Task 1
Cyclic Oxidation

The cyclic oxidation of a range of commercial ferritic stainless steels has been evaluated under a range of conditions pertinent to fuel cell operation. The alloys were: (Nominal compositions in wt%)

- E-BRITE (Fe-26 Cr-1 Mo - 0.2 Si)
- 26Cr Ferritic (Fe-26Cr-1-Mo-2Mn-4.5Ni-1Si-1Al)
- AL 453 (Fe-22 Cr-0.6 Al-0.3 Mn + 0.1Ce/La)
- Crofer22 APU (Fe-22Cr-0.5Mn-0.08 Ti-0.016P-0.06 La)

The exposure conditions for the ferritic alloys included:
- T = 900°C and 700°C (Limited experiments were performed at 800˚C)
- One-Hour Cycles (45 min. hot, 15 min.cold)
- Atmospheres
-     Dry Air (Simulated Cathode Gas)
-     Air + 0.1 atm H_2O (Simulated Moist Cathode Gas)
-     Ar/H_2/H_2O (Simulated Anode Gas)
      (p_{O_2} = 10^{-17} atm at 900°C and 10^{-20} at 700°C)

The exposure apparatus used for these exposures is shown schematically in Figure 1.

     An additional group of model alloys was prepared in an attempt to grow a TiO_2 outer layer to suppress Cr volatility. Four heats of novel Fe-Cr-Ti alloys and one Ti-free control heat were produced in a vacuum induction melting furnace in the form of fifty-pound ingots at ATI Allegheny Ludlum. The chemical composition of each ingot was determined at ATI Allegheny Ludlum's Analytical Services laboratory (results reported in weight percent). Extensive manufacturing trials were carried out to evaluate the processing characteristics of the high-Ti stainless steels. The ingots were successfully hot-rolled to 10 mm, surface conditioned, and then cold rolled to 1 and 2 mm thickness for oxidation testing and mechanical/physical property determination.

Heat Identification Code

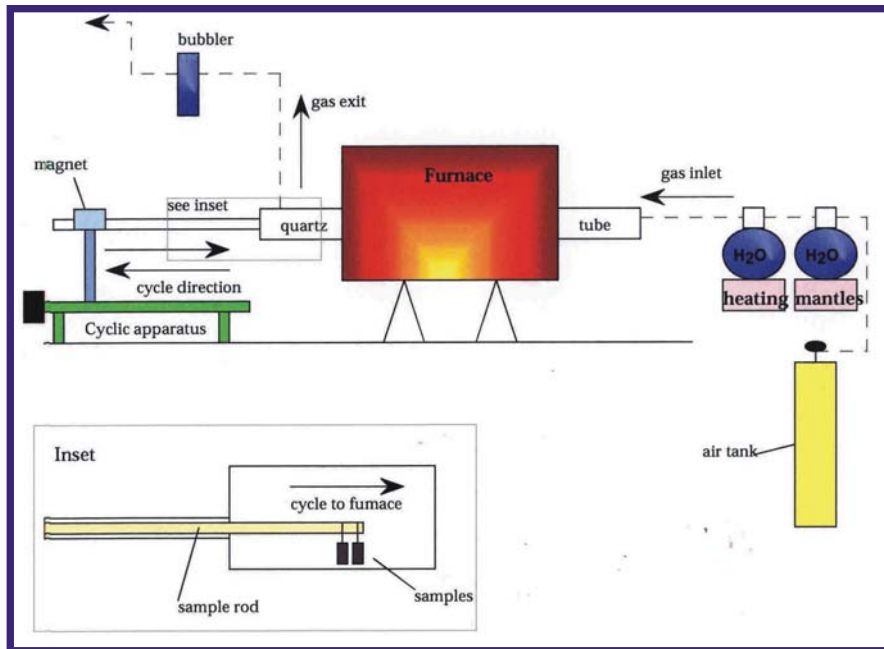| Element	RV 2103	RV 2104	RV 2095	RV 2096	RV 2097
Cr	21.8	21.8	22.1	22.2	22.2
Ti	0.004	0.84	1.65	2.72	3.98
Mn	0.033	0.030	0.031	0.024	0.023
C	0.010	0.013	0.010	0.016	0.017
N	0.018	0.018	0.011	0.008	0.008
Ce	0.004	0.027	0.031	0.027	0.027
La	0.001	0.009	0.012	0.012	0.010
Al	0.005	0.005	0.008	0.030	0.049
Si	0.043	0.042	0.036	0.020	0.020

Figure 1.   Schematic diagram showing the apparatus to cyclically oxidize coupon
              specimens in gases with defined and controlled amounts of water vapor in
              air at a total pressure of 1 atm.

The series of Fe-Cr-Ti alloys were subjected to cyclic tests as described above at $800^{o}C$
in the dry air and moist cathode gas environments. Long term exposures were also
performed in these atmospheres at $760^{\circ}C$. As these are new alloys, thermogravimetric
(TGA) measurements were also made. In this test, the sample is held at constant
temperature (no cycling) and the mass of the sample is continuously measured via a
microbalance (Figure 2). The results are used to determine the parabolic rate constant
which is related to the oxide thickness. The different atmospheres were used to exploit
the fact that vaporization occurs faster in moist environments. Comparing the results
from moist and dry tests will give an idea of the effectiveness of the oxide in preventing
vaporization. The test parameters are as follows:

- Alloys - Fe-22Cr-xTi (x=0-4), E-Brite, Crofer
- T= $800^{o}C$, $900^{o}C$
- Time = 1 week (168 hrs)
- Atmosphere
    - Dry Air
    - Air + 0.1 atm H_2O
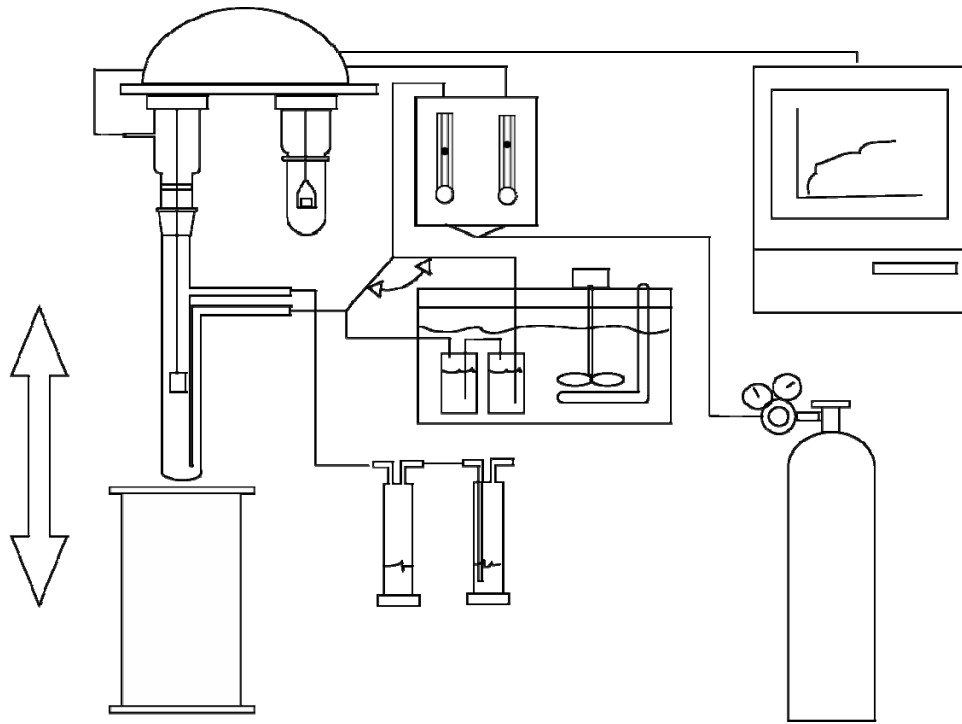
Figure 2.   Schematic diagram of the TGA apparatus for continuous measurement of
              mass during exposure.

Dual Atmosphere Exposures

A dual atmosphere testing apparatus was also constructed (Figure 3). The system consists of three parts. The first is the specimen holder, which is a superalloy cup with a hole in the bottom, through which the fuel gas is introduced. A mica washer (compressive seal) and the specimen are placed in the cup, covering the hole. The second piece is a stainless steel tube that fits into the top of the cup. It is used to introduce the oxidant gas to the system and is in contact with the specimen to supply further compression as necessary to seal the system. These two pieces are placed in a quartz tube sealed with silicone stoppers, which is in turn in a vertical furnace. Outside the system, opposing jacks at the ends of the cup and tube can be used to apply even further compression.

Specimen Characterization

Following exposure the oxidation products and alloy microstructure were characterized using x-ray diffraction (XRD), scanning electron microscopy (SEM) and energy dispersive x-ray analysis (EDS).
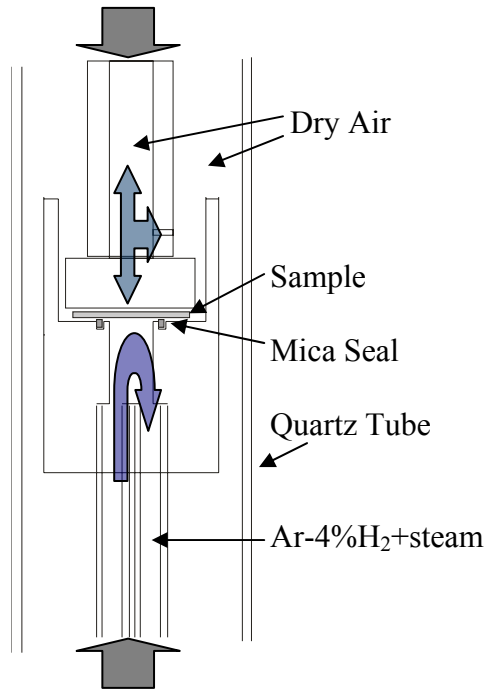
Figure 3.   Schematic diagram of the dual atmosphere apparatus.

Coated Specimens

    Specimens coated with a sputtered LaCrO$_3$ (some were also Sr doped) layer have been studied as these coatings may suppress oxide evaporation. The substrates are as follows:

- E-Brite (same as above)
- AL 453 (same as above)
- 29-4C (29Cr, 4 Mo, 0.5 Mn, 0.3 Ni, 0.35 Si)
- Type 446 stainless steel (similar to E-Brite)
- Inconel 600 (Ni based, 14-17 Cr, 6-1 Fe, max 1 Mn)

    X-ray diffraction showed that the coatings were amorphous in the as coated condition. E-Brite and T-446 specimens were exposed in a dry air (simulated cathode gas) atmosphere at 900°C for 100 hours to crystallize the coating and to form a chromia layer. It was observed during SEM analysis that the coatings had become porous during the exposure. The porosity was considered to be detrimental to the effectiveness of the coating to prevent vaporization. As a result, the subsequent experiments on the coated specimens involve annealing to crystallize the coatings. However, the volume change during crystallization resulted in cracking of the coatings. A limited number of experiments were performed to attempt to seal the cracks. The techniques used were:
- Aluminizing in a commercial CVD reactor.
- Application of a liquid precursor to form La-oxides.

Area Specific Resistance Measurements

       The electrical conductivity of the oxidized specimens was measured using a 4 point probe technique. Figure 4 is a schematic diagram of the apparatus that was constructed. Electrical contact was made with the coupons, following oxidation using platinum paste (SPI Lot No.1090120). The paste was painted in 6x6 mm squares on both sides of the specimen. Following application of the platinum paste, the specimens were exposed at 600°C for one hour in dry air to drive off the binder in the paste, and to sinter the platinum particles. Platinum paste was then reapplied to the specimen, which was followed by another annealing step at 600°C for one hour. The surfaces of the specimens were then examined using an optical microscope or a scanning electron microscope to insure that the paste covered the desired area. The specimen is then placed between two Pt foils that previously had lead wires spot welded in place. This sandwich is placed in the slot in the specimen holder and the screws are tightened to ensure physical contact is maintained throughout the test. The specimen holder is placed on another holder that is attached to the reaction tube end cap. This entire set up is then put into the furnace and heated. The lead wires are attached to the current source/voltmeter. Current was applied using a Jandel Model RM2 current source, at a fixed amperage between 1000-10,000μA. The voltage drop across the specimen was also measured by the Keithley 2001 multimeter. A resistance is calculated via Ohm's law, $V=I*R$. The ASR is then calculated by multiplying the resistance by the known area of the Pt paint.

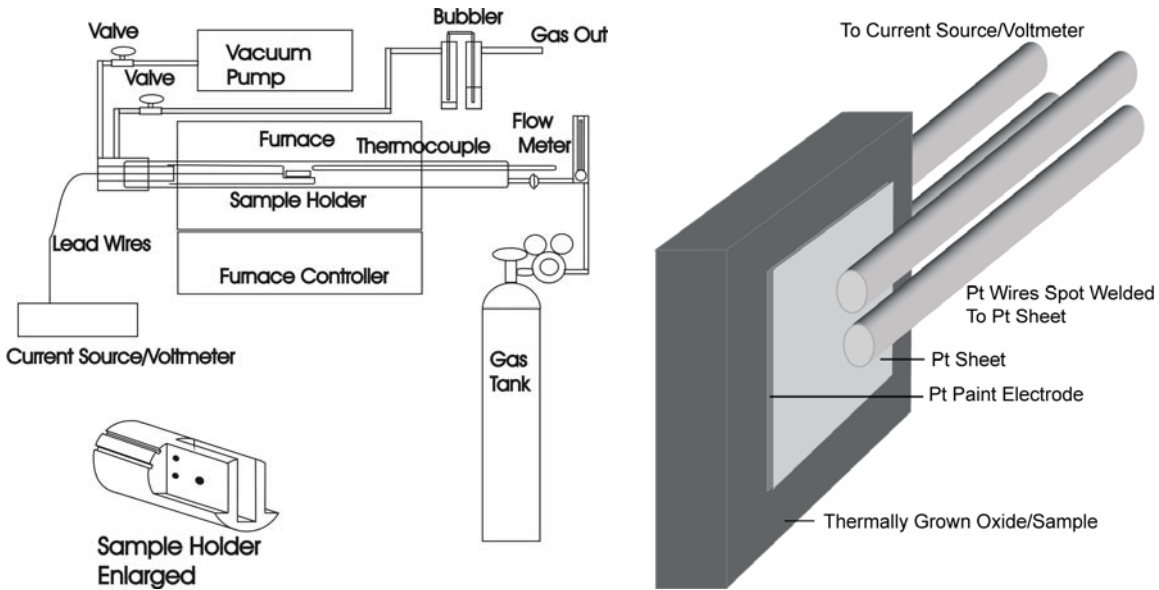Figure 4.   Schematic diagram of the ASR apparatus and cartoon showing a close up of the specimen and electrode/lead attachments.

Task 2

Indentation Testing

The use of indentation as a means for inducing chromia scale spallation from interconnect alloys builds upon previous research by the PIs involving indentation of thermal barrier coating (TBC) systems [1, 2]. Testing goals in TBC and interconnect alloy systems are similar, where an understanding of mechanisms leading to coating spallation is needed, as are methods for accelerating cyclic thermal testing to evaluate new coating/substrate systems.

The test for SOFC interconnects currently involves indenting the specimen using a Rockwell hardness tester and a conically-shaped brale indenter. The chromia scale is penetrated by the indenter and the interconnect alloy substrate is plastically deformed. This plastic deformation induces compressive radial strains in the substrate, which are transferred to the chromia scale (there is a match of in-plane strains across the interface). This causes an axisymmetric region of spallation, either in the form of intermittent flaking of the scale or as an intact peeling of the scale from the substrate. The radial extent of the debonding or its density as a function of radial distance can be related (through fracture modeling) to the fracture toughness or distribution of fracture toughness of the chromia/alloy interface. Micrographs of debonds resulting from indentation are given in the section on Indentation Testing of Interface Adhesion.

This type of test can be applied to other brittle coating systems deposited or grown on comparatively ductile substrates. As part of this program, chromite-coated interconnect alloys are being tested, where indentation can induce spallation of the chromite coating and a chromia layer growing beneath it. Similarly, this type of test may be applicable to the testing of other SOFC interfaces, such as those between sealant glasses and interconnect materials and those between electrolyte and anode layers in anode-supported cell structures.

Indentation testing has been performed for the following alloy systems and exposure conditions, which parallel cyclic oxidation experiments described above:

- E-BRITE in Air + 0.1 atm H_2O: 100 Hrs. and 200 Hrs. @ 900°C
- E-BRITE in $Ar/H_2/H_2O$ (SAG): 264 Hrs, 364 Hrs. and 464 Hrs. @ 900°C
- $La_{0.8}Sr_{0.2}CrO_3$ on E-BRITE, AL 453 and AL 29-4C (from PNNL): As Processed
- $LaCrO_3$ on Inconel and SS 446 (from Drexel/NETL): As Processed
- $La_{0.8}Sr_{0.2}CrO_3$ on E-BRITE and $LaCrO_3$ on SS 446: 100 Hrs. @ 900°C
- Indentation tests on interconnect specimens exposed at 700°C is currently underway.

A full description of these tests and their relation to cyclic oxidation testing is provided in the sections on Indentation Testing of Interface Adhesion and Accelerated Testing

Task 3

Experiments are being carried out on pure Ni as a possible alternative interconnect material since the oxygen partial pressure in the anode gas is too low to

oxidize Ni. Efforts to decrease the electrical resistance of the interconnect oxide are twofold. First, surface dopants are being used to reduce the scale thickness. Pulsed laser deposition (PLD) is used to deposit thin films of SrO and CeO_2 onto the surface of nickel. Second, the resistance introduced by the thermally grown oxide is being by-passed by the use of high conductivity pathways. Silver is not considered as a possible interconnect material due to the high permeability of hydrogen and oxygen in silver, which causes water nucleation and mechanical instability. However, silver may be able to provide a high conductivity pathway through another material. Systems in which silver wires are passed through nickel and silver powder is melted into holes drilled in nickel have been examined. Figure 5 presents a schematic diagram of these composite specimens.

Exposure Conditions
        The exposure conditions for the Ni-base materials are the same as those described for Task 1. In addition, since some Ni alloys are available as tubes, a second dual atmosphere apparatus has been constructed, Figure 6.

Specimen Characterization
The specimen characterization techniques are the same as those described for Task 1.
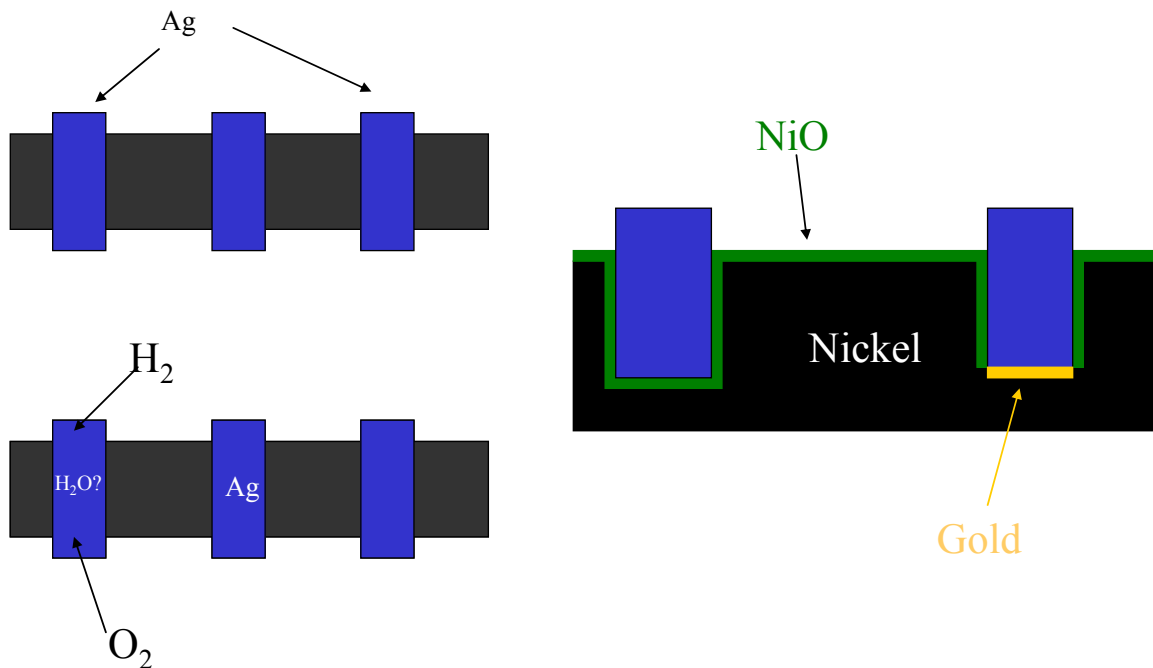
Figure 5.   Schematic diagram showing possible ways of using silver as a conducting path through nickel interconnects.

Figure 6.   Schematic diagram of dual atmosphere apparatus for exposing tubular specimens.

Task 4: Development of Durable Contacting Material (WVU)

Samples have been fabricated using various compositions of silver and differing oxides such as LSM and copper-oxide. The samples were fabricated by dry pressing followed by sintering at high-temperature for various periods of time. It was determined that this method did not result in samples that were robust enough for use in the high-temperature evaporation experiments. In order to fabricate samples that were durable enough for testing, it was decided that the method of fabrication be modified. Instead of the ball-milling/pressing/sintering method previously used, it was decided that the oxidation of specific alloys would be a simpler method to produce reliable samples. Sterling silver has been identified as a candidate for use as a contacting material due to its favorable composition and low-cost. Upon oxidation, the copper in the sample becomes copper-oxide which is meant to act as a barrier against evaporation of the silver in the sample, extending the usable life of the cermet. Sterling silver has been tested in high-temperature exposure alongside pure silver for a period of 27 weeks to gain an understanding of the performance of copper-oxide in protecting against silver evaporation.

RESULTS AND DISCUSSION

Task 1: Mechanism-based Evaluation Procedures

The oxidation results for the ferritic stainless steels under fuel cell conditions have been reported previously [3]. These results have also been described in a manuscript accepted for publication in Oxidation of Metals. This manuscript is attached as Appendix A.

In attempts to reduce the growth rate of chromia, and, therefore, the electrical resistance, E-Brite samples have been doped with CeO_2 using pulsed laser deposition (PLD). Oxidation experiments for 100 hours at 800°C in air show that the doping drastically reduced the thickness of the chromia scale.

Sigma phase was observed to form at 700°C in the alloys with higher chromium concentrations, e.g. 26 Cr Ferritic and E-BRITE. Sigma phase is promoted in these alloys by the presence of Mo. (additions of W would have a similar effect.) It was also found

that impurity elements, such as Si, accelerated the formation of the sigma phase, e.g. 26 Cr Ferritic developed this phase more rapidly than did E-BRITE. A previously unknown result was that sigma phase formation was dramatically accelerated in atmospheres containing water vapor. Sigma- phase must be avoided since it is very brittle and tends to crack.

It was found that even small amounts of Al or Si (less than 0.5 wt %) in ferritic steels result in the formation of continuous alumina or silica films which greatly increases the ASR. Therefore, future alloy development should hold these elements to the minimum values possible.

A major problem with chromia-forming alloys is oxide volatility as CrO_3, particularly in the cathode gas, since the CrO_3 partial pressure increases with oxygen partial pressure. The volatile species are reduced at electrochemically active sites on the cathode during SOFC operation, which inhibits the required oxygen reduction. Analysis of the Cr vapor species indicates water contents above about 0.1% in air result in partial pressures of $CrO_2(OH)_2$ which exceed the partial pressure of CrO_3 and result in cathode poisoning. There are three potential solutions to this problem:

1. Develop cathode materials that are not affected by Cr contamination.
2. Suppress the evaporation of Cr-species from ferritic alloys.
3. Develop Cr-free materials with suitable interconnect properties.

The latter two approaches have been pursued in this research. Approach 3 is described in Task 3 below.

An ideal approach to suppressing Cr volatility would be to develop an alloy which forms a Cr-free oxide overlayer. Experiments on Ni-base superalloys indicated that Ti additions might provide such a layer. Four heats of novel Fe-Cr-Ti alloys with Ti contents varying between 1 and 4 wt% and one Ti-free control heat were produced by ATI Allegheny Ludlum. Ingots were melted in a vacuum induction furnace with a fifty pound crucible. These were hot and cold-worked to flat sheets approximately 0.5 mm thick by 150 mm wide without incident.

Initial characterization of these Fe-Cr-Ti alloys was carried out to determine the effect of titanium on mechanical properties and on coefficient of thermal expansion. Figure 7 presents the results of duplicate tensile tests. Titanium was found to increase both yield and ultimate tensile strength and to decrease plastic elongation compared to the base Fe-22Cr alloy. The changes were significant for the two highest titanium alloys, where the ductility was particularly low and may be unacceptable for forming applications.

Adding titanium was found to have a negligible effect on the linear coefficient of thermal expansion (CTE) compared to the base Fe-22Cr alloy at the lowest level of addition (0.84 wt.%). For the higher levels, titanium was observed to systematically increase the CTE (Figure 8). For additions ranging from 1.7 to 4.0 wt.%, the percentage change in CTE relative to the base Fe-22Cr alloy was found to obey the following relationship over the temperature range 600-900°C.

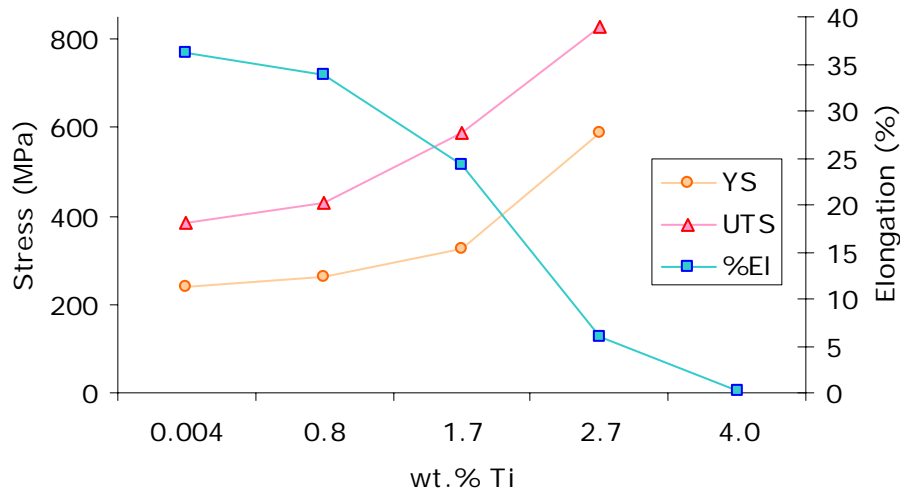$$\Delta\alpha(\%) = 4.8 \times (wt.\%Ti) - 3.5$$

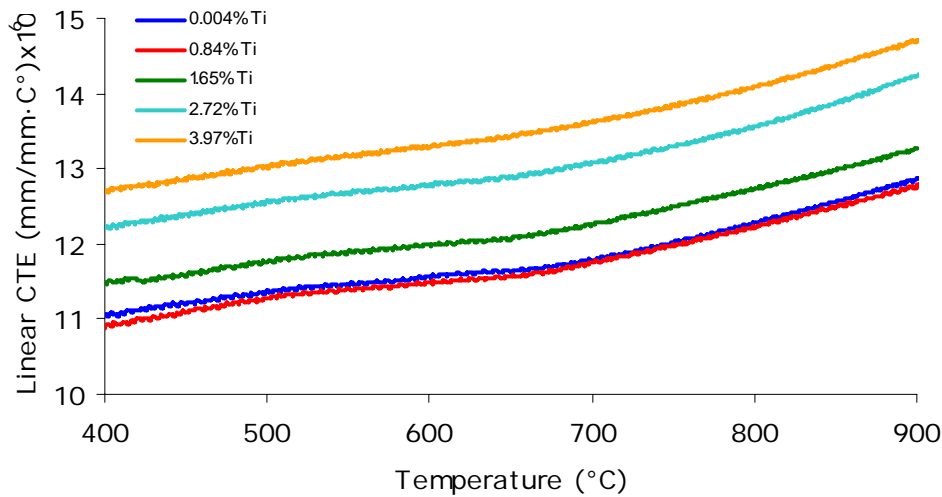Figure 7.   Effect of titanium on the mechanical properties of a model Fe-22Cr alloy.

Figure 8.   Effect of titanium on the linear coefficient of thermal expansion of a model Fe-22Cr alloy.

Isothermal oxidation (Figures 9) experiments indicate that the Ti additions, at least to 3 wt%, accelerate the oxide growth rate at 900˚C relative to the Fe-Cr baseline alloy and CroFer. The same trend is evident in the cyclic oxidation kinetics at 800˚C (Figure 10). Figure 11 indicates that indeed these alloys can form a continuous TiO_2 overlayer, particularly for the higher Ti concentrations. The cross-sections also indicate that there is significant internal oxidation of the Ti below the chromia scale.
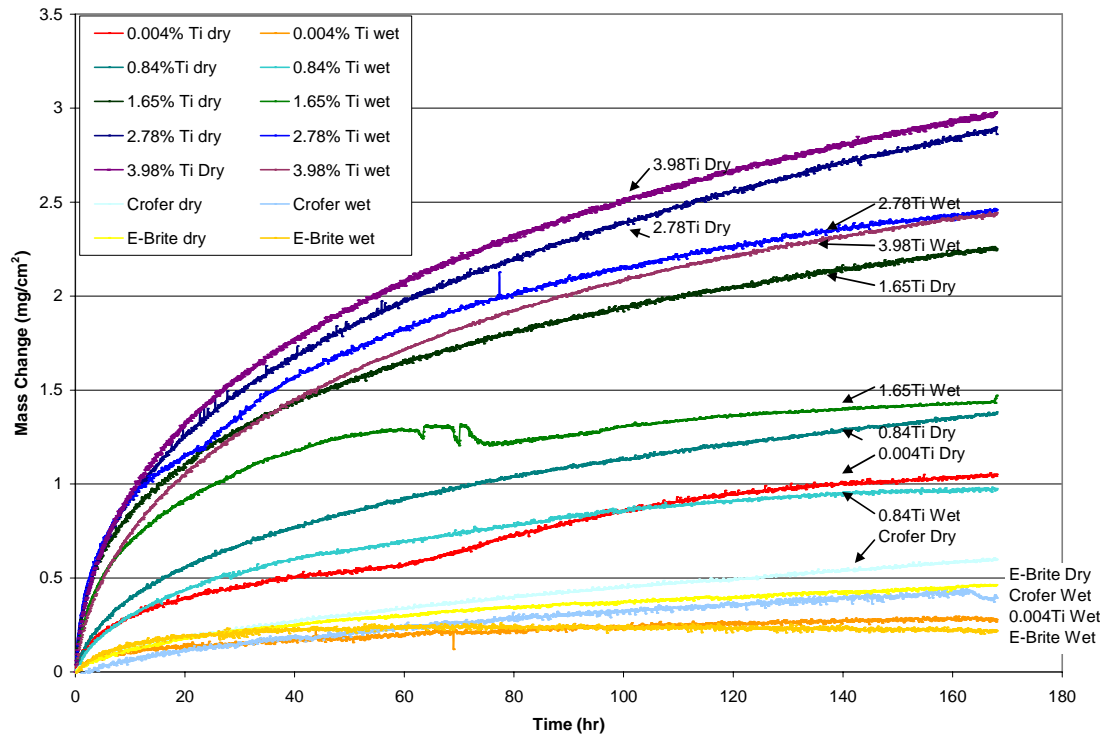
Figure 9. TGA data for Fe-Cr-Ti alloys, Crofer, and E-Brite at 900˚C in dry and moist atmospheres.
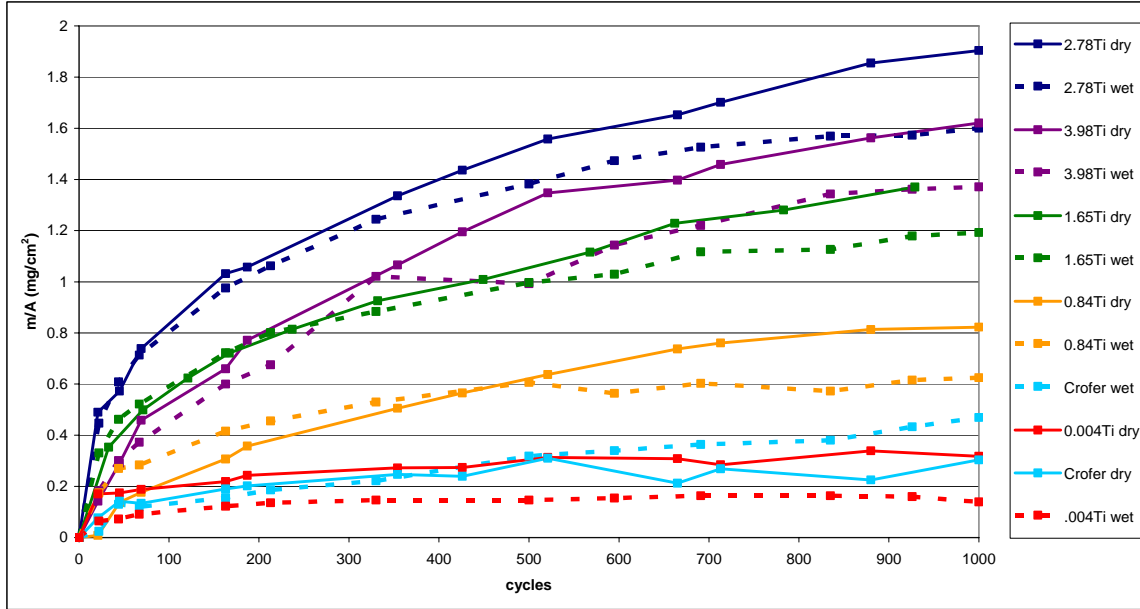
Figure 10.   Cyclic oxidation data for Fe-Cr-Ti alloys and Crofer, at 800°C in dry and moist atmospheres.

Long-term exposures of the Fe-Cr-Ti alloys were carried out in both ambient and humidified air at 760°C. Samples of E-BRITE alloy, which has been well-characterized in such tests, was included for comparison purposes. All of the samples were tested simultaneously. The humidified air environment was maintained by using a tube furnace of similar construction to Figure 1. Samples were cycled to room temperature once per week for weighing and inspection throughout the nominal 3,000 hour exposure period.

In ambient air, the addition of titanium resulted in a consistent increase in weight gain up to a level of 2.7 wt.%, at which point the incremental weight gain appears to have reached a plateau (Figure 12). In air containing added water vapor, adding titanium has a notable effect on the rate of chromium oxide evaporation (Figure 13). The E-BRITE and Fe-22Cr model alloy samples both exhibit a tendency towards weight loss, with the cumulative weight gain after 3,000 hours approaching zero. Adding titanium to the base Fe-22Cr appears to reduce the rate of evaporation, with the effect proportional to the amount of added titanium. Figure 14 compares the two data sets by taking the ratio of weight gain after 3,000 hours in humidified air to that in ambient air. If evaporation is completely suppressed, this ratio should equal one. The nominal reduction in the effect of evaporation increases the ratio from about 0.3 for the base Fe-22Cr alloy to approximately 0.8 for the Fe-22Cr-2.7Ti alloy. There is no apparent effect caused by further increasing the titanium content to 4.0 wt. %.
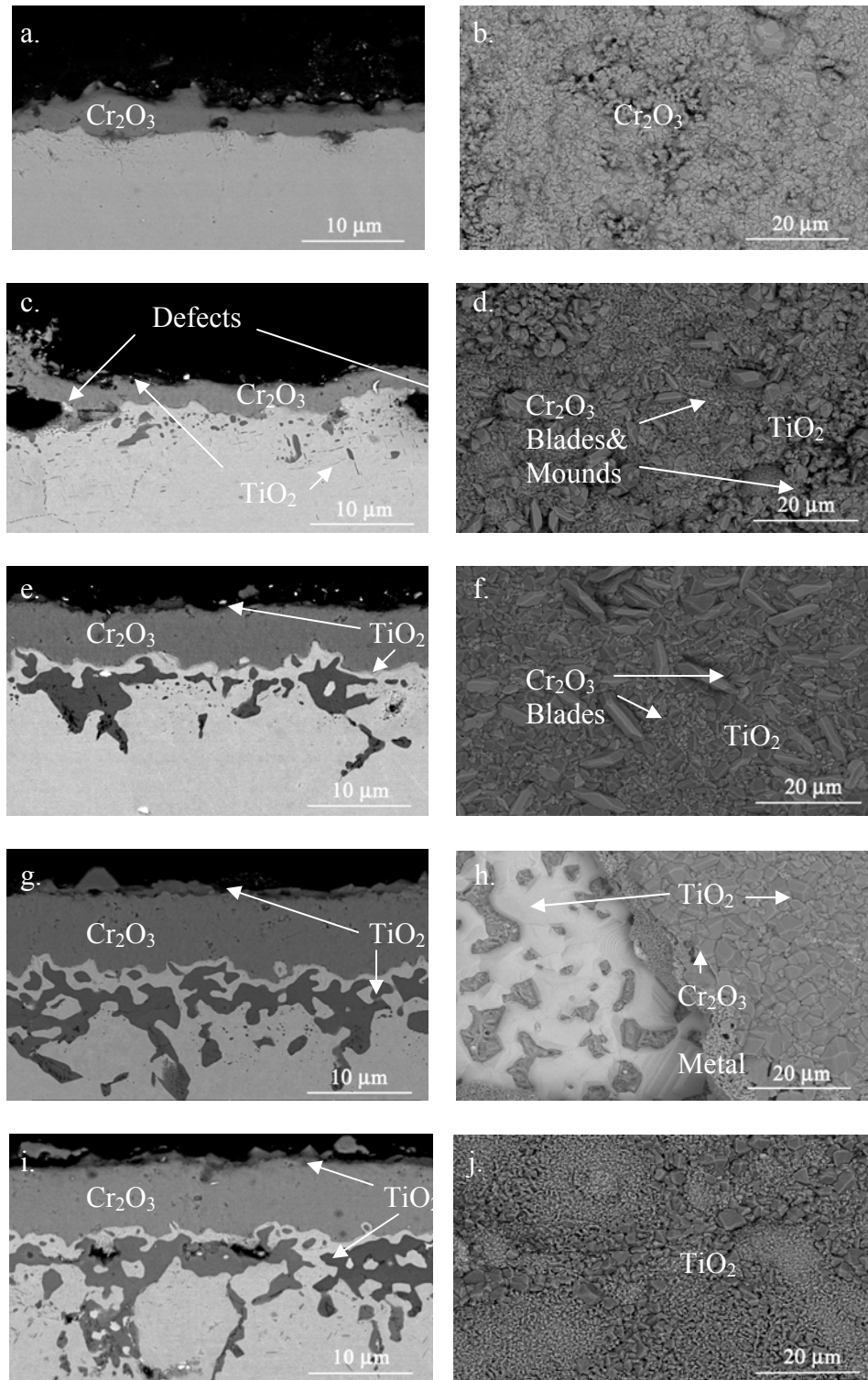
Figure 11.   Cross – sectional and surface SEM micrographs of alloys exposed for 96 hrs at 900°C in dry air containing 0.004% (a&b), 0.84% (c&d), 1.65% (e&f), 2.78% (g&h), and 3.98% (i&j) titanium.
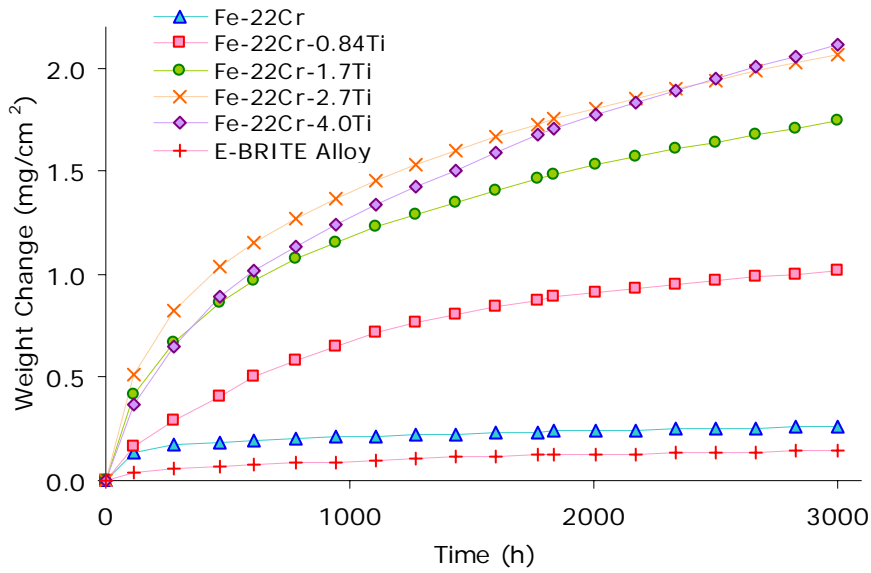
Figure 12.   Long-term oxidation test results at 760°C in ambient air for Fe-22Cr alloys with added titanium (E-BRITE sample included for a reference).
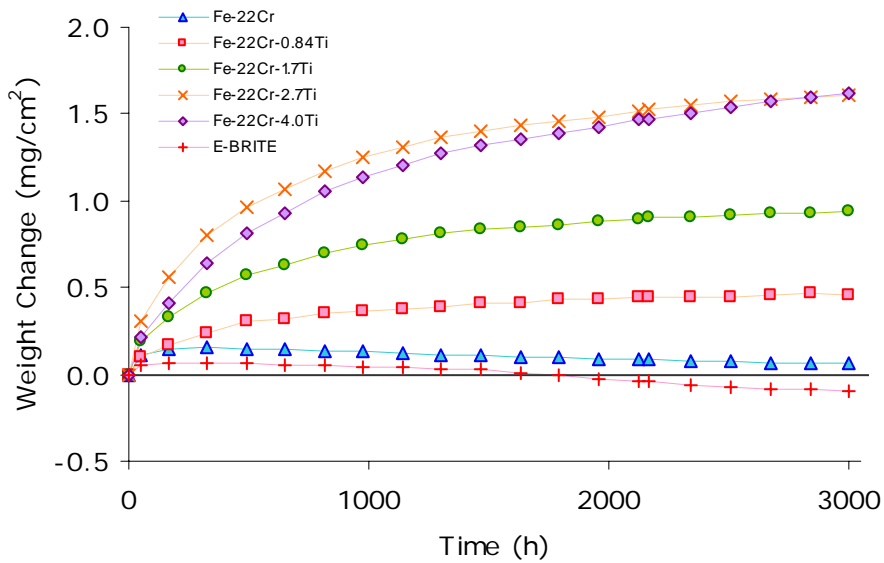
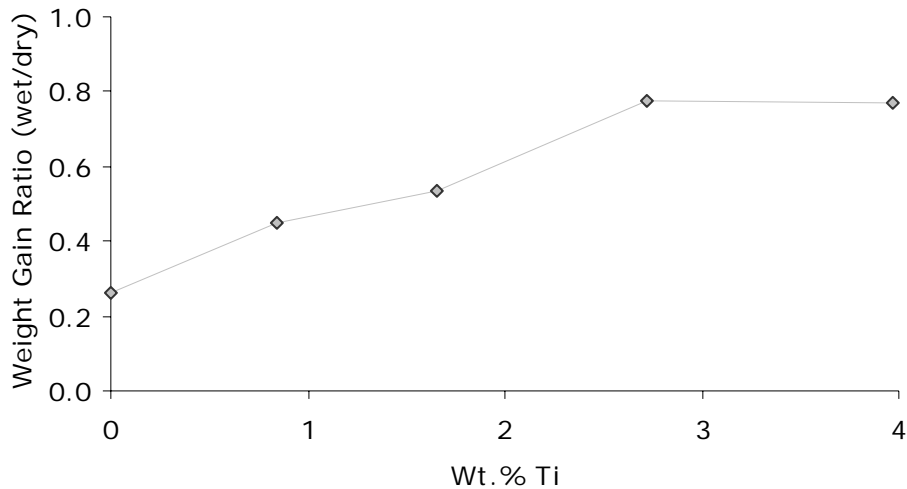Figure 13.   Long-term oxidation test results at 760°C in air containing 7% water vapor for Fe-22Cr alloys with added titanium (E-BRITE sample included for a reference).

Figure 14.   Comparison of weight gains after 3,000 hours at 760°C for Fe-22Cr alloys with added titanium – ratio of terminal weight gain in air containing 7% added water vapor to terminal weight gain in ambient air.

The effect is shown in direct comparisons in Figures 15-17 for the Fe-22Cr base alloy, Fe-22Cr-1.7Ti, and Fe-22Cr-4.0Ti. It is apparent that increasing the titanium content reduces or eliminates the tendency for the overall weight gain curve to transition from net positive to negative, as observed for Fe-22Cr. There remains, however, a significant difference between the terminal weight gain results between the samples exposed in ambient and humidified air, with the humidified air testing always resulting in lower weight gains. It is difficult to deconvolute the observed oxidation kinetics for the Fe-Cr-Ti alloys, as the weight gain is made up of three factors – weight gain due to internal oxidation of titanium, weight gain due to external oxide formation (split between titanium oxide and chromium oxide layers), and weight loss due to oxide scale evaporation. There is uncertainty regarding the rates of these processes and there may be complex interactions between them. Therefore, it is difficult to absolutely quantify the efficacy of adding titanium to Fe-Cr alloys for reducing the tendency for chromium oxide evaporation in humidified air.

Post-exposure structures similar to those presented for the short-term samples were noted in the long-term oxidation samples. Figure18 is a collection of micrographs taken after a 500 hour exposure at 816°C in ambient air, which resulted in well-developed oxide scale microstructures. The titanium-free samples exhibited chromium oxide scales, with the oxide on the E-BRITE alloy being very thin and smooth, while the oxide scale on the Fe-22Cr alloy was thicker and more convoluted. The alloys containing titanium formed thick oxides which were rich in titanium on the surface. The oxides were highly variable in thickness from location to location, with maximum thickness increasing steadily with titanium content. All of the alloys had similar minimum thickness values, which may explain continued volatility at higher titanium levels due to potential thin spots in the titanium oxide outer layer. Beneath the oxide were zones of internal oxidation and internal nitridation. The depth and severity of the internal oxidation increased with titanium content. The number and size of the internal titanium

27

nitrides increased with titanium content, but the depth of the internally nitrided zone appeared to be fairly consistent for the titanium-bearing alloys. The presence of the internal nitridation layer is not typical for chromia-forming stainless steels in oxidizing environments and suggests that the titanium addition is permitting nitrogen transport through the oxide scale, either by physical access to the metal through cracks/voids, or by increased permeability through the condensed oxide.

	E-BRITE alloy	Fe-22Cr alloys				
		0.004% Ti	0.84% Ti	1.7% Ti	2.7%Ti	4.0%Ti
oxide thickness (microns)	1.1	1.7-2.6	2.1-4.0	2.6-6.7	2.9-8.7	1.9-10.7
internal oxide depth (microns)	-	-	5	9	21	23
internal nitridation depth (microns)	-	-	23	21	21	23
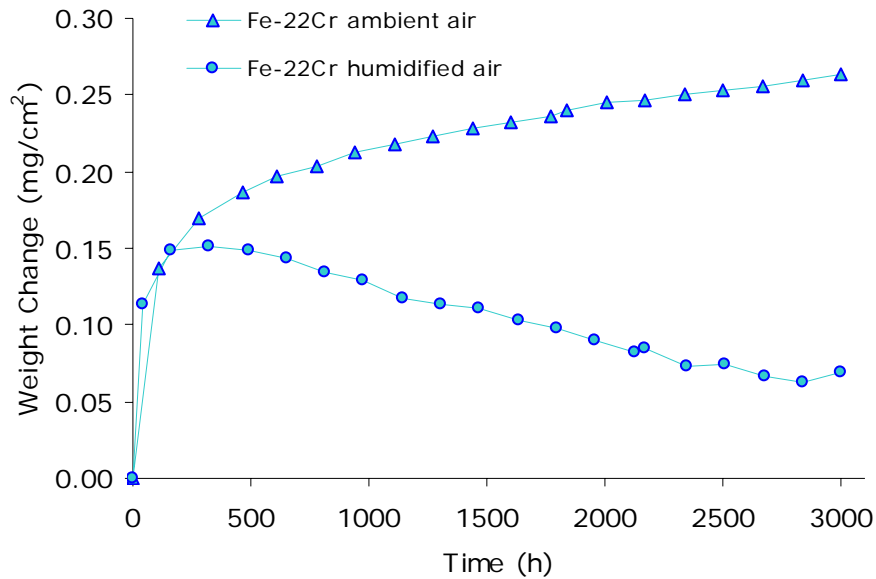
Figure 15.   Long-term oxidation test results for base Fe-22Cr alloy at 760°C in air with and without added water vapor.

28
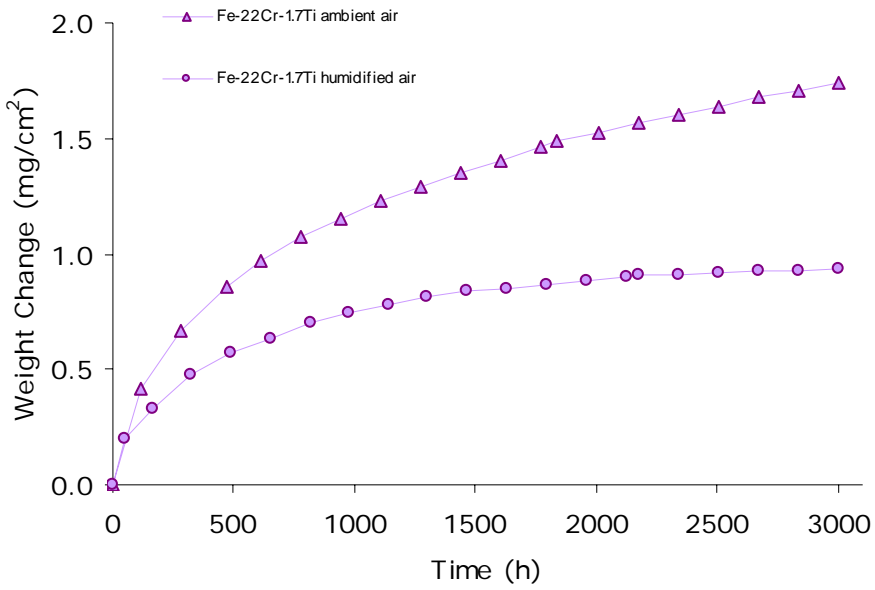
Figure 16.   Long-term oxidation test results for base Fe-22Cr-1.65Ti alloy at 760°C in air with and without added water vapor.
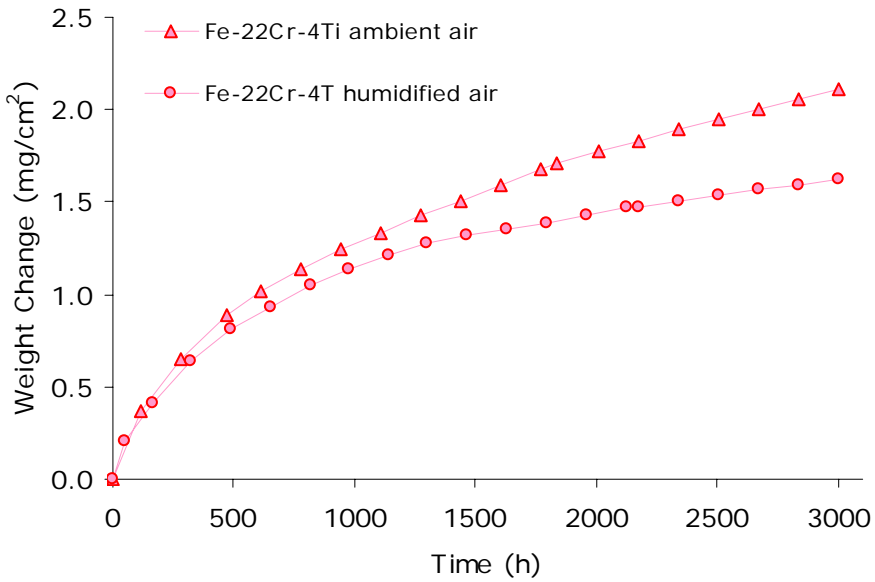
Figure 17.   Long-term oxidation test results for base Fe-22Cr-4.0Ti alloy at 760°C in air with and without added water vapor.
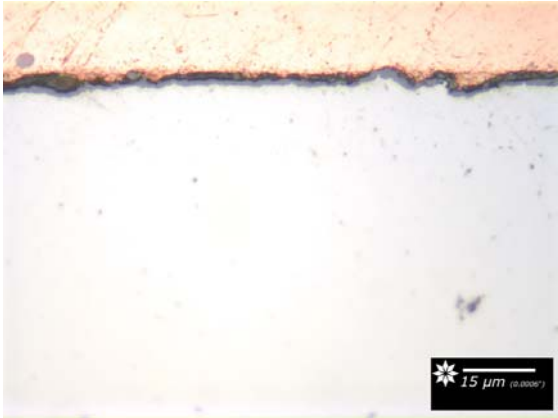
E-BRITE alloy
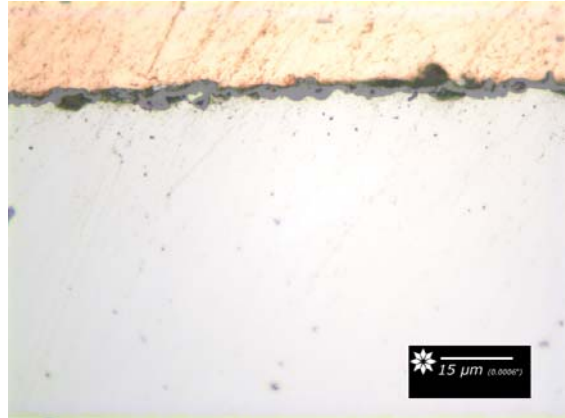
Fe-22Cr
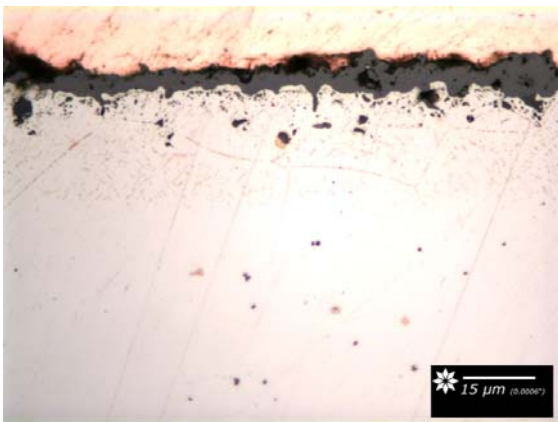
Fe-22Cr-0.8Ti
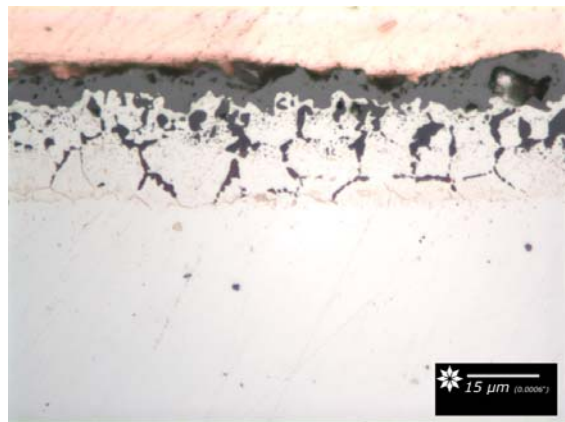
Fe-22Cr-1.7Ti

Fe-22Cr-2.7Ti
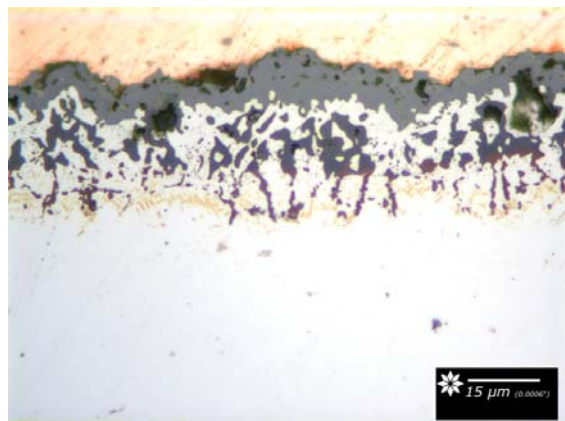
Fe-22Cr-4.0Ti

Figure18.   Metallographic cross-sections of different alloys exposed for 500 hours at 816°C in ambient air (light optical micrographs).

A limited number of experiments were conducted in an attempt to seal cracks in $La_{0.8}Sr_{0.2}FeO_3$ coatings on a ferritic steel substrate. Two sputter coated E-Brite specimens were annealed at 800˚C in argon to create cracks as the coatings crystallized. One specimen was then vapor-phase aluminized at Howmet Corporation using a standard procedure used for coating superalloys. It was hoped that the aluminum would only deposit in the cracks so that subsequent heating in air would result in alumina in the cracks to suppress Cr evaporation. The surface of this specimen after aluminizing is presented in Figure 19. Examination of this surface using EDS indicated the aluminum had deposited on the $La_{0.8}Sr_{0.2}FeO_3$ coating as well as in the cracks. Therefore, subsequent oxidation would produce a continuous alumina layer, which would make an unacceptably large contribution to the ASR of the specimen. Figure 20 shows the opposite side of the same specimen where the aluminum was deposited directly on to the E-Brite. The aluminide coating cracked on cooling from the coating temperature presumably because the low CTE of E-Brite resulted in tensile stresses in the brittle coating.

The second specimen was coated with La_2O_3 from a liquid precursor. The surface of the coating is presented in Figure 21. There has been some deposition in the cracks. The La_2O_3 would tend to react with any volatile Cr-oxides to form the stable compound $LaCrO_3$ which has been used as an interconnect coating. Therefore, there may be value in attempting to optimize the technique for crack sealing using liquid precursors.
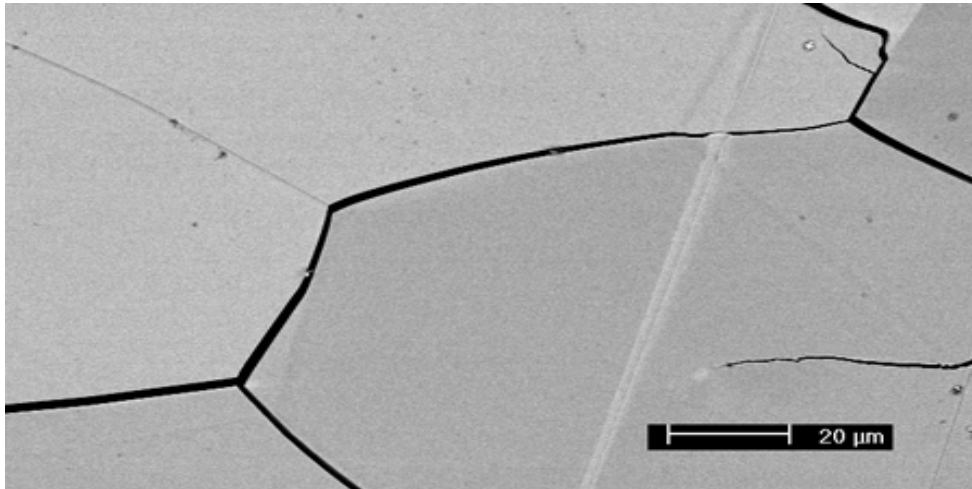

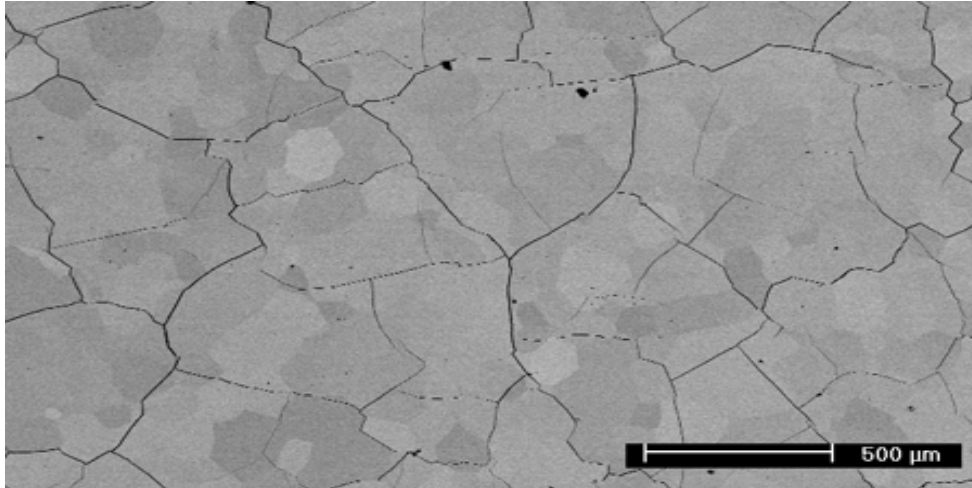Figure 19.   Surface of La-Sr-ferrite coating after aluminizing.

31

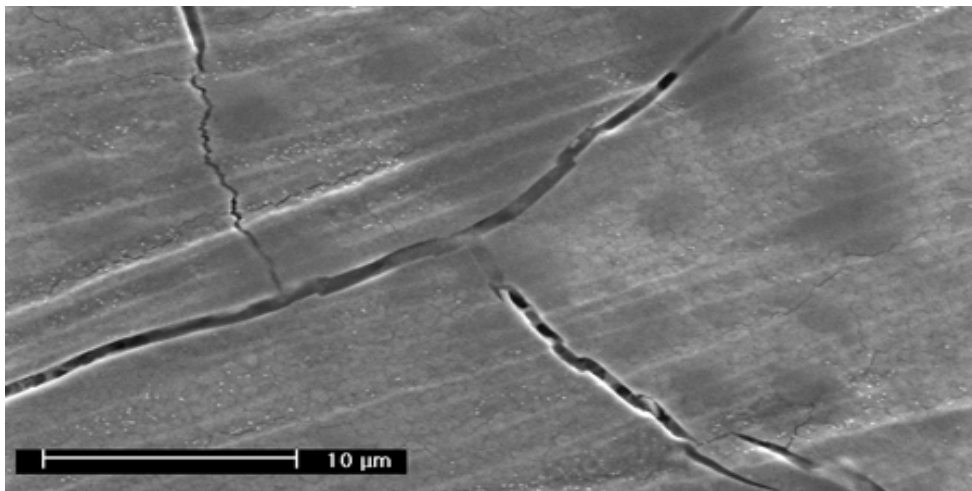Figure 20.   Surface of ferritic steel substrate after aluminizing.

Figure 21.   Surface of La-Sr-ferrite coating after deposition of La_2O_3 from a liquid
                precursor.

Task 2: Fundamental Aspects of Thermomechanical Behavior (CMU)
        Previous reports have described the indentation fracture testing of ferritic stainless
steel alloys exposed to simulated anode gas (SAG) $Ar/H_2/H_2O$ environments. Indented
chromia scales formed in SAG debond as an intact coating, and the radial extent of the
debonding observed in short-term exposures has been used to estimte the long-term
exposure time when spallation can occur. Previous reports also presented indentation
results for ferritic stainless steels exposed in air with 0.1 atm H_2O, representing a moist
simulated cathode gas (SCG) environment. When indented, those specimens exhibited a

flaking type of debonding with a decreasing density of flaking with radial distance from the indent. Results for both types of tests are summarized in the paper by Dhanaraj et al. [4] which is attached as Appendix B.

In this past year, an image analysis technique has been developed to analyze the failures seen in SCG-exposed interconnects. In these specimens, bonded areas are black or dark grey, which is the shade of the chromia scale. Areas of spallation appear white or very light grey due to the exposed metal substrate. The imaging technique involves quantifying the distribution of white/grey/black pixels in a single image in regions far from the indentation. The distributions of greys in 5-7 rings around the indentation are also determined. The percentage of debonding in a ring is determined by subtracting the distributions of grey from that ring from the far-field image distribution. The result from the analysis of multiple rings is a plot of the percentage of debonding scale vs. radial distance from the debond. Results from images taken after different exposures allow the tracking of debonding vs. radius as a function of exposure.

Figure 22 gives an example of results from this type of analysis. In the figure, images from indentation of a 26 Cr ferritic alloy exposed in SCG from 10 to 200 hours have been analyzed. Images at 10 and 200 hours are included in the figure, as is a plot of the percentage of debonding vs. R/a for different exposures. R is the radial distance from the indentation and a is the radius of the indentation. The images taken in these tests show a fairly consistent decrease in debonding density with radius and an increase in debonding density with exposure. Plots of debond percentage vs. R/a from the image analyses are consistent with these qualitative observations. As exposures are increased, the curves of percentage debonding rise, but the increases in debonding stop at 100-200 hours of exposure. At this point, some amount of debonding is observed even at radial distances where the strains due to indentation are almost zero.

The conclusion from these results is that after 100-200 hours of exposure in SCG at 900°C, spontaneous spallation (spallation that can occur without the use of indentation) has begun to occur. At this point, spontaneous spalls (and perhaps some scale evaporation) act to keep the average thickness of the chromia scale more or less constant, so that plots of debond percentage vs. R/a reach a steady-state. This is consistent with weight gain measurements performed as part of Task 1 of this project. Weight gains in these specimens stop after 100 hrs of exposure and specimen weight remains constant from that point on.
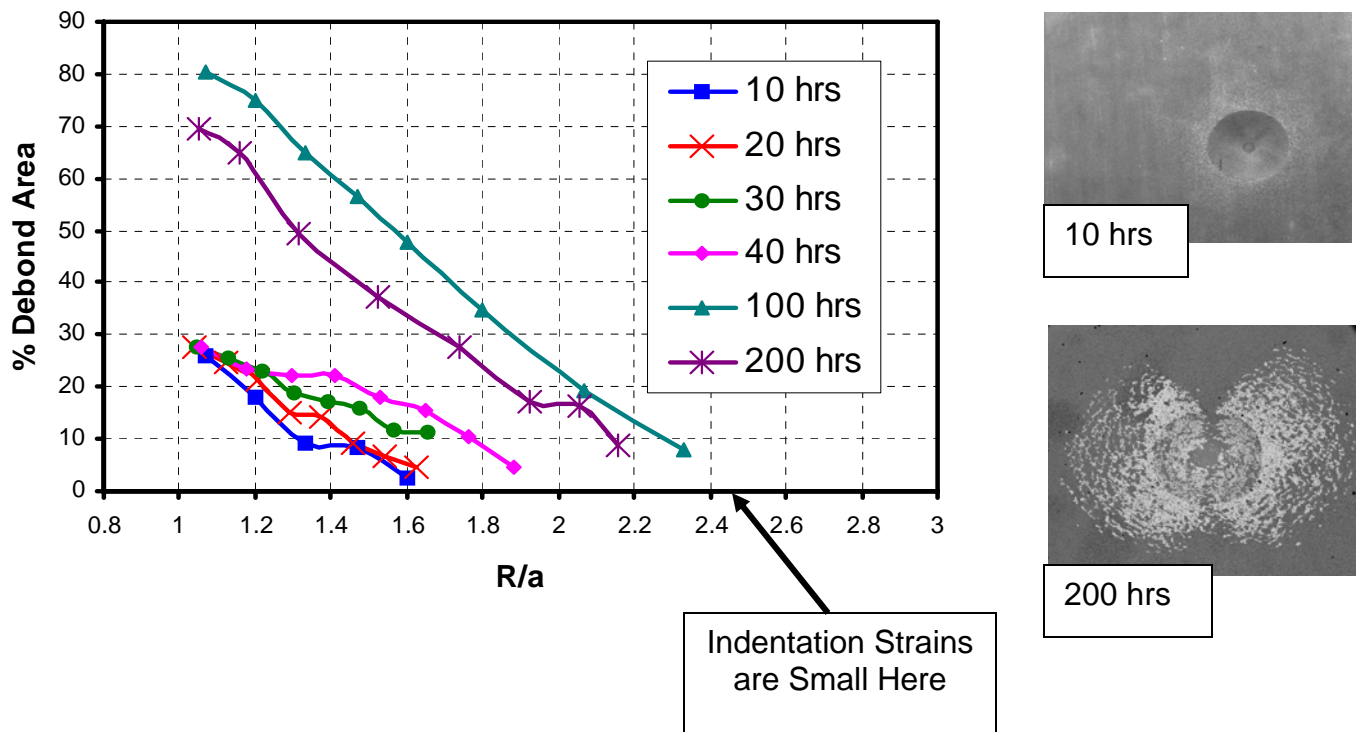
Figure 22. Percentage of Debonding vs. Radial Distance for a 26 Cr Ferritic Alloy Exposed in Wet Air (Simulated Cathode Gas) at 900°C for 10 – 200 hrs

Task 3 Alternative Materials

Experiments are being carried out on pure Ni as a possible alternative interconnect material since the oxygen partial pressure in the anode gas is too low to oxidize Ni. The primary challenge in making Ni perform satisfactorily as an interconnect, is to reduce the electrical resistance of the thermally grown oxide, that forms on the cathode side during fuel cell operation.

Efforts to decrease the electrical resistance of the interconnect oxide are twofold. First, we have tried to reduce the scale thickness by the use of surface dopants. Pulsed laser deposition (PLD) is used to deposit thin films of SrO and CeO_2 onto the surface of nickel. These experiments have shown that CeO_2 decreases the thickness of NiO by a factor of 4 (Figure 23) and SrO doping decreases it by a factor of 2. ASR is proportional to scale thickness and the resistance decreases accordingly (Figure 24). These dopants can be deposited by inexpensive techniques once the optimum dopants are identified.

Tubes of Ni 200 have been exposed under dual atmosphere conditions in the apparatus presented in Figure 6. Cross-sections of tubes for air-air and air-SAG exposures are presented in Figure 25 and indicate no effect of the dual-atmosphere.
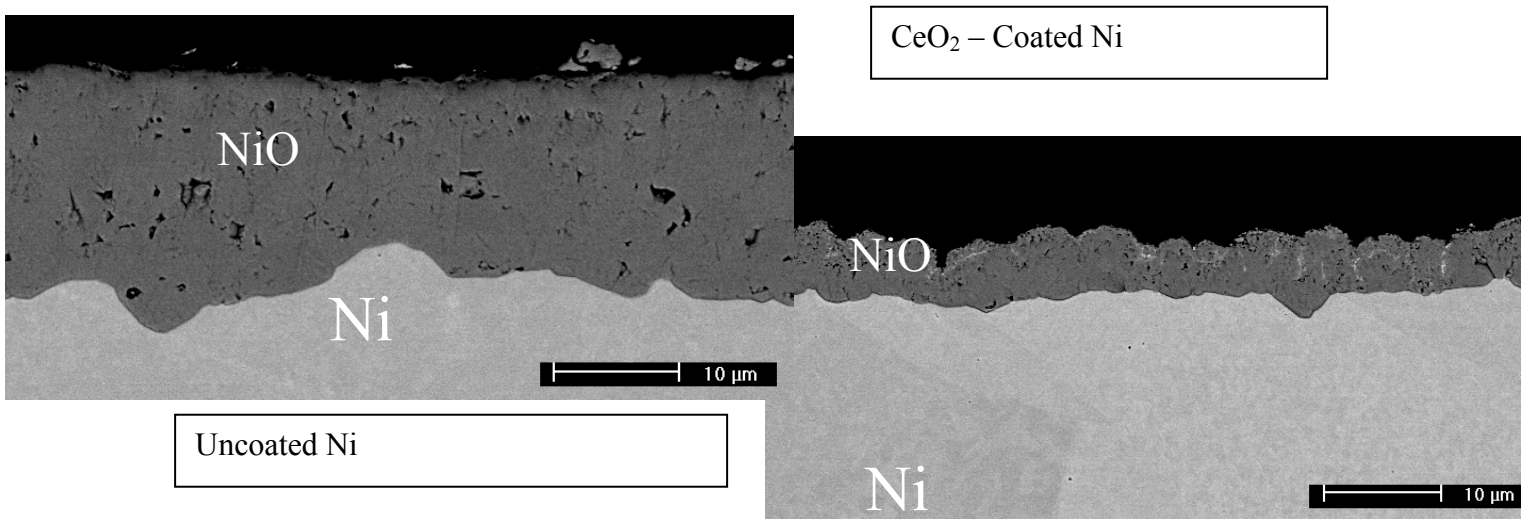
Figure 23.   Effect of CeO2 deposited by pulsed laser deposition on the growth rate of NiO for 100 hours at 800°C in dry air.

Finally, the resistance introduced by the thermally grown oxide has been by-passed by the use of high conductivity pathways. Silver is not considered as a possible interconnect material due to the high permeability of hydrogen and oxygen in silver, which causes water nucleation and mechanical instability. However, silver may be able to provide a high conductivity pathway through another material. Systems in which silver wires are passed through nickel and silver powder is melted into holes drilled in nickel have been examined. Figure 26 shows the cross-section of a Ni specimen where Ag has been melted in a hole drilled in the Ni. After exposure there is some porosity in

the silver and it appears the grain boundaries are delineated with pores far into the silver. Importantly, despite the porosity, the specimen had resistance values typical of a metal when measured at room temperature following exposure. In this configuration the Ni provides the physical integrity of the interconnect and the silver only provides the conduction path through the scale.
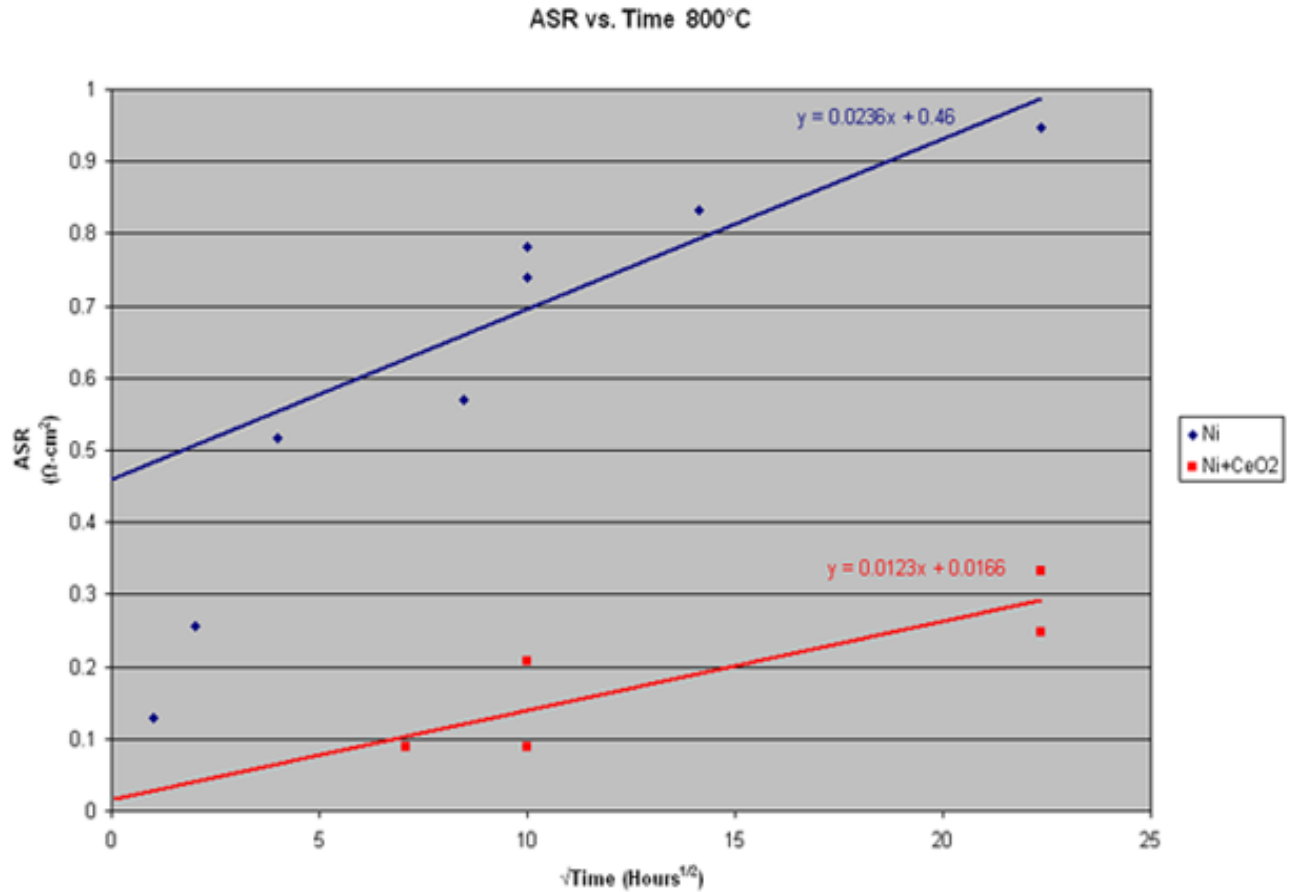

ASR vs. Time 800°C

$y = 0.0236x + 0.46$

$y = 0.0123x + 0.0166$

Figure 24.   ASR as a function of the square root of the oxidation time at 800˚C for pure Ni and CeO$_2$-doped Ni.
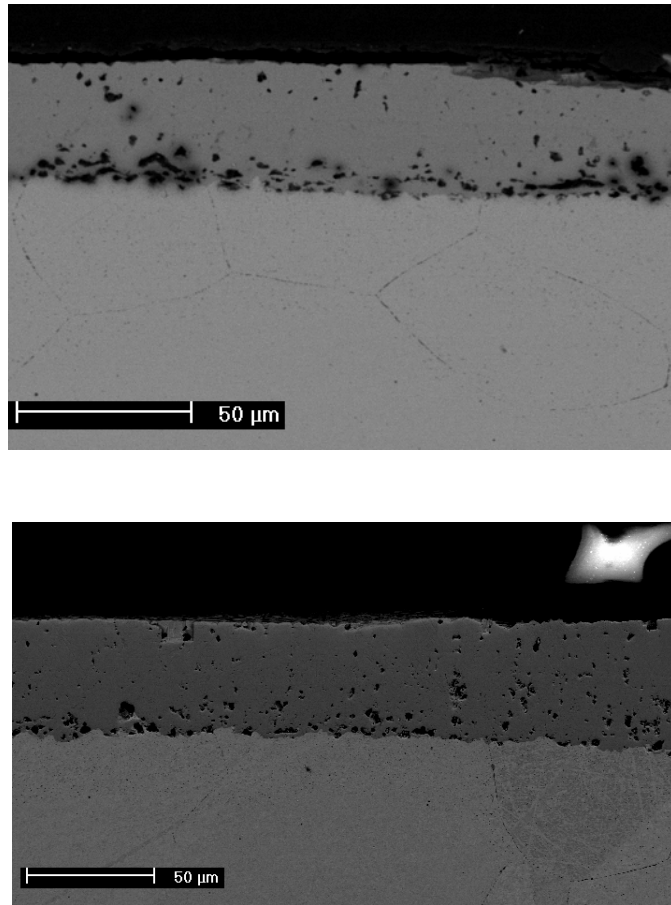
Figure 25   Cross-sections of Ni 200 tubes exposed for 600 hours at 800˚C. The top specimen was exposed with dry air inside and outside the tube. The bottom specimen was exposed with Ar-10%H_2O - 4%H_2 inside the tube and dry air on the outside. The micrograph was taken from the side exposed to air.

Task 4: Development of Durable Contacting Material (WVU)

Sterling silver was tested in a high-temperature exposure experiment alongside pure silver to gain an understanding of the performance of copper-oxide in protecting against silver evaporation. Samples were weighed on a weekly basis and the observed mass changes were used to determine the reduction in thickness of the samples. Results from the evaporation data are shown in Figure 27.

Very early on it appears that all samples exhibit similar evaporation behavior, however, after several weeks it appears that the rate of loss for the pure silver samples is lower than the sterling silver sample. This trend continued throughout the 27-week experiment. This is an unexpected result as the copper-oxide formed during oxidation was intended to protect the silver and reduce the rate of evaporation of the samples.
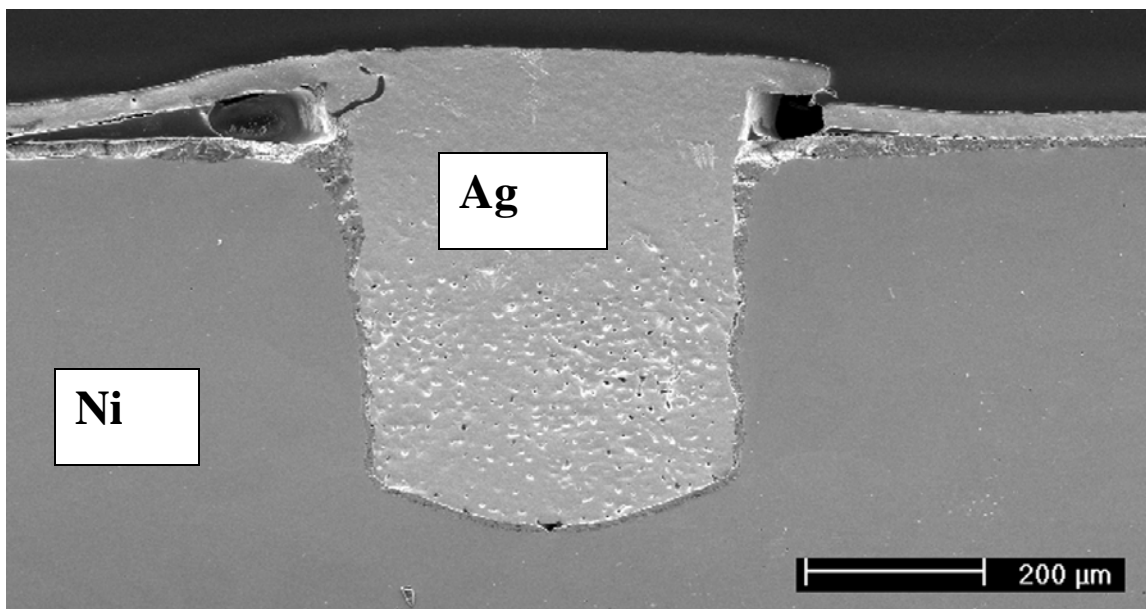
Figure 26.　　Silver Via, 800°C 100 Hours, exposed under dual atmospheric conditions. The upper surface was exposed to dry air while the lower surface was exposed to simulated anode gas of Ar-10%H_2O-4%H_2.

Samples are also regularly examined for surface changes due to high-temperature exposure. Examples of SEM micrographs for exposed samples are shown in Figure 28. As shown, the sample surfaces exhibit clearly different behavior which may affect the evaporation rates of the samples.

Time-series analysis was conducted to evaluate a particular section of the surface of a sterling silver sample during high-temperature exposure. This analysis allows a better understanding of the evaporation characteristics of the samples as well as any interaction between the copper-oxide particles and silver in the sample. Figure 29 illustrates a time-series of backscatter micrographs for a typical sterling silver sample. The main changes that can be seen on the surface of the sample are the migration and agglomeration of the copper-oxide particles at the surface; silver can also be seen to recede at the edges of some copper-oxide particles indicated in the images. This indicates that copper-oxide is volatile under SOFC operating conditions to act as an appropriate protective oxide in the cermet. Further analysis of the interior regions of the exposed sterling silver samples revealed the coarsening of copper-oxide particles beneath the surface of the sample, indicating that this coarsening behavior may be an intrinsic phenomenon related to copper-oxide when exposed to an oxidizing environment. Figure 30 illustrates an example of SEM backscatter imaging of a typical interior section of a sterling silver sample after high-temperature exposure.

Some basic analyses were conducted using the SEM micrographs from the exposure experiments. It was noted that the silver visible between the copper-oxide particles on the surface of the sterling silver samples exhibited a much higher step-density, number of observable steps per unit length, than was observed at the surface of

the pure silver samples. Figure 31 shows the difference in step-density observed for each type of sample.

In Summary, based on data collected over the six-month evaporation experiment as well as microstructure changes observed using time-series SEM analysis, it appears that copper oxide may be too volatile for use as a protective oxide in a contacting cermet for a solid-oxide fuel cell. The data indicates that the sterling silver sample lost mass more rapidly than its pure silver counterpart, possibly due to the inability of the surface microstructure to reach the least favorable orientation to evaporation. SEM analysis showed a much higher step density for sterling silver than for pure silver after high temperature exposure, illustrating a clear difference in surface microstructure, which could also affect the sample's vaporization rate. Time-series SEM analysis also illustrated migration and agglomeration of copper-oxide particles both at and below the surface of the sterling silver samples indicating possible issues of volatility with regard to copper-oxide. Strontium-doped lanthanum manganite (LSM) and cerium-oxide will likely be the focus of future work as they may possess better properties with regard to electrical conductivity as well as stability under SOFC operating conditions than those observed in copper-oxide.
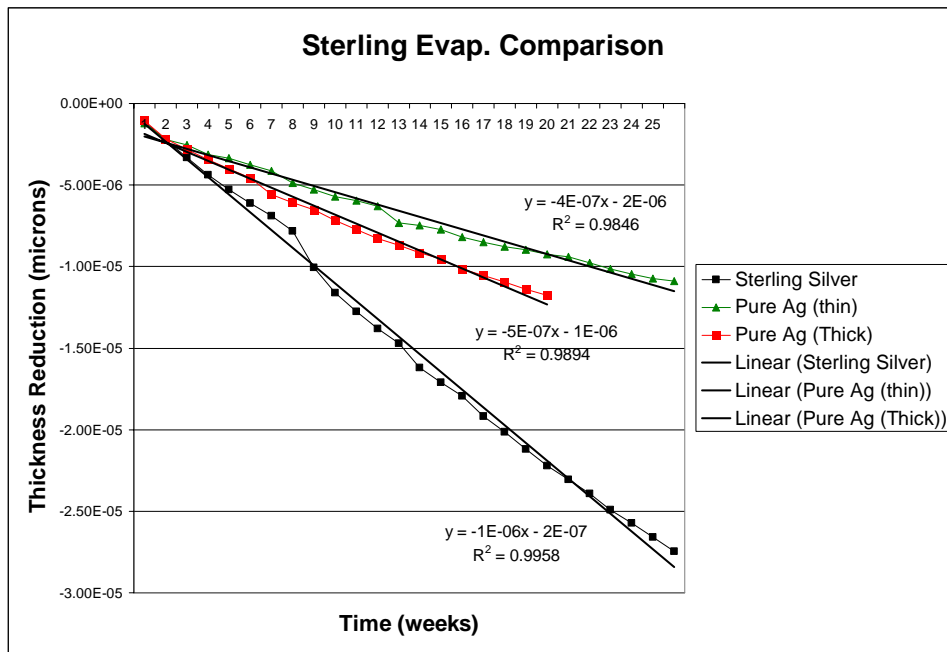
Figure 27.   Comparison of thickness reductions for various silver samples.
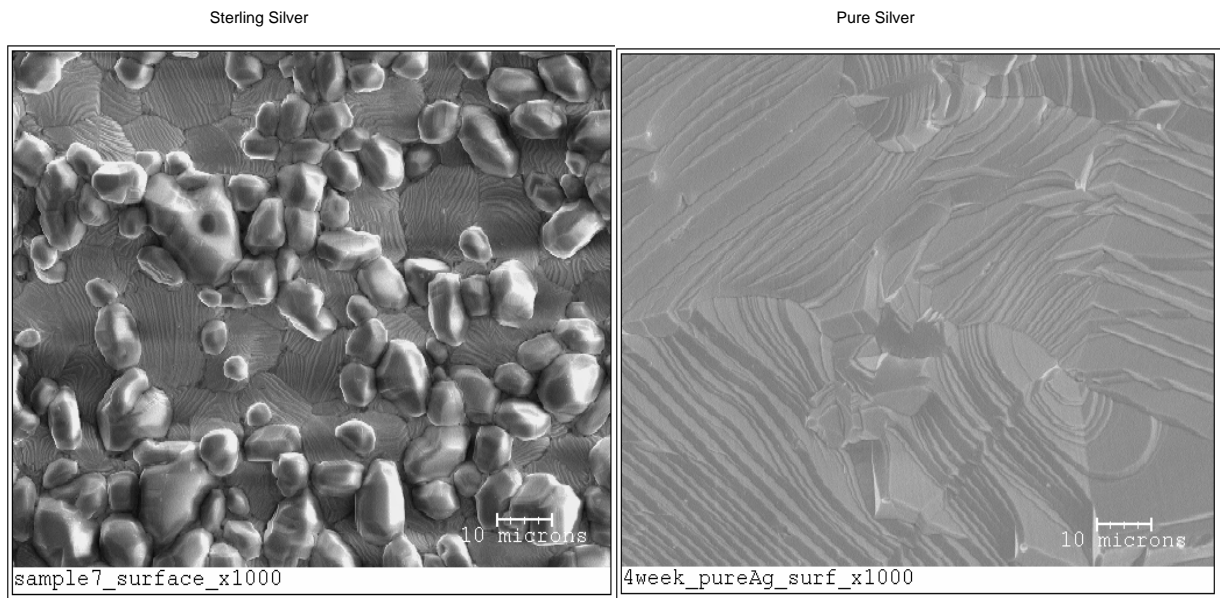
Figure 28.   SEM micrograph comparison of sterling and pure silver samples after
              3- week high-temperature exposure.

12-hours   2-weeks   4-weeks

6-weeks   8-weeks   10-weeks

12-weeks   14-weeks   16-weeks
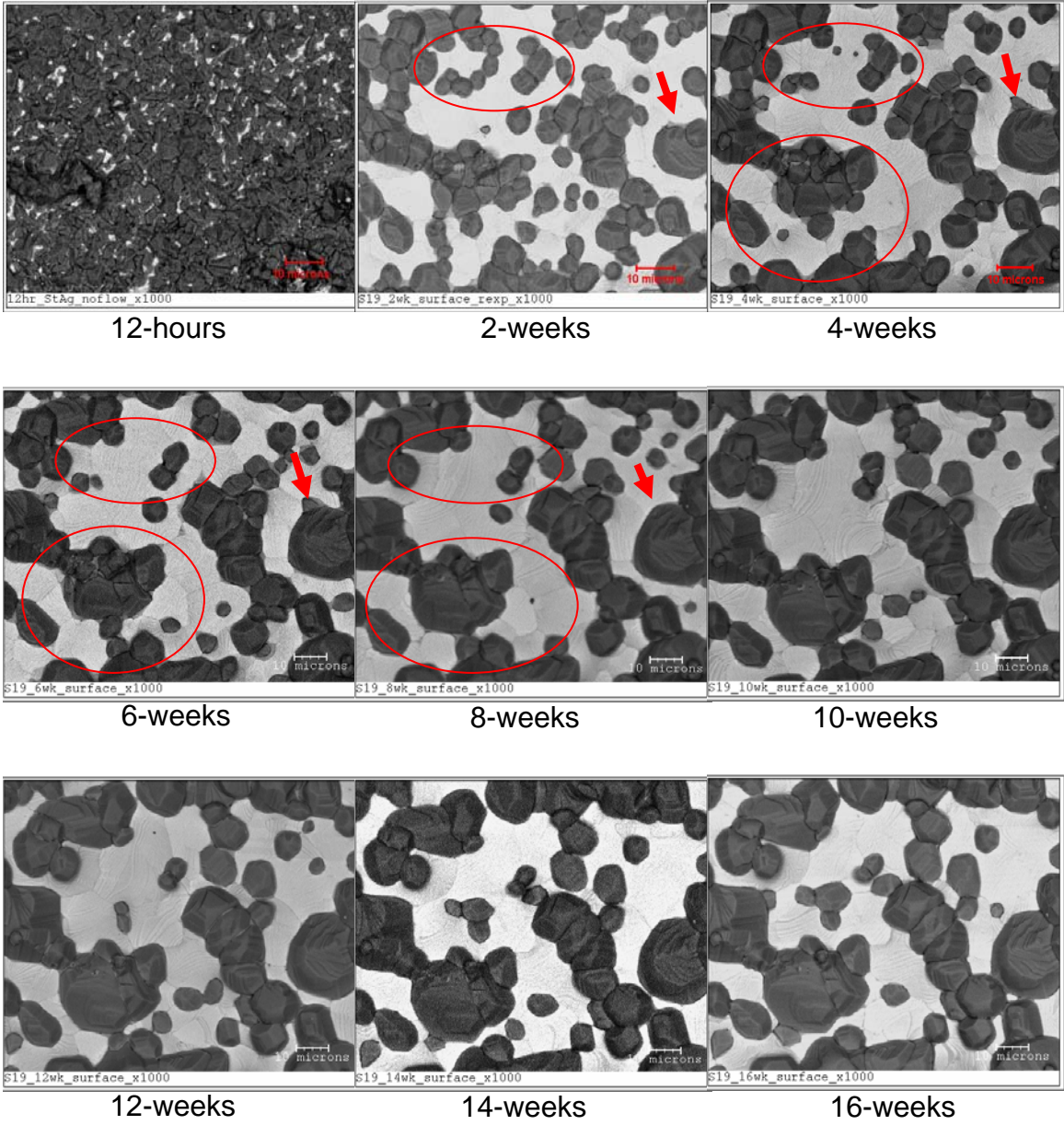
Figure 29.   Time-series analysis of sterling silver surface during high-temperature.

1-week

3-weeks

5-weeks

7-weeks

10-weeks

13-weeks

17-weeks
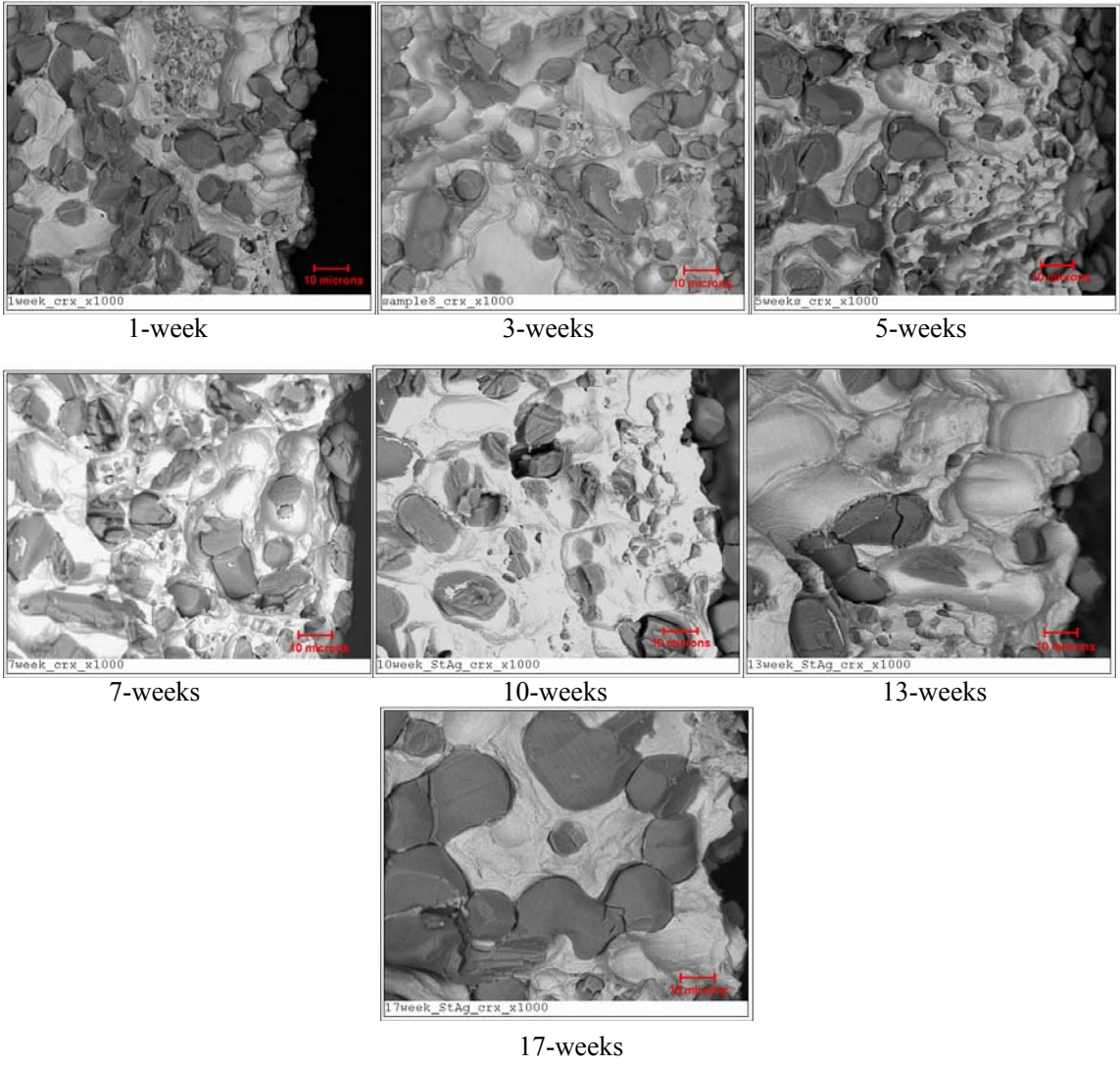
Figure 30. Fracture surfaces of sterling silver samples after high-temperature exposure.
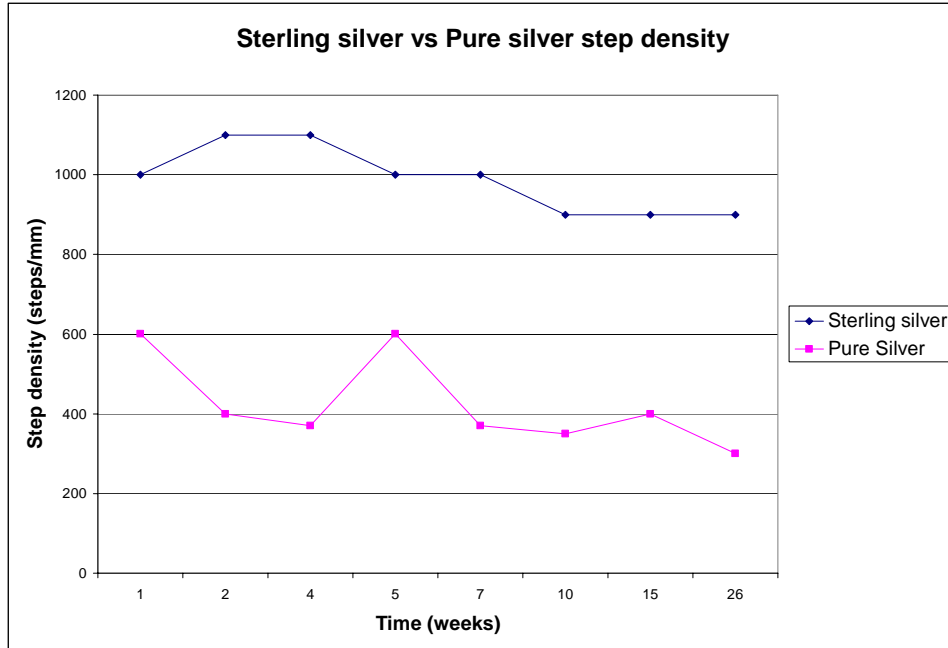
Figure 31. Step-densities for pure silver and sterling silver samples.

REFERENCES

1. A. Vasinonta and J. L. Beuth, Eng. Fracture Mech., 68, 843 (2001).
2. R. A. Handoko, J. L. Beuth, G. H. Meier, F. S. Pettit, and M. J. Stiger, "Mechanisms for Interfacial Toughness Loss in Thermal Barrier Coating Systems," *Durable Surfaces* (D.R. Mumm, M.E. Walter, O. Popoola and W.O. Soboyejo, eds.), Proceedings of the Materials Division Symposium on Durable Surfaces, (2000) ASME International Mechanical Engineering Congress and Exposition, Orlando, November 2000, Trans Tech Publications, Switzerland, 2001, p. 165.
3. G. H. Meier and F. S. Pettit, "Fundamental Studies of the Durability of Materials for Interconnects in Solid Oxide Fuel Cells", Phase I Topical Report, DOE Award: DE FC26 02NT41578, June 30, 2003.
4. N. Dhanaraj, J. L. Beuth, G. H. Meier, F. S. Pettit, J. Hammer, and S. J. Laney, "Interfacial Fracture Testing to Evaluate, the Durability of SOFC Interconnect Alloys", Materials for the Hydrogen Economy (J. J. Petrovic, I. E. Anderson, T. M. Adams, G. Sandrock, C. F. Legzdins, J. W. Stevenson, and Z. G. Yang, eds.), Proc. Materials Science and Technology 2005, Pittsburgh, September 2005, pp 165-175.

Appendix A

The Oxidation of Ferritic Stainless Steels in Simulated

Solid Oxide Fuel Cell Atmospheres

J. E. Hammer, S. J. Laney, R. W. Jackson, K. Coyne, F. S. Pettit, and G. H. Meier

Department of Materials Science and Engineering

University of Pittsburgh

Pittsburgh, PA

ABSTRACT

The cyclic oxidation of a variety of chromia-forming ferritic stainless steels has been studied in the temperature range 700-900°C in atmospheres relevant to solid oxide fuel cell operation. The most detrimental environment at 800°C and 900°C was found to be air with 10% water vapor. This resulted in excessive oxide spallation or rapid scale growth. Impurities in the alloys, particularly Al and Si, were found to have a significant effect on the oxidation behavior. Oxide growth was slow at 700°C but the higher Cr-content alloys were observed to form sigma-phase at this temperature. The sigma phase formation was accelerated by higher silicon contents and, remarkably, by the presence of water vapor in the exposure environment. Alloys containing Mn were observed to form an outer layer of $MnCr_2O_4$ over the chromia scale. The potential for this overlayer to suppress reactive evaporation of the chromia scales has been analyzed.

INTRODUCTION

Solid oxide fuel cells provide a potential way to generate electricity with high efficiency and low pollution. The operating principles of fuel cells have been known for over 100 years and low-temperature fuel cells provided the electric power on all the Gemini and Apollo spacecraft. However, fuel cells have not achieved widespread commercial use for a number of economic and technical reasons.

One of the most important technical challenges for planar solid oxide fuel cells, which operate in the temperature range 700-900°C, is the design of interconnects (current collectors). These components, in addition to drawing off the electric current, must separate the anode compartment of one cell from the cathode compartment of the adjacent cell. This means that one side of an interconnect is exposed to the fuel, typically hydrogen or hydrocarbons in which the oxygen partial pressure is low, and the other side is exposed to the oxidant, which is typically air. The requirements for interconnects have been reviewed recently[1-4]. Interconnect material requirements include a variety of physical, chemical, and electrical properties. The optimal interconnect material would have the following properties:

1. Low electrical resistivity.

2. Impermeability to anode and cathode gases.

3. Stability in both anode and cathode gases under thermal cycling conditions.

4. Chemical compatibility with other cell components.

5. Close match in coefficient of thermal expansion with other components.

6. Good mechanical properties.

7. High thermal conductivity.

8. Ease of fabrication.

9. Low cost.

Metallic interconnects are attractive in that they have favorable values of properties 2, 6, 7, 8, and 9. Metallic materials also have low electrical resistance but they react with the gases to form oxide layers, which generally have high electrical resistivity. Oxidation resistant alloys are designed to form one of three protective oxides: alumina, silica, or chromia. Of these the electrical resistivities of alumina and silica are much too high for interconnect applications. Exact values of the resistivities of oxides depend on numerous factors but approximate values of the resistivities of silica, alumina, and chromia at 800˚C in air are presented in Table 1.

Chromia scales grow much faster than alumina or silica but the resistivity of chromia is sufficiently lower to allow chromia-forming alloys to be considered as a "compromise" as interconnects. The coefficient of thermal expansion of chromia-forming ferritic steels matches that of the ceramic components, particularly in the case of the common anode supported SOFCs. The oxidation behavior of this class of alloy under conditions relevant to SOFC operation is the subject of this paper.

Previous Studies of Metallic Interconnect Materials

A number of studies have been conducted on chromia-forming metallic interconnect materials, particularly with regard to their stability in the cathode and anode gases.

Cathode Gas

The cathode gas provides the oxidant for the cell and will generally consist of air. England and Vircar[5] oxidized thin foils of the commercial Ni-base alloys Inconel 625, Inconel

718, Hastelloy X, and Haynes 230 in air under isothermal conditions at temperatures between 800 and 1100°C. All the alloys formed scales consisting essentially of chromia and the apparent parabolic rate constants varied over more than an order of magnitude e.g. between 1×10^{-15} and 2.8×10^{-14} g^2/cm^4s at 800°C.

Quadakkers et al[6] have studied chromium-based alloys since they have lower coefficients of thermal expansion than the nickel based alloys. The addition of a Y_2O_3 dispersion improved the mechanical strength and lowered the oxidation rates of the alloys. A significant problem with Cr (and chromia-forming alloys) which has been recognized for many years[7] is the reactive evaporation of chromia scales. This is a particular problem in the cathode gas since the CrO_3 partial pressure increases with oxygen partial pressure, as illustrated in Figure 1[8]. The volatile species are reduced at electrochemically active sites on the cathode during SOFC operation, which inhibits the required oxygen reduction[9]. Analysis of the Cr vapor species[10] indicates water contents above about 0.01% in air result in partial pressures of $CrO_2(OH)_2$ which exceed the partial pressure of CrO_3. This will be discussed in more detail in a subsequent section of this paper.

A number of investigators have studied the behavior of ferritic stainless steels as interconnect materials since they have a good thermal expansion match with typical ceramic components of SOFCs. Huang et al[11] studied the isothermal oxidation of ferritic Fe – 26 wt% Cr alloys in air reporting a k_P of 8.8×10^{-14} g^2/cm^4s at 800°C. Brylewski et al[12] reported a similar value of 8.5×10^{-14} g^2/cm^4s for Fe-16 wt% Cr. Quadakkers et al[13, 14] have developed model alloys based on the philosophy of:

i. Using La additions to slow the growth rate of the chromia scale and improve the adherence of the scale to the alloy.

ii. Making additions of Ti and Mn to form spinels on the chromia scale to reduce CrO_3 evaporation.

iii. Maintaining Al and Si levels as low as possible to prevent the formation of electrically insulating alumina or silica layers.

(The last point is quite important in that many commercial Fe- and Ni-base alloys, which are nominally chromia-formers, contain sufficient Al and/or Si so that, under certain exposure conditions, alumina or silica can form between the chromia layer and the alloy.)

The work of Quadakkers et al has lead to the commercialization by ThyssenKrupp VDM of a ferritic alloy, Crofer 22 APU, specifically designed for fuel cell applications. Yang et al[15] have reported the results of cursory studies of the oxidation behavior of this alloy. The area specific resistance (ASR) was reported in Ref. 11 for scales formed during 24 hour exposures in air at 900°C. The ASR measured at 900°C with Ag electrodes was on the order of 0.02 Ωcm^2. Quadakkers et al[13] performed in-situ measurements of the ASR of chromia scales forming at 800˚C on one of the modified ferritic alloy alloys described above. The ASR (measured at 800˚C) after 100 hours of oxidation was approximately 0.01 Ωcm^2 and increased to approximately 0.1 Ωcm^2 after 8000 hours.

Anode Gas

The anode gas consists of the fuel (typically hydrogen or hydrocarbons) and the products of combustion (water vapor and, possibly, CO and CO_2). England and Vircar[16] oxidized thin

foils of the commercial Ni-base alloys Inconel 625, Inconel 718, Hastelloy X, and Haynes 230 in hydrogen, which was saturated with water at 40°C under isothermal conditions at temperatures between 700 and 1100°C. The growth rate of the chromia scales at 800°C were higher than those observed in air[5] for the same alloys and the electrical resistance of the scales was higher than for those formed in air.

Quadakkers et al[17-19] have studied pure Cr and yttria-dispersed Cr at 950 and 1000°C in $Ar/H_2/H_2O$ mixtures. They too observed larger mass gains in H_2/H_2O mixtures but correctly point out that this is the result of mass losses from CrO_3 evaporation in air, which are minimal at the reduced oxygen partial pressures in H_2/H_2O mixtures. One rather surprising result of this study was that the chromia scales were substantially more adherent when formed in H_2/H_2O mixtures than in dry air. It is well documented that spallation of alumina scales is accelerated by water vapor[20, 21] so these results for chromia are in need of further study.

Quadakkers et al reported the chromia scales formed on ferritic stainless steels in simulated anode gas at 800°C were thinner than those formed in air[13, 14]. Brylewski et al[12] reported similar values of k_P for oxidation in $94H_2/6H_2O$ and air.

Dual Atmosphere Exposures

Yang et al[22] observed a change in the oxide formed on stainless steels in air when a simulated anode gas was present on the opposite side of the specimen. They hypothesized that this is the result of H diffusing from the anode side and affecting the oxide growth on the cathode side.

This paper presents results for the oxidation of ferritic stainless steels in single atmospheres which form a baseline for understanding oxidation in dual atmosphere conditions.

EXPERIMENTAL

Cyclic Oxidation

The cyclic oxidation of a range of ferritic stainless steels has been evaluated under a range of conditions pertinent to fuel cell operation. The alloys were: (Nominal compositions in Wt%)

- E-BRITE (Fe-26 Cr-1 Mo - 0.2 Si)

- 26Cr Ferritic (Fe-26Cr-1-Mo-2Mn-4.5Ni-1Si-1Al)

- AL 453 (Fe-22 Cr-0.6 Al-0.3 Mn + 0.1Ce/La)

- Crofer22 APU (Fe-22Cr-0.5Mn-0.08 Ti-0.016P-0.06 La)

The exposure conditions included:

- T = 900°C and 700°C (Limited experiments were performed at 800˚C)

- One-Hour Cycles (45 min. hot, 15 min.cold)

- Atmospheres

-     Dry Air (Simulated Cathode Gas)

-     Air + 0.1 atm H_2O (Simulated Moist Cathode Gas)

-     Ar/H_2/H_2O (Simulated Anode Gas)

        (p_{O_2} = 10^{-17} atm at 900°C and 10^{-20} at 700°C)

The exposure apparatus used for these exposures is shown schematically in Figure 2.

Specimen Characterization

Following exposure the oxidation products and alloy microstructure were characterized using x-ray diffraction (XRD), scanning electron microscopy (SEM) and energy dispersive x-ray analysis (EDS).

RESULTS AND DISCUSSION

Cyclic Oxidation at 900°C

The experiments at 900°C were designed as *accelerated tests*. The duration of the test was 2000 cycles, which corresponded to 1500 hours at temperature (900°C). Based on the temperature dependence of the parabolic rate constants reported for oxidation of Fe-26 wt% Cr in air [11], exposure for 1500 hours at 900°C should result in a chromia scale thickness comparable to that formed after about 16,000 hours at 800°C. Thus, if one can assume the same oxidation mechanisms at 800 and 900°C, these experiments should simulate an exposure at 800°C for 16,000 hours of hot time. In the latter case 2000 cycles would correspond to the specimen being cycled to room temperature with a frequency of approximately twice per day. Since cyclic degradation can depend on cycle frequency, it is not clear how many cycles at 800°C would produce similar degradation. Correlation between the accelerated tests with operating conditions is an ongoing theme of this project.

The oxidation kinetics for exposure in dry air (simulated cathode gas) are presented in Figure 3. The mass gains for Crofer22 APU correspond to literature values for the isothermal

oxidation of ferritic alloys in air [11] while the mass gains for Fe-26Cr ferritic are somewhat

smaller and those for Al 453 are somewhat larger. The oxidation curves do not give evidence for

substantial scale spallation. The results for duplicate specimens under all exposure conditions

were in good agreement. Therefore, subsequent plots will present the average data for the two

specimens in a single curve.

Figure 4 presents the corresponding oxidation kinetics in simulated anode gas. The mass

gains for Fe-26 Cr ferritic and Crofer are similar and are similar to those reported for isothermal

oxidation of ferritic alloys in hydrogen-water vapor atmospheres [12]. The mass gains for AL 453

are larger.

Figure 5 presents the oxidation kinetics in air containing 10% water vapor. This gas does

not directly simulate a fuel cell atmosphere. However, with the use of air, there are the

possibilities that the air has not been dried, small seal leakages occur, or hydrogen diffuses to the

cathode side and reacts with oxygen; therefore, it is not unreasonable to anticipate that the

cathode gas may contain water vapor in some situations. The mass changes for Fe-26Cr ferritic

are similar to those in dry air. However, the mass gains are far larger for Crofer, and AL 453

than those observed in either of the other two atmospheres. These observations are consistent

with measurements of oxide thickness (presented in Table 2) and metallographic observations to

be described below. It is important to note that the simple analysis in the table can be

compromised by both specimen deformation and internal oxidation, particularly in the case of

Crofer, yielding significant differences between measured and calculated values.

Figure 6 presents cross-section micrographs of Fe-26Cr ferritic after exposures in all

three atmospheres at 900°C. The scales are similar and are consistent with the similar oxidation

kinetics observed in the three environments. The external scale consists of Cr_2O_3 and there is a

fine distribution of Al-rich precipitates in the alloy below the scale.   Figure 7 shows more detail

of the alloy/scale interface for Fe-26Cr. There is a substantial amount of silica at this interface.

It is not clear if this phase was responsible for the lack of acceleration of scale growth for

exposures in air + 10% H_2O. However, it is believed that oxide spallation is primarily

responsible for the thinner scales observed on Fe 26 Cr in this atmosphere. Figure 8 shows a

macroscopic surface photograph of Fe-26Cr ferritic after 847 cycles showing circular spalled

areas. Other areas were also observed where there were circular areas of thin oxide, which

appeared to have reformed in spalled areas on subsequent cycles. Spalling is also consistent with

the data in Table 2. The experimental mass gain for Fe-26Cr Ferritic in wet air is substantially

smaller than that calculated from the oxide thickness. The mass changes in air + 0.1 atm H_2O

may also be influenced by evaporation of $CrO_2(OH)_2$, as will be discussed below.

Figure 9 presents cross-section micrographs of Crofer after exposure in all three

environments. The specimen exposed in dry air had a continuous layer of $MnCr_2O_4$ at the

scale/gas interface with a chromia layer beneath. Figure 10 indicates some internal oxidation

below the chromia layer. These oxides were found to be Al-rich, although Al is not listed as an

intentional component of this alloy. The specimen exposed in wet air exhibited a very thick

scale, which is consistent with the large mass gain in this atmosphere. However, The $MnCr_2O_4$ is

present as discontinuous particles at the scale/gas interface rather than as a continuous layer.

Figure 11 shows a macroscopic photograph of a Crofer specimen oxidized in wet air. This

specimen is severely warped, presumably because of the extensive oxidation. Specimens

exposed in dry air and simulated anode gas did not exhibit this deformation. The specimen

exposed in simulated anode gas showed very little $MnCr_2O_4$ at the scale/gas interface and the

chromia scale appeared somewhat 'friable". The micrograph of this specimen in Figure 10 also

shows an inclusion running parallel to the rolling direction of the sheet. This was identified as a La-rich oxide. Similar inclusions, as well as Ti-nitrides were found throughout the as-received alloy.

Figures 12 and 13 present cross-section micrographs of AL 453 exposed in the three environments. The striking feature in all environments is the extensive internal oxidation of Al below the chromia scale. Table 2 indicates the measured mass gain of this alloy in all three environments is substantially larger than that calculated from the thickness of the external scale. The oxygen uptake in forming the internal oxides is responsible for this difference. An additional feature of this alloy is the appearance of a layer of metallic Fe-Cr between the internal oxidation zone and the external chromia scale. The origin of this layer has not yet been determined. One possibility is extrusion of metal out from the zone of internal oxidation as the alumina precipitates form. This phenomenon is discussed more fully below.

In summary, accelerated cyclic oxidation testing at 900°C has been investigated. The most detrimental environment was found to be air with 10% water vapor. This resulted in excessive oxide spallation from Fe-26Cr ferritic and rapid scale growth on Crofer22 APU and AL 453. Huczkowski et al.[23] have explained the accelerated oxidation of Crofer as resulting from the internal oxidation of Si and Al causing metallic protrusions. This presumably increases the effective surface area of the alloy. However, Figure 9 does not indicate a significant difference in the amount of internal oxidation or metal protrusions between the specimens exposed in dry air and air plus water vapor. Therefore, it is not clear why the scale on Crofer grows faster in the presence of water vapor.

Cyclic Oxidation at 800˚C

The accelerated oxide growth rate on Crofer at 900˚C, when exposed in air with 10% water vapor, prompted further investigation of this phenomenon at 800˚C. In addition to Crofer several other alloys were studied. These included JS-3, a model alloy (Fe-23Cr-0.39Mn-0.05Ti-0.09La, wt%),with Si and Al contents less than 0.01 wt%, and a second heat of Crofer (termed "New Crofer") in which more care was used to reduce the Al and Si impurities, both provided by Dr. J. Quadakkers, Forschungszentrum, Jülich. E-brite and Fe-26Cr-Ferritic were also included in this experiment. The cyclic oxidation kinetics in air with 10% water vapor are presented in Figure 14. The Crofer from the original heat exhibited accelerated oxidation similar to that at 900˚C whereas the Crofer from the second heat (with lower Si and Al impurities) and JS-3 did not exhibit this tendency. The 26 Cr Ferritic and E-brite began to show mass losses after short times as a combined result of spallation and scale evaporation.

Figure 15 is a cross-section micrograph of Crofer after exposure for 2000 hours. It shows significant internal oxidation of Al and silica forming at the scale alloy interface. Figure 16 shows a cross-section of the purer Crofer from the second heat. There is substantially less internal oxidation but there is still a significant amount of metal protruding into the scale. Figure 17 shows a cross-section of JS-3. There is some internal oxidation but no metal protruding into the scale. Huczkowski et al.[23] observed most of the internal oxides to be TiO_2. However, some of the particles in Figure 17 are alumina and silica.

Cyclic Oxidation at 700˚C

Figures 18, 19, and 20 show the mass change vs. exposure time for samples at 700°C in dry air, $Ar/H_2/H_2O$, and air +0.1 atm H_2O, respectively. In all cases, AL 453 exhibited the

largest mass gains, followed by Crofer and the 26 Cr Ferritic alloy. In the moist air environment, the 26 Cr alloy showed small initial mass gains, but began to lose mass after ~400 cycles.

Figure 21 presents cross-section micrographs of Fe-26Cr Ferritic after exposures in all three atmospheres at 700°C. The scales are similar. The external scale consists of Cr_2O_3 and there is a fine distribution of Al-rich precipitates in the alloy below the scale and Si-rich particles are present at the scale/alloy interface.   The experimental mass change for Fe-26Cr Ferritic in wet air was observed to go negative after about 400 cycles. As was the case of the 900˚C experiments, the mass changes in air + 0.1 atm H_2O may be influenced by evaporation of $CrO_2(OH)_2$, as will be discussed below. All of the Fe-26Cr specimens exposed at 700˚C formed sigma-phase. The details of the formation of this undesirable brittle phase will be discussed in detail below.

Figure 22 presents cross-section micrographs of Crofer after exposure in all three environments. The specimen exposed in dry air had a layer of $MnCr_2O_4$ at the scale/gas interface with a chromia layer beneath although the layer was not as well developed as that at 900˚C. There was also formation of internal Al-rich oxides at this temperature and these oxides had a tendency to form into semi-continuous bands. Bands of Si-rich oxides formed at the alloy/chromia interface.

Figure 23 presents cross-section micrographs of AL 453 exposed in the three environments. In all environments there was extensive internal oxidation of Al below the chromia scale and these oxides formed virtually continuous films. Metallic regions were observed above the internal Al-oxides for the specimens exposed in air but were absent for exposures in SAG.

Oxide Evaporation

A significant problem with Cr (and chromia-forming alloys), which has been recognized for many years[7], is the reactive evaporation of chromia scales. The formation of CrO_3 by the reaction

$$Cr_2O_3(s) + \tfrac{3}{2}O_2(g) = 2CrO_3(g) \tag{1}$$

becomes significant at high temperatures and high oxygen pressures. The oxygen pressure effect is illustrated in Fig. 1[8]. (In the presence of water vapor, the predominant evaporating species may become $CrO_2(OH)_2$ whose partial pressure increases with increasing H_2O partial pressure, as indicated in Figure 24[10].) The evaporation of CrO_3 results in the continuous removal of the protective Cr_2O_3 scale so the diffusive transport through it is rapid. The effect of the volatilization on the oxidation kinetics has been analyzed by Tedmon[7]. The instantaneous change in scale thickness is the sum of two contributions: thickening due to diffusion and thinning due to volatilization.

$$\frac{dx}{dt} = \frac{k_d'}{x} - k_s' \tag{2}$$

where k_d' is a constant describing the diffusive process and k_s' describes the rate of volatilization. This equation can be rearranged to yield

$$\frac{dx}{\left(\dfrac{k_d'}{x} - k_s'\right)} = dt \tag{3}$$

which, upon integration, yields:

$$\frac{-x}{k_s'} - \frac{k_d'}{k_s'^2} \ln\left(k_d' - k_s'x\right) + C = t \tag{4}$$

where C is an integration constant to be evaluated from the initial conditions. Taking $x=0$ at $t=0$

$$t = \frac{k_d'}{k_s'^2}\left[-\frac{k_s'}{k_d'}x - \ln\left(1 - \frac{k_s'}{k_d'}x\right) \right] \tag{5}$$

Initially, when the diffusion through a thin scale is rapid, the effect of CrO_3 volatilization is not significant but, as the scale thickens, the rate of volatilization becomes comparable and then equal to the rate of diffusive growth. This situation, *paralinear oxidation*, results in a limiting scale thickness, x_o, for which $dx/dt = 0$. Setting this condition in equation 3 yields

$$x_o = \frac{k_d'}{k_s'} \tag{6}$$

This problem, which is more serious in rapidly flowing gases, is one of the major limitations on the high temperature use of Cr_2O_3 forming alloys and coatings.

Evaporation is a particular problem in the cathode gas of solid oxide fuel cells (SOFCs) since the CrO_3 partial pressure increases with oxygen partial pressure, as illustrated in Figure 1. The volatile species are reduced at electrochemically active sites on the cathode during SOFC operation, which inhibits the required oxygen reduction[8]. Analysis of the Cr vapor species[10] indicates water contents above about 0.1% in air result in partial pressures of $CrO_2(OH)_2$ which exceed the partial pressure of CrO_3. Thus, maintaining the cathode gas as dry as possible is desirable.

Figures 1 and 24 are constructed for unit activities of Cr and Cr_2O_3, i.e. evaporation at high oxygen partial pressures occurs from pure chromia. However, examination of the equilibrium constant for reaction 1

$$K_1 = \frac{p^2_{CrO_3}}{a_{Cr_2O_3}\, p^{3/2}_{O_2}} \qquad\qquad (7)$$

shows that, for a fixed oxygen partial pressure, the partial pressure of CrO_3 will decrease as the activity of chromia is reduced. Other things being equal, the evaporation rate should be directly proportional to the CrO_3 partial pressure. Therefore, the presence of an outer oxide layer with reduced chromia activity could slow the scale evaporation. Coatings of $La_{0.9}Sr_{0.1}CrO_3$ have been applied to ferritic alloys to limit CrO_3 evaporation[24].

The formation of a complex oxide over a chromia layer can also occur naturally during oxidation of some alloys. Spinels (MCr_2O_4) have been observed to form over chromia scales growing on alloys containing the transition metals Fe, Ni, Co, and Mn. In some cases the spinels form before the chromia layer becomes continuous (transient oxidation) but in others the spinel

forms by outward diffusion of the transition metal through the chromia layer. Outer layers

containing Fe and Mn have been known to form on stainless steels for many years[25]. This is

somewhat remarkable since the steel usually only contain about 1 % Mn. The high mobility of

Mn ions in chromia is also in agreement with theoretical studies[26]. Crystal field theory

calculations of the difference in stabilization energies for cations on octahedral versus tetrahedral

sites in the hexagonal oxide ion sublattice of chromia lead to the prediction that the mobility of

divalent cations should increase in the order $Ni^{2+} : Cu^{2+} : Co^{2+} : Fe^{2+} : Mn^{2+}$ [26]. Figure 9 shows

cross-sectional micrographs of Crofer 22, which contains approximately 0.5 wt% Mn, after

exposure at 900˚C in dry air. An outer layer of $MnCr_2O_4$ can be observed at the scale/gas

interface. This layer is particularly well developed for the specimen oxidized in dry air.

The diffusion properties in the chromia will control the development of an outer spinel

layer but the thermodynamic properties of the individual spinels will determine how much they

decrease the activity of chromia. Tretjakow and Schmalzried[27] performed an extensive study of

the thermodynamic properties of the spinels of Cr with Fe, Ni, Co, Mg, and Cu over the

temperature range 1000 to 1500K. They found that the standard Gibbs free energy change for

the reaction

$$MO + Cr_2O_3 = MCr_2O_4 \qquad\qquad (8)$$
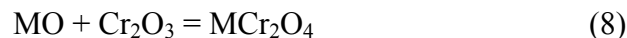
was very similar for all the spinels, which would suggest they all would be similarly effective in

lowering the activity of chromia. Unfortunately, Mn was not included in this study and no data

are listed for $MnCr_2O_4$ in the available thermodynamic data compilations [28]. In the present

study the available thermodynamic data[28] were used to catalog the properties of the spinels for

which data are available and then to estimate the thermodynamic data for $MnCr_2O_4$. The data were used to estimate the partial pressure of CrO_3 which would stand in equilibrium with each spinel at typical SOFC operating temperatures.

Thermodynamic Calculations

The standard Gibbs free energies of formation ($\Delta G°$) for Cr_2O_3, Al_2O_3, FeO, NiO, CoO, MnO, MgO, $FeCr_2O_4$, $NiCr_2O_4$, $CoCr_2O_4$, $MgCr_2O_4$, and $MnAl_2O_4$, were taken from reference 28 over the temperature range of interest 1000 to 1300K. Data for the reaction

$$MnCr_2O_4 + Al_2O_3 = MnAl_2O_4 + Cr_2O_3 \qquad (9)$$
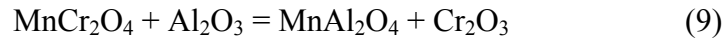
were reported at one temperature (1373K) in reference 29. This allowed the calculation of $\Delta G°$ for $MnCr_2O_4$ at 1373K and estimates of the standard entropy change ($\Delta S°$) for the reaction

$$MnO + Cr_2O_3 = MnCr_2O_4 \qquad (10)$$

were used to extrapolate the data to lower temperatures. Figure 25 shows $\Delta G°$ for reaction 8 for Fe, Ni, Co, and Mg. The data for Fe, Ni, and Mg are similar while the values for Co are somewhat more negative. Figure 26 presents the extrapolated data for Mn with the data for Ni as a basis for comparison. It is clear that $MnCr_2O_4$ is much more stable than the other spinels. The data from Figure 26 were used to calculate the equilibrium constant for reaction 10 which

allowed the calculation of the activity of chromia, assuming saturation with MnO. Insertion of this value in equation 7 allowed calculation of the CrO_3 partial pressure in equilibrium with $MnCr_2O_4$ in air. These values are plotted in Figure 27 along with those for unit activity of chromia and those for $LaCrO_3$. (The latter were calculated by inserting the activity data for chromia in $LaCrO_3$ from reference 10 and presumably refer to La_2O_3-saturation.) Figure 27 indicates that the CrO_3 partial pressure and, therefore, evaporation rate from a chromia forming alloy could be reduced by two orders of magnitude if a layer of MnO-saturated $MnCr_2O_4$ could be made to reliably form on the surface. A dense, artificially applied coating of $LaCrO_3$ could, in principle, achieve another order of magnitude reduction.

It should be noted that the low values of CrO_3 partial pressure indicated to be in equilibrium with $MnCr_2O_4$ and $LaCrO_3$ in Figure 27 were calculated assuming MnO and La_2O_3 saturation, respectively. If layers of these compounds are present over a chromia film and begin to equilibrate with the underlying chromia the activity of chromia will increase and this will result in an increase in the CrO_3 partial pressure. In the limit of the layers becoming Cr_2O_3 saturated the chromia activity will be unity and the CrO_3 partial pressure will be given by the line for Cr_2O_3 in Figure 27. The rate and extent of such equilibration will be determined by transport in the outer layer as well as loss of CrO_3 to the gas phase.

All of the above comments will also pertain to the reduction of the partial pressure of $CrO_2(OH)_2$ over chromia-containing spinels in atmospheres containing water vapor.

Formation of Oxide-free Zone Below the Chromia Scale

A number of the cross-section micrographs presented above indicate oxide-free metallic regions between the external chromia scale and a zone of internal oxidation. In the case of Crofer these regions were in the form of metallic globules protruding into the chromia scale, Figures 9, 10, 15, 16 and 22. In the case of AL 453 a continuous, or nearly continuous, region formed below the chromia scale, Figures 12, 13, and 23.

These regions have formed by plastic flow of metal from the zone of internal oxidation because of stresses produced by the volume increase associated with the internal oxide particles. This phenomenon was apparently first reported by Darken[30] for the internal oxidation of Ag-base alloys. It was studied in detail by Guruswamy et al[31] who observed oxide-free Ag nodules on the surface of Ag-In alloys after internal oxidation in air at temperatures in the range 500-700˚C. It was proposed that dislocation pipe-diffusion controlled creep was the mode of stress relief and Ag transport. Similar observations have been made for the internal oxidation of Ni-Al[32] and Ni-Al-Si[33, 34] alloys. The amount of metal transported has been observed to be proportional to the volume of internal oxides produced. This is qualitatively the result of the current investigation in that there is a much larger oxide-free region for AL453 than Crofer which is consistent with a larger internal oxide volume for AL453. Such a region has apparently formed locally above a single large internal oxide particle in 26 Cr Ferritic in Figure 21a. The previous observations of this phenomenon have generally been for the case of internal oxidation with no external scale formation. Guan et al[35] studied the internal oxidation of Ni-Al-Si alloys under a NiO scale but did not report an oxide-free region for an oxidation temperature which had produced an oxide-free layer of Ni on the surface in the absence of an external scale. Huczkowski et al[23] show several examples of metallic protrusions under chromia scales and comment that they can accelerate the oxidation rate.

Sigma-Phase Formation

Figure 21 shows that a second phase formed in the Fe-26 Cr ferritic alloy during exposure at 700˚C. Figure 28 shows the XRD pattern for a Fe-26 Cr ferritic specimen exposed for 2000 hours at 700^oC in air + 0.1 atm H_2O. Many of the peaks match with the chromia lines, the ferrite lines, or the sigma phase lines. This analysis proved that the sample did in fact contain the sigma phase.

The approximate compositions of the sigma phase and the ferrite were determined by EDS analysis. The results show significant increases in the amount of chromium (~35 wt%) and molybdenum (3-4 wt%) in the sigma phase regions when compared to the initial composition. The surrounding ferrite is slightly depleted of those elements. The silicon content appears to not be greatly affected, with only a slight enrichment in the sigma phase.

Figure 29 shows E-brite that had been exposed in dry air at 700^oC in 50 hour increments to 500 hours. Only a small amount of the sigma phase is seen after 200 hours, but with time, more is seen in each successive micrograph. The sigma-phase nucleates at intersections of ferrite grain boundaries with the free surface and propagates inward.

The micrographs of Fe-26 Cr ferritic exposed in dry air at 700^oC in 50 hour increments up to 500 hours are shown in Figure 30. Again, there is only a small amount of sigma phase observed in the sample exposed for 200 hours. As the exposure time is increases, the amount of sigma phase also increases.

The sigma phase was observed only in E-brite and Fe-26Cr ferritic that had been exposed at 700^oC in the three atmospheres that were studied. This can be explained if the Fe-Cr phase diagram is examined (see Figure 31). E-brite and Fe-26Cr ferritic both contain 26% chromium,

which is more than the other alloys that were investigated. In Figure 31, point A (700°C, 26% chromium) is within the region where sigma forms, but point B (900°C, 26% chromium) is outside of this region. However, sigma phase formation is also strongly influenced by other elements in the alloy.

E-brite contains 1.0% molybdenum and 0.2% silicon. The Fe-26 Cr ferritic also contains 1.0% molybdenum, but has approximately 1.0% silicon. Additions of molybdenum and silicon will increase the rate of sigma phase formation[36]. However, Fe-26 Cr ferritic contains considerably more silicon than E-brite. It has been reported that Si is extremely potent in accelerating sigma-phase formation[37, 38]. This was indeed observed in that the formation of sigma-phase was more extensive in Fe-26Cr ferritic than E-brite. Tetsui et al[38] have reported that a high purity Fe-30Cr alloy did not form sigma phase after 500 hours at 650°C. Therefore, alloy purity may be an important avenue of study for production of high-Cr interconnects which are resistant to sigma-phase formation.

The development of the sigma phase was observed to be strongly influenced by the environment in which the specimens were exposed. Figure 32 shows a cross-section of Fe-26Cr ferritic which was exposed in dry air for 2000 cycles. The sigma phase, which nucleated at the surface, has penetrated a distance of approximately 50 μm into the alloy. Figure 33 show a cross-section of the same alloy which was exposed in simulated anode gas for 2000 cycles. Sigma phase was observed to form all the way to the center of the 1 mm thick specimen. Similarly, Figure 34 shows the cross-section of a specimen exposed for 2000 cycles in air plus 10% water vapor. The sigma phase has formed all the way to the center of the specimen and the volume fraction of sigma phase appears to be even larger than that in Figure 33. Figures 33 and 34 suggest that the presence of water vapor is influencing the nucleation and/or growth of the

sigma phase. This somewhat remarkable result of a metallic phase transformation being influenced by an external atmosphere is the subject of continuing experiments.

SUMMARY AND CONCLUSIONS

The cyclic oxidation of a variety of ferritic stainless steels has been studied in the temperature range 700-900˚C in atmospheres relevant to solid oxide fuel cell operation. The most detrimental environment at 800˚C and 900˚C was found to be air with 10% water vapor. This resulted in excessive oxide spallation from Fe-26Cr ferritic and E-brite and rapid scale growth on Crofer22 APU and AL 453. The oxidation behavior of the alloys varied considerably based on the Cr concentration and the presence of other minor elements, whether added intentionally (e.g. reactive elements) or remaining as impurities (e.g.Si, Al).

Oxide growth was slow at 700˚C but the higher Cr-content alloys were observed to form sigma-phase at this temperature. The sigma phase formation was accelerated by higher silicon contents and, remarkably, by the presence of water vapor in the exposure environment.

Alloys containing Mn were observed to form an outer layer of $MnCr_2O_4$ over the chromia scale. The potential for this overlayer to suppress reactive evaporation of the chromia scales has been analyzed.

REFERENCES

1. Z. G. Yang, J. W. Stevenson, and P. Singh, Adv. Mater. Proc., 161 (6), 34 (2003).

2. W. Z. Zhu and S. C. Deevi, Mater. Sci. Eng., A348, 227 (2003)

3. Z. G. Yang, K. S. Weil, D. M. Paxton, and J. W. Stevenson, J. Electrochem. Soc., 150, A1188 (2003).

4. W. J. Quadakkers, J. Piron-Abellan, V. Shemet and L. Singheiser, Materials At High Temperatures, 20, 115 (2003).

5. D. M. England and A. V. Virkar, J. Electrochem. Soc., 146, 3196 (1999).

6. W. J. Quadakkers, H. Greiner, and W. Köck, "Metals and Alloys for High Temperature SOFC Application", Proc. First European Solid Oxide Fuel Cell Forum, U. Bossel, ed. 1994, p.525.

7. C. S. Tedmon, J. Electrochem. Soc., 113, 766 (1966).

8. N. Birks and G. H. Meier, Introduction to High Temperature Oxidation of Metals, Edward Arnold, London, l983.

9. W. J. Quadakkers, H. Greiner, W. Köck, H. P Buchkremer, K. Hilpert, and D. Stöver, "The Chromium Base Metallic Bipolar plate – Fabrication, Corrosion and Cr Evaporation", Proc. Second European Solid Oxide Fuel Cell Forum, B. Thorstensen, ed. 1996, p.297.

10. K. Hilpert, D. Das, M. Miller, D. H. Peck, and R. Weiss, J. Electrochem. Soc., 143, 3642 (1996).

11. K. Huang, P. Y. Hou, and J. B. Goodenough, Solid State Ionics, 129, 237 (2000).

12. T. Brylewski, M. Nanko, T. Maruyama, and K. Przybylski, Solid State Ionics, 143, 131 (2001).

13. W. J. Quadakkers, T. Malkow, J. Pirón-Abellán, U. Flesch, V. Shemet, and L. Singheiser, "Suitability of Ferritic Steels for Application as Construction Materials for SOFC Interconnects", Proc. Fourth European Solid Oxide Fuel Cell Forum, A. J. McEvoy, ed. 2000, p.827.

14. J. Pirón-Abellán, V. Shemet, F. Tietz, L. Singheiser, W. J. Quadakkers, and A. Gil, "Ferritic Steel Interconnect for Reduced Temperature SOFC", Proc. Solid Oxide Fuel Cells VII, H. Yokokawa and S. C. Singhal, eds., The Electrochem. Soc., 2001, p. 811.

15. Z. G. Yang, J. S. Hardy, M. S. Walker, G. Xia, S. P. Simner, and J. W. Stevenson, J. Electrochem. Soc., 151, A1825 (2004).

16. D. M. England and A. V. Virkar, J. Electrochem. Soc., 148, A330 (2001).

17. A.Gil, H. J. Penkalla, M. Hänsel, J. Norton, W. Köck, and W. J. Quadakkers, "The Oxidation Behaviour of Cr Based ODS Alloys in H_2/H_2O at 1000°C", IX Conf. On Electron Microscopy of Solids, 1996, p. 441.

18. W. J. Quadakkers, J. F. Norton, J. Penkalla, U. Breuer, A. Gil, T. Rieck, and M. Hänsel, "SNMS and TEM Studies on the Oxidation Behaviour of Cr-Based ODS Alloys", Microscopy of Oxidation 3, S. B. Newcomb and J. A. Little, eds., Inst. of Materials, 1996, p.221.

19. W. J. Quadakkers, J. F. Norton, S. Canetoli, K. Schuster, and A. Gil, "Hot Stage Microscopy of the Nucleation and Growth of Oxide Scales on Cr and Cr-Based Alloys", Microscopy of Oxidation 3, S. B. Newcomb and J. A. Little, eds., Inst. of Materials, 1996, p. 609.

20. R. Janakiraman, G. H. Meier, and F. S. Pettit, Metall. and Mater. Trans. A, 30A, 2905 (1999).

21. M. C. Maris-Sida, G. H. Meier, and F. S. Pettit, Metall. and Mater. Trans. A, 34A, 2609 (2003).

22. Z. G. Yang, M.S. Walker, P. Singh and J. W. Stevenson, Electrochem. And Solid State Letters, 6, B35 (2003).

23. P. Huczkowski, N. Christiansen, V. Shemet, J. Piron-Abellan, L. Singheiser, and W. J. Quadakkers, J. Fuel Cell Sci. and Tech. (Trans. ASME), 1, 31 (2004).

24. C. Gindorf, L. Singheiser, and K. Hilpert, Steel Research, 72, 528 (2001).

25. J. E. Antill, K. A. Peakall, and J. B. Warburton, Corros. Sci., 8, 689 (1968).

26. M. G. C. Cox, B. McEnaney, and V. D. Scott, Phil. Mag., 26 , 839 (1972).

27. J. D. Tretjakow and H. Schmalzried, Berichte der Bunsengesellschaft, 69, 396 (1965).

28. I. Barin, Thermochemical Data of Pure Substances, VCH Verlagsgesellschaft, Weinheim, 1993.

29. T. Jacob and G. N. K. Iyengar, J. Amer. Ceram. Soc., 69, 487 (1986).

30. L.S. Darken, Trans. Amer. Soc. Metals, 54, 600 (1961).

31. S. Guruswamy, S. M. Park, J. P. Hirth, and R. A. Rapp, Oxid. Metals, 26, 77 (1986).

32. F. H. Stott and G. C. Wood, Mater. Sci. and Tech., 4, 1072 (1988).

33. H. C. Yi, S. W. Guan, W. W. Smeltzer, and A. Petric, Acta Metall. Mater., 42, 981 (1994).

34. S. W. Guan, H. C. Yi, and W. W. Smeltzer, Oxid. Metals, 41, 377 (1994).

35. S. W. Guan, H. C. Yi, and W. W. Smeltzer, Oxid. Metals, 41, 389 (1994).

36. G. F. Vander Voort, "Embrittlement of Steels." *ASM Handbook, Volume 1, Properties and Selection: Irons, Steels, and High-Performance Alloys, Tenth Edition*, ASM International, Materials Park, Ohio, 1990, p. 689 – 736.

37. I. Yano and K. Abiko, Phys. Stat. Sol., 160, 449 (1997).

38. T. Tetsui, M. Shinohara, and K. Abiko, Phys. Stat. Sol., 160, 459 (1997).

LIST OF FIGURES

Table 1   Approximate Electrical Resistivities of Oxides in Air at 800°C.

Oxide	Resistivity (Ω^*cm^2)
SiO_2	10^6
Al_2O_3	10^8
Cr_2O_3	10^2

Table 2: Comparison of oxide thicknesses and weight gains per area for three ferritic alloys exposed at $900^{\circ}C$ in $Ar/H_2/H_2O$, air, and air + 10% H_2O

Alloy	Atmosphere	Time (hr)	Average Oxide Thickness (μm)	Calculated Δm/A (mg/cm²)	Measured Δm/A (mg/cm²)
Crofer	Dry Air	2000	8	1.3201	2.1916
Crofer	Air + 0.1 atm H_2O	2000	13.5	2.2276	1.9964
Crofer	$Ar/H_2/H_2O$	2005	20	3.3001	11.2230
AL 453	Dry Air	2000	8.75	1.4444	2.5033
AL 453	Air + 0.1 atm H_2O	2000	7.5	1.2375	1.0790
AL 453	$Ar/H_2/H_2O$	2005	11.5	1.8976	0.7079
Fe-26Cr	Dry Air	2000	4.5	0.7425	3.4825
Fe-26Cr	Air + 0.1 atm H_2O	2000	6	0.9900	3.0840
Fe-26Cr	$Ar/H_2/H_2O$	2005	8.5	1.4025	6.1166
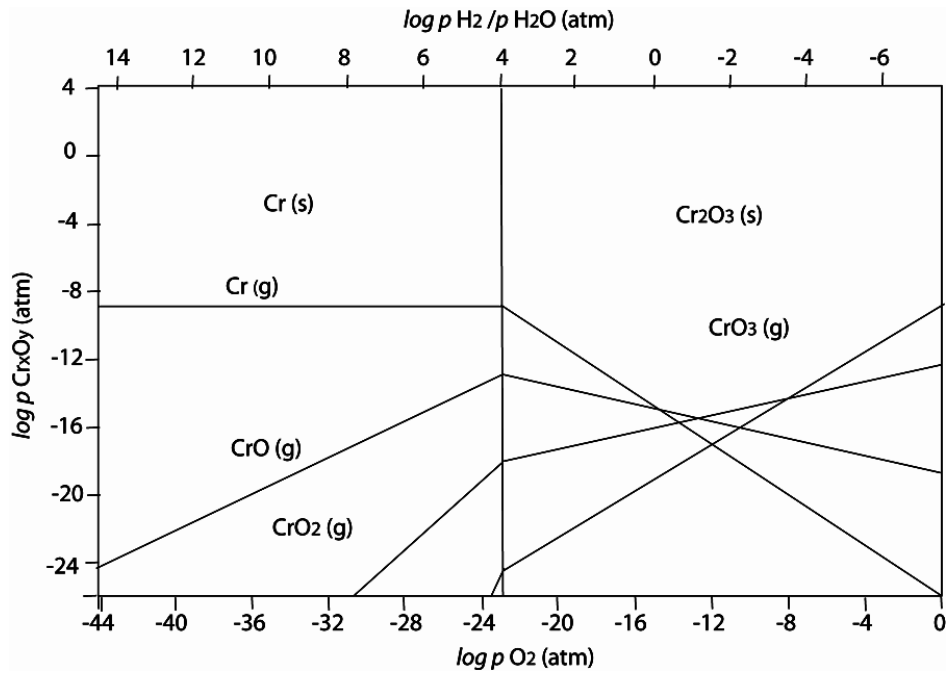
Figure 1.   Vapor species diagram for the Cr-O system at 1250 K from Ref. 7.
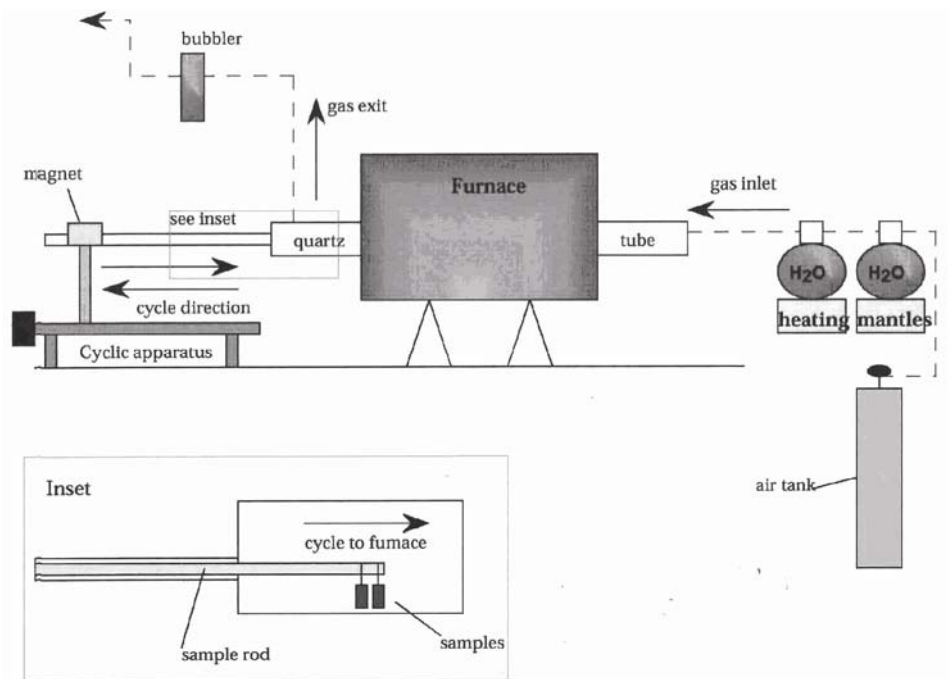
Figure 2   Schematic diagram of the apparatus used for cyclic oxidation exposures with controlled partial pressures of water vapor.
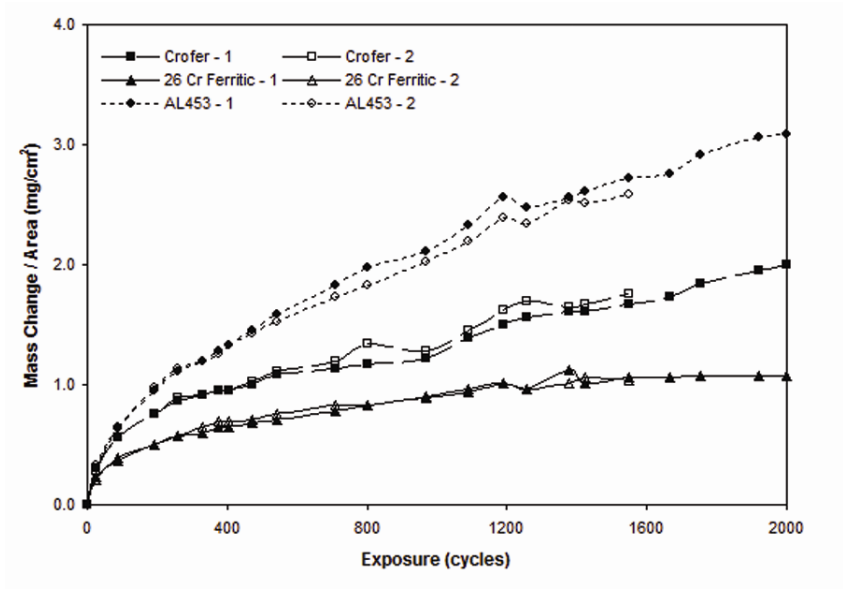
Figure 3. Weight Change Vs Time Plots for duplicate specimens for ferritic alloys exposed in dry air (simulated cathode gas) at 900°C using one – hour cycles.
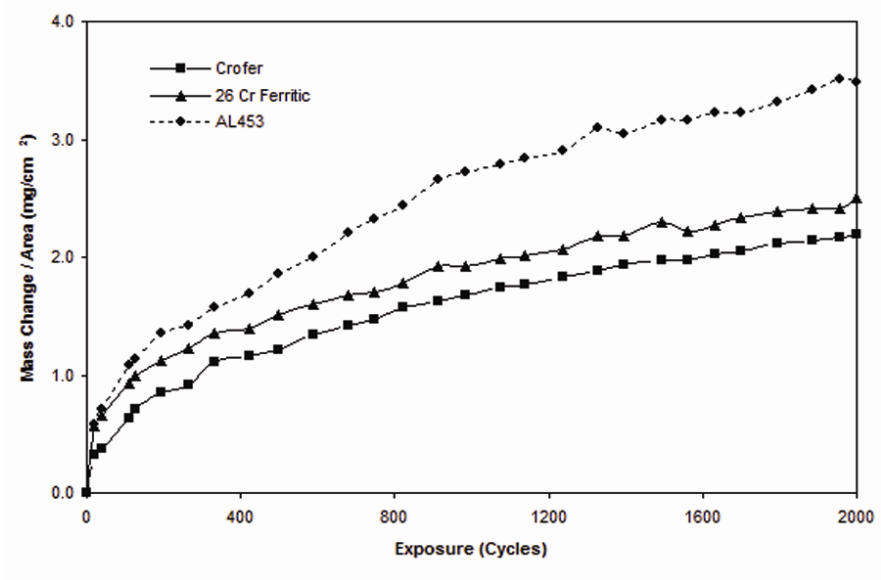
Figure 4. Weight Change Vs Time plots for duplicate specimens of ferritic alloys exposed in

Ar/H_2/H_2O (simulated anode gas) at 900^oC using one – hour cycles.
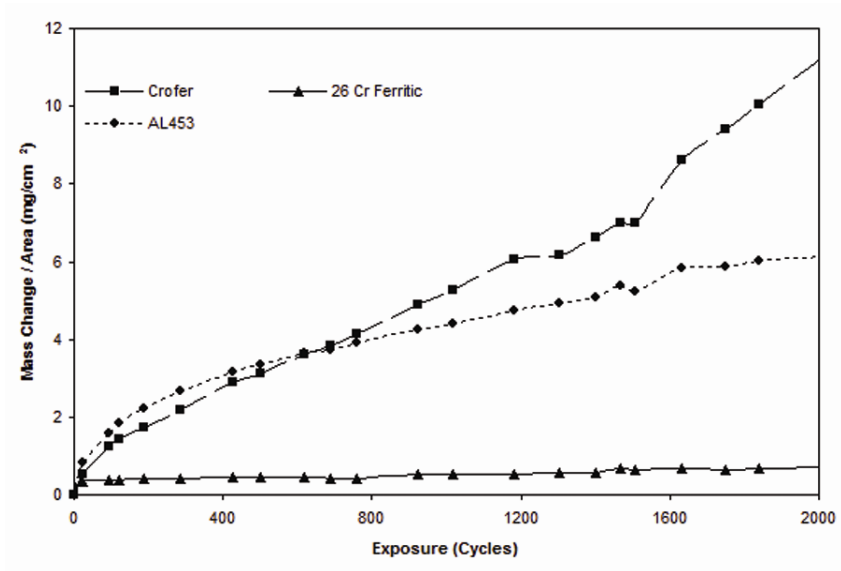
Figure 5. Weight Change Vs Time plots for duplicate specimens of ferritic alloys exposed in air + 10% H_2O (simulated moistened cathode gas) at 900°C using one – hour cycles.
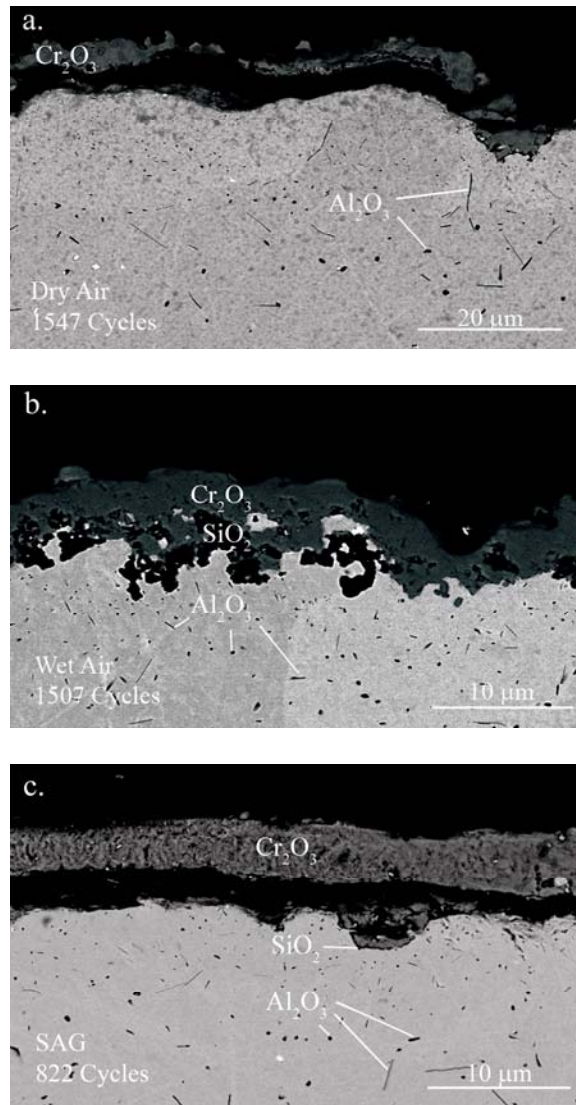
Figure 6. Cross – section micrographs of Fe-26%Cr ferritic after exposure in dry air (a.), air + 10% H_2O (b.), and $Ar/H_2/H_2O$ (c.) atmospheres at 900°C.
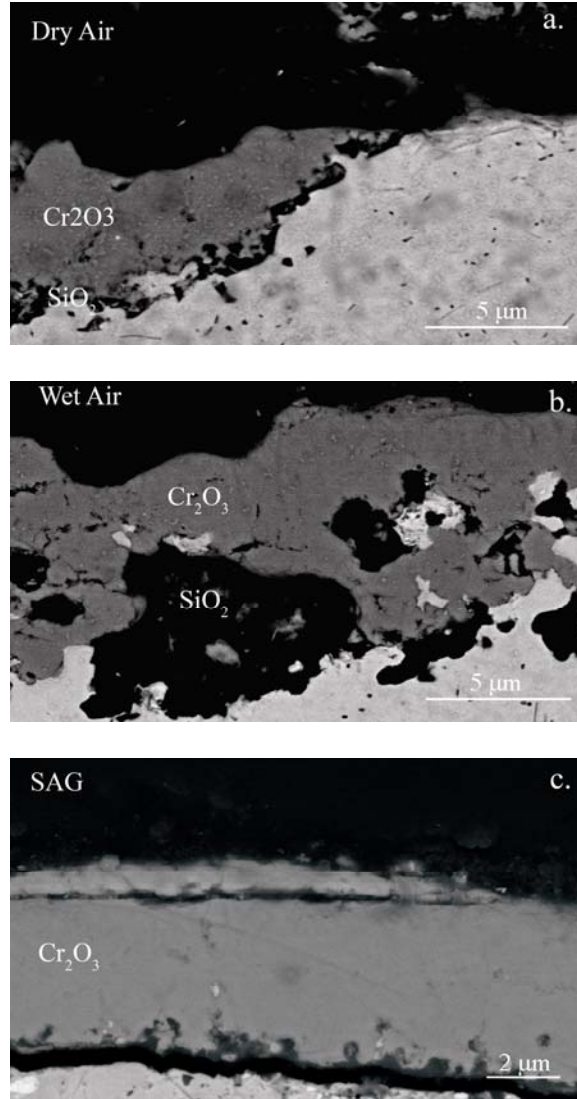
Figure 7. Cross – section micrographs of Fe-26%Cr ferritic after exposure in dry air (a.), air + 10% H_2O (b.), and Ar/H_2/H_2O (c.) atmospheres at 900°C showing details of the alloy/scale interface.
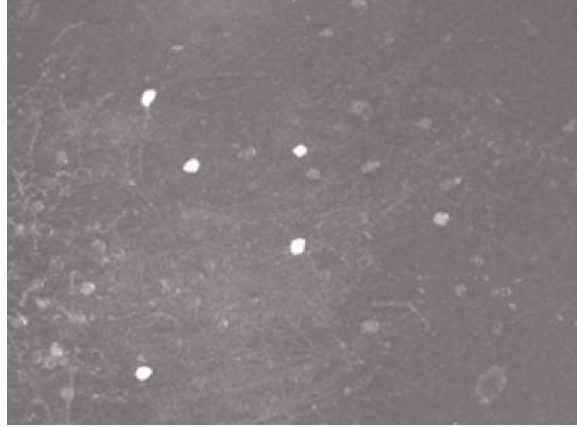
Figure 8.   Macroscopic photograph showing freshly spalled and re-grown areas on the surface of Fe-26Cr ferritic (847 cycles, 1/10atm H_2O)
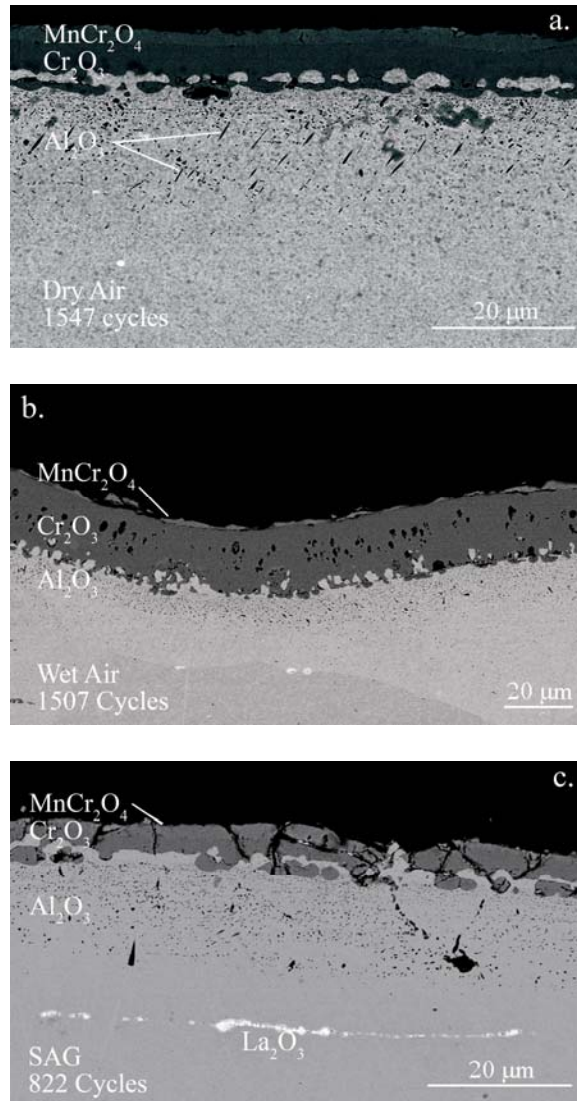
Figure 9. Cross – section micrographs of Crofer after exposure in dry air (a.), air + 10% H_2O (b.), and $Ar/H_2/H_2O$ (c.) atmospheres at 900°C
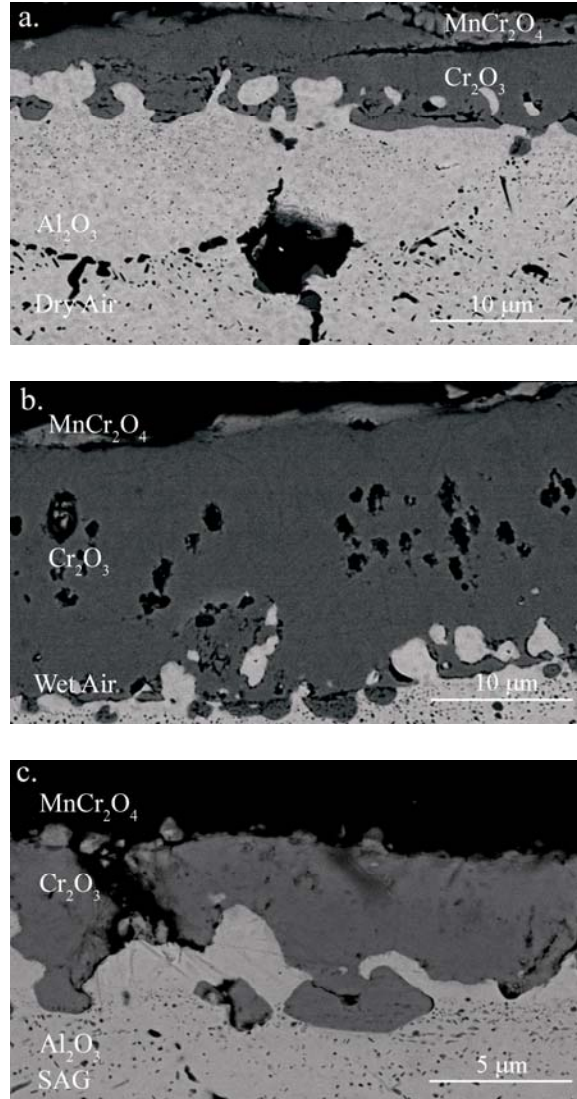
Figure 10. Cross–section micrographs of Crofer after exposure in dry air (a.), air + 10% H_2O (b.), and $Ar/H_2/H_2O$ (c.) atmospheres at 900°C, showing more detail of the scales.
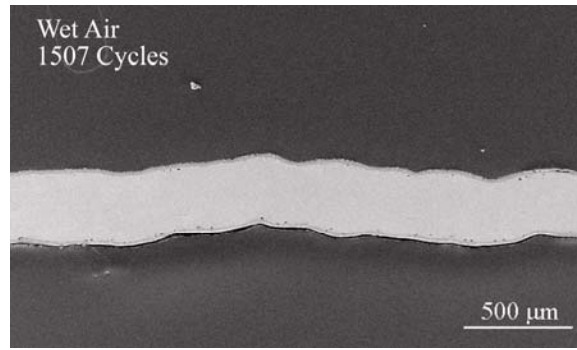
Figure 11.   Macroscopic photograph of a Crofer specimen exposed in air +10% H_2O showing extensive warpage.
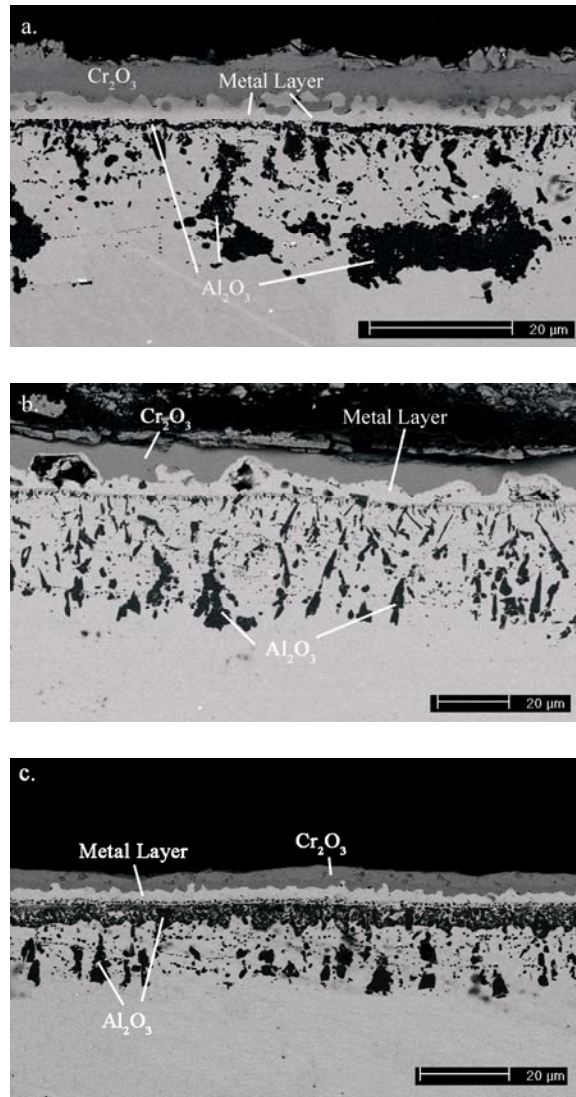
Figure 12 Cross-section micrographs of AL453 after exposure in dry air (a.), air + 10% H_2O (b.), and $Ar/H_2/H_2O$ (c.) atmospheres at 900°C.
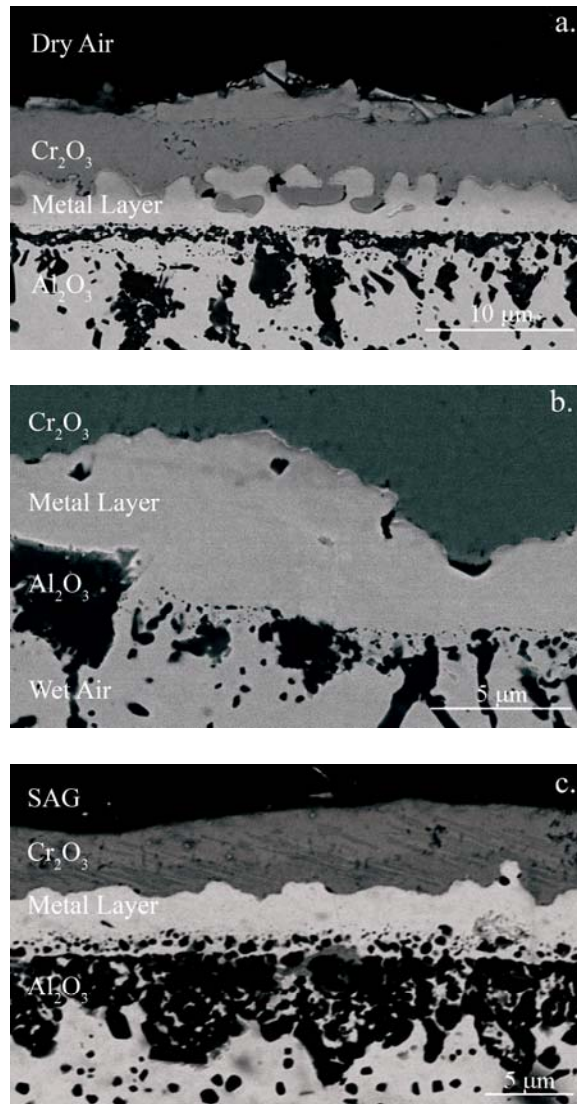
Figure 13. Cross-section micrographs of AL453 after exposure in dry air (a.), air + 10% H_2O (b.), and $Ar/H_2/H_2O$ (c.) atmospheres at 900°C, showing more detail of the scales.
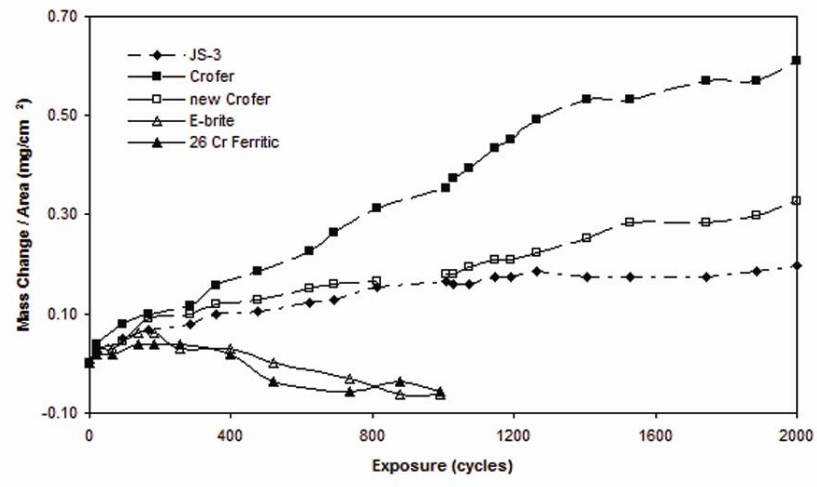
Figure 14. Weight Change Vs Time plots for duplicate specimens of ferritic alloys exposed in air + 10% H_2O (simulated moist cathode gas) at 800°C using one – hour cycles.
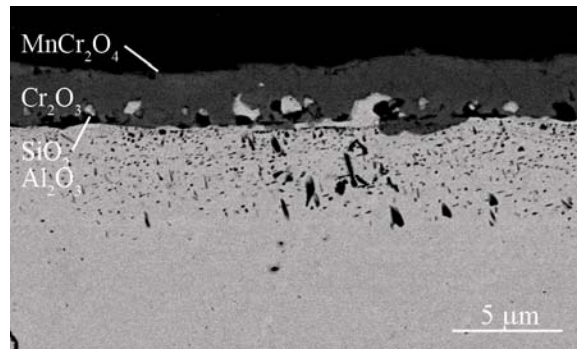
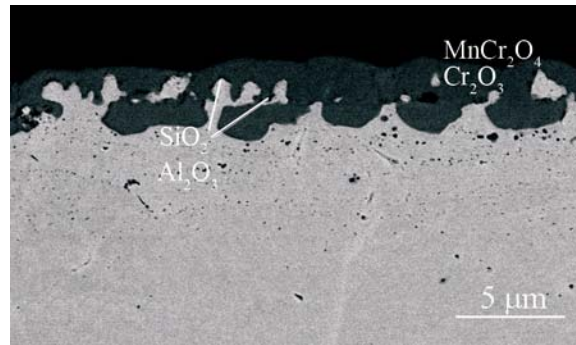Figure 15.   Cross-section micrograph of Crofer after exposure in air + 0.1 atm H_2O for 2000 hours at 800˚C.

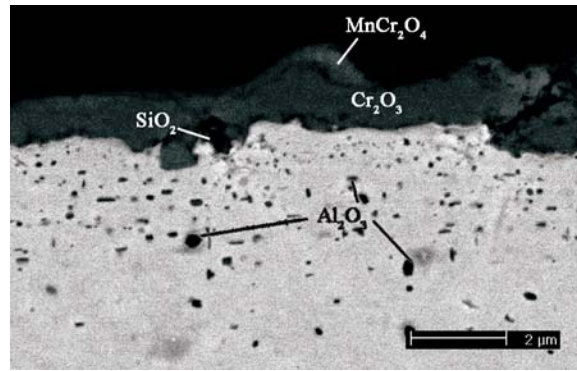Figure 16.   Cross-section micrograph of "New Crofer" after exposure in air + 0.1 atm H_2O for 2000 hours at 800°C.

Figure 17.   Cross-section micrograph of JS-3 after exposure in air + 0.1 atm H_2O for 2000 hours at 800˚C.

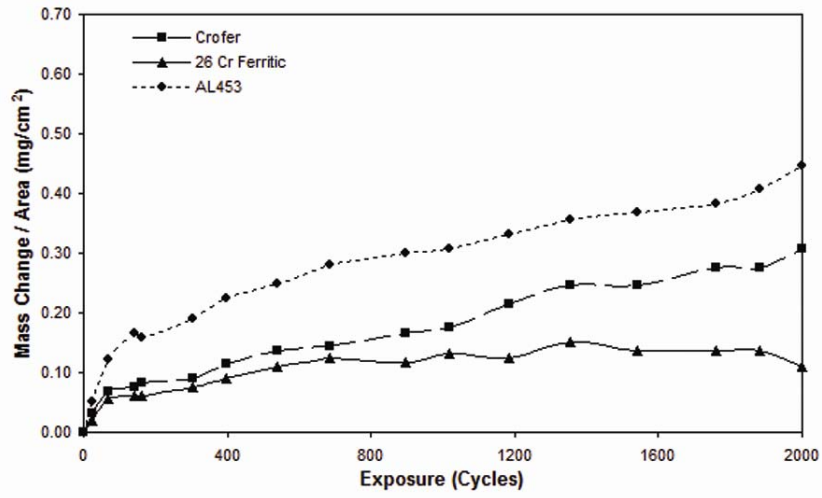Figure 18. Weight Change Vs. Time plots for duplicate specimens of ferritic alloys exposed in dry air (simulated cathode gas) at 700°C using one – hour cycles.
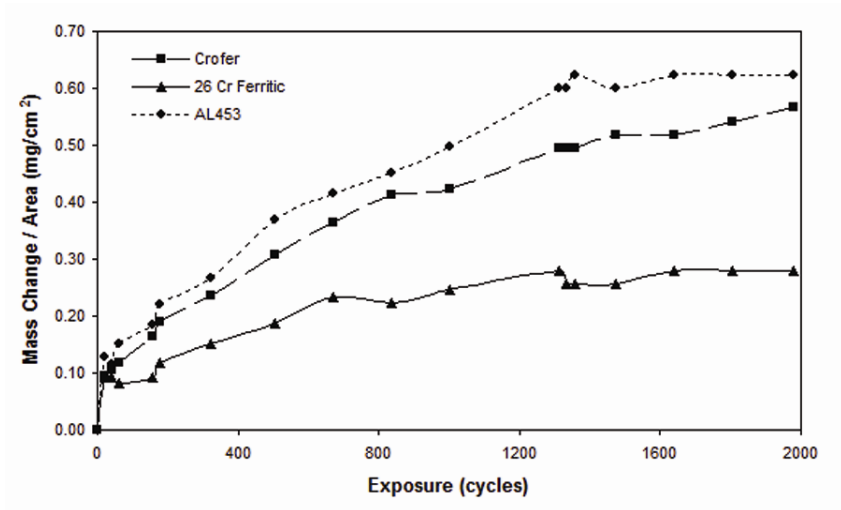
Figure 19. Weight Change Vs Time plots for duplicate specimens of three ferritic alloys exposed in Ar/H$_2$/H$_2$O (simulated anode gas) at 700°C using one – hour cycles.
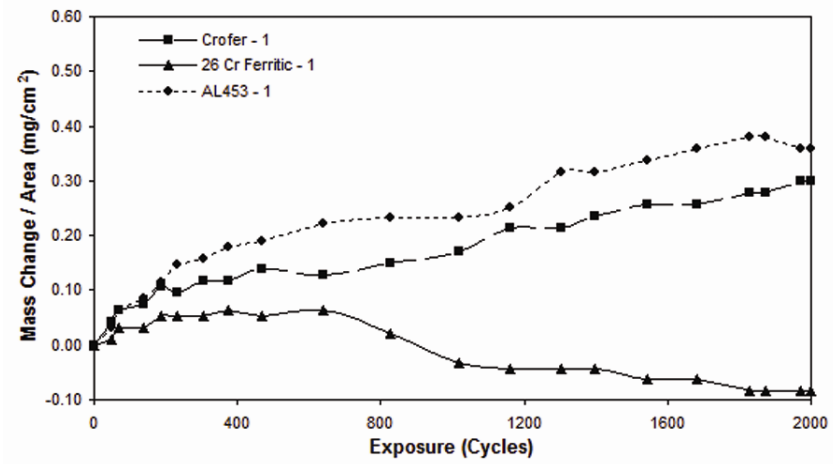
Figure 20. Weight Change Vs Time plots for duplicate specimens of ferritic alloys exposed in air + 10% H_2O (simulated moist cathode gas) at $700^{\circ}C$ using one hour cycles
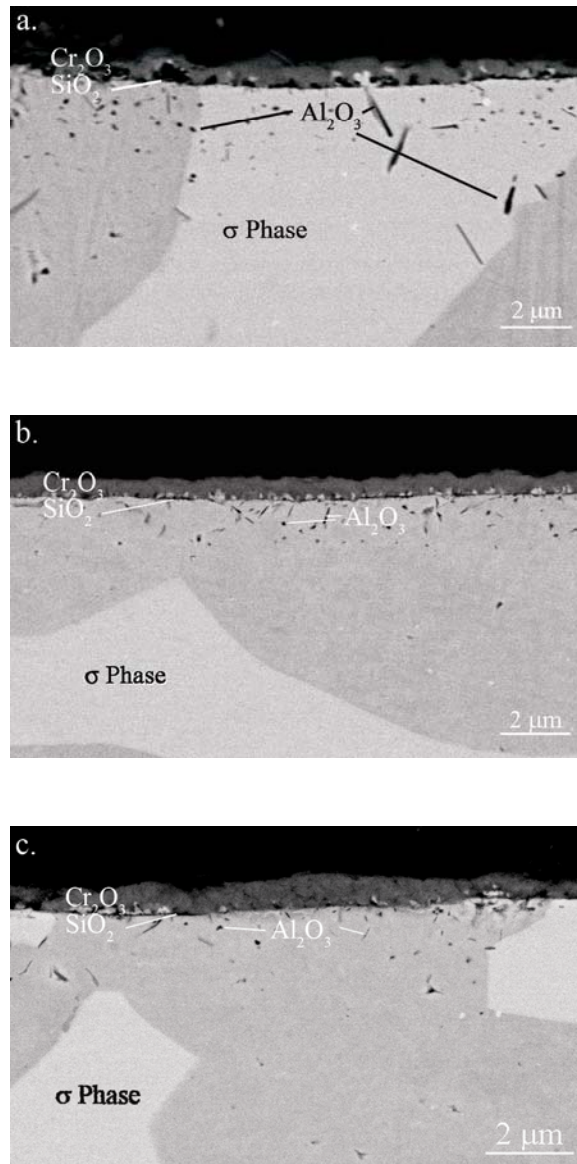
Figure 21. Cross – section micrographs of Fe – 26% Cr ferritic alloy after exposure in atmospheres of dry air (a.), Ar/H_2/H_2O (b.), and air + 10% H_2O (c.) for 2000 one hour cycles at 700°C.
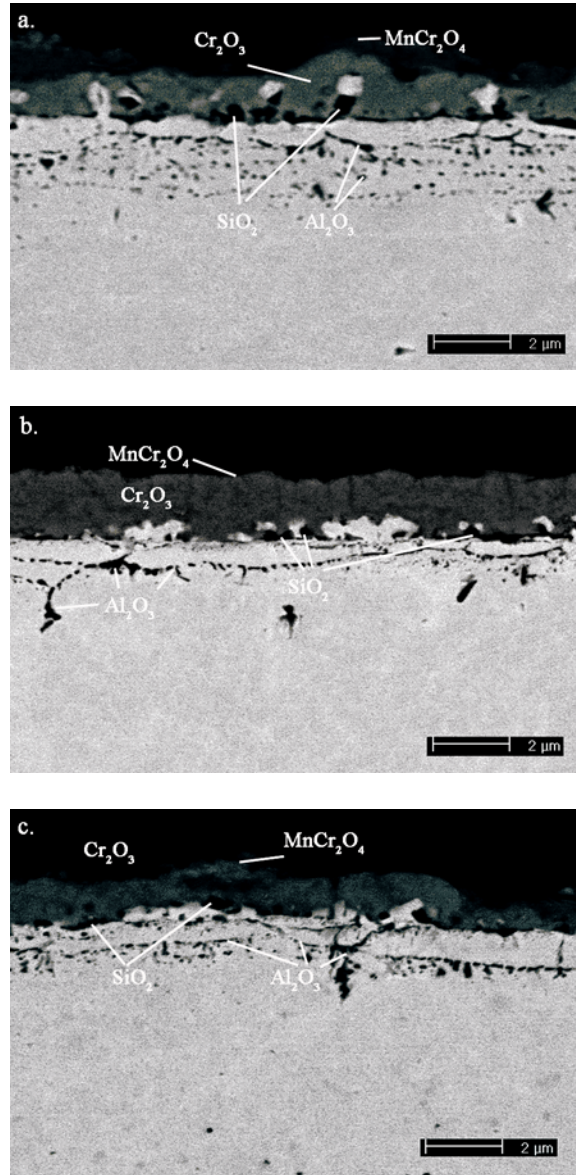
Figure 22.   Cross – section micrographs of Crofer 22APU after exposure in atmospheres of dry air (a.), $Ar/H_2/H_2O$ (b.), and air + 10% H_2O (c.) for 2000 one hour cycles at 700^oC.
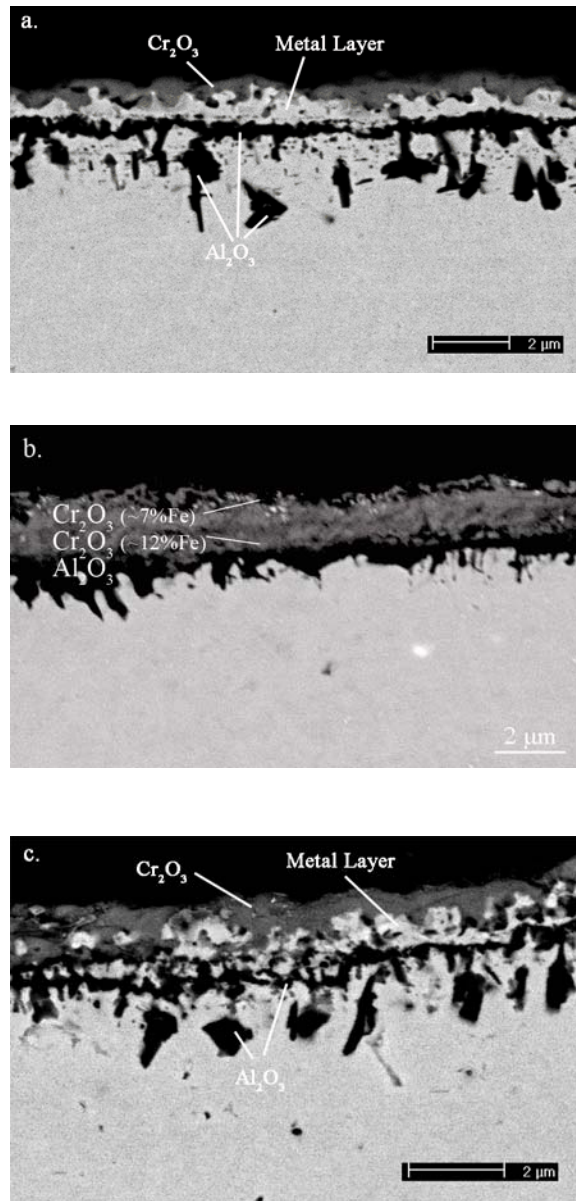
Figure 23.   Cross – section micrographs of AL 453 after exposure in atmospheres of dry air (a.), $Ar/H_2/H_2O$ (b.), and air + 10% H_2O (c.) for 2000 one hour cycles at 700^oC.
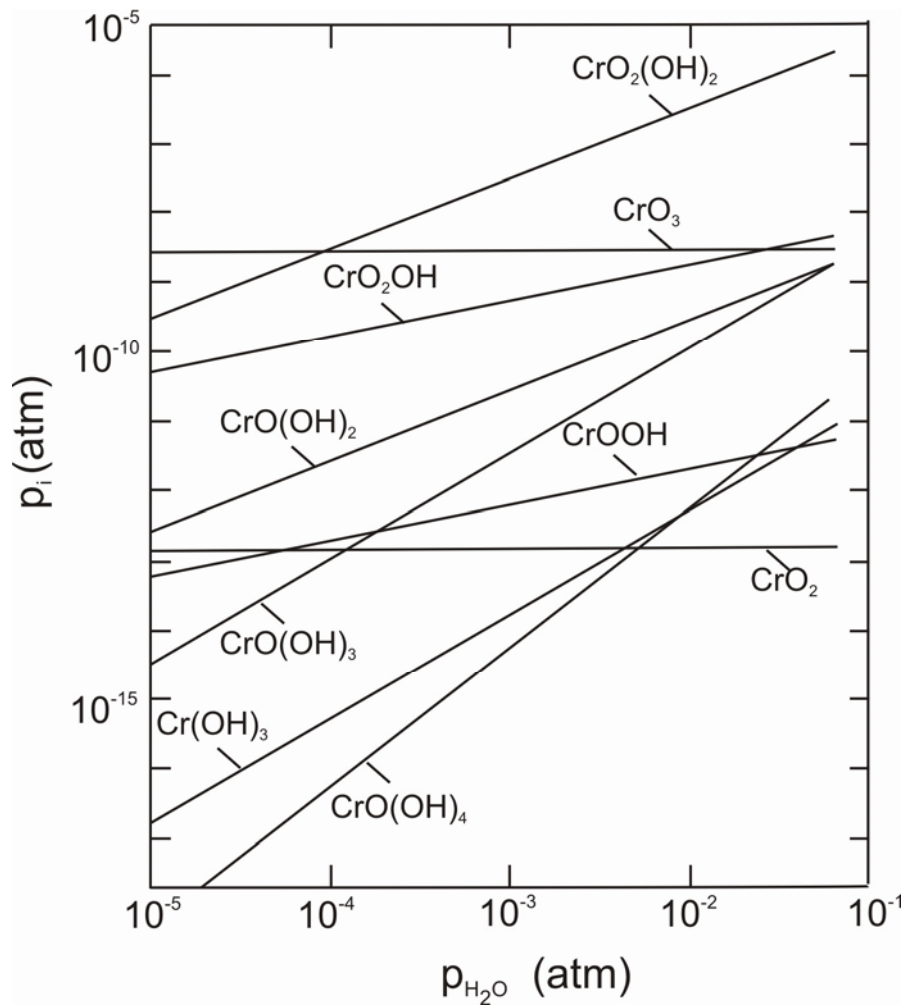
Figure 24   Plot showing the effect of water vapor on the volatility of Cr_2O_3 at 950°C after Ref. [10].
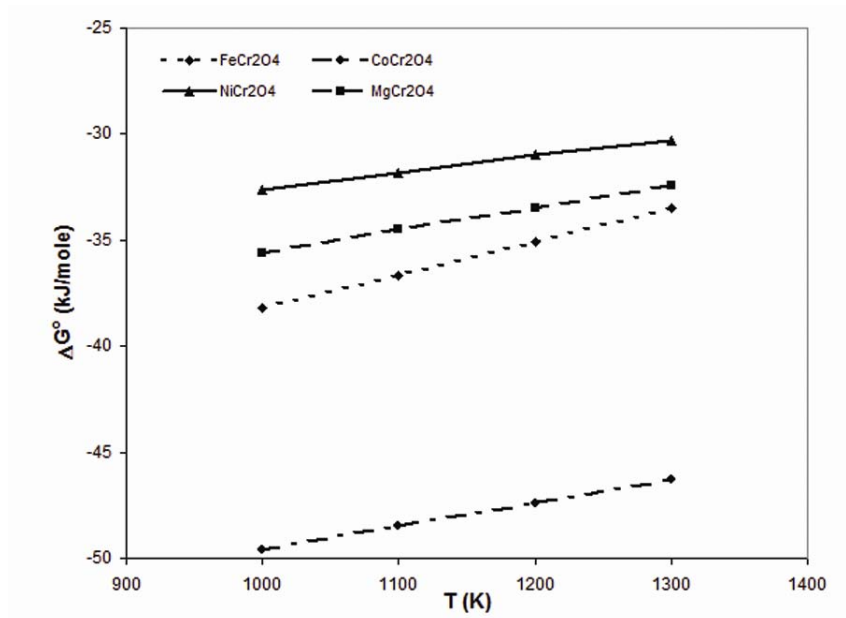
Figure 25   Standard free energy as a function of temperature changes for the reaction of transition metal oxides with chromia to form spinel.
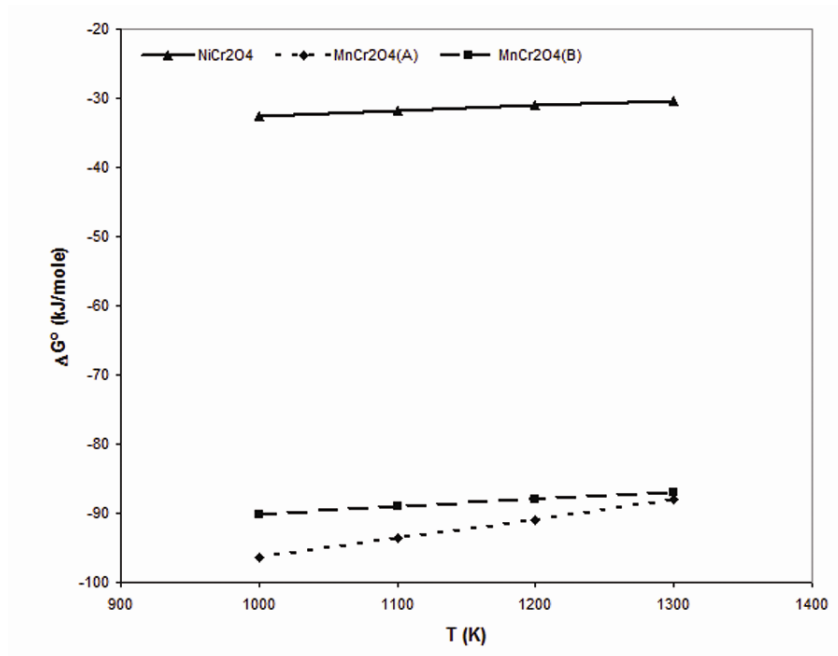
Figure 26   Standard free energy changes for the reactions of NiO and MnO with chromia to form the respective chromates. (The two lines for $MnCr_2O_4$ were obtained by using two different techniques for estimating $\Delta S°$.)
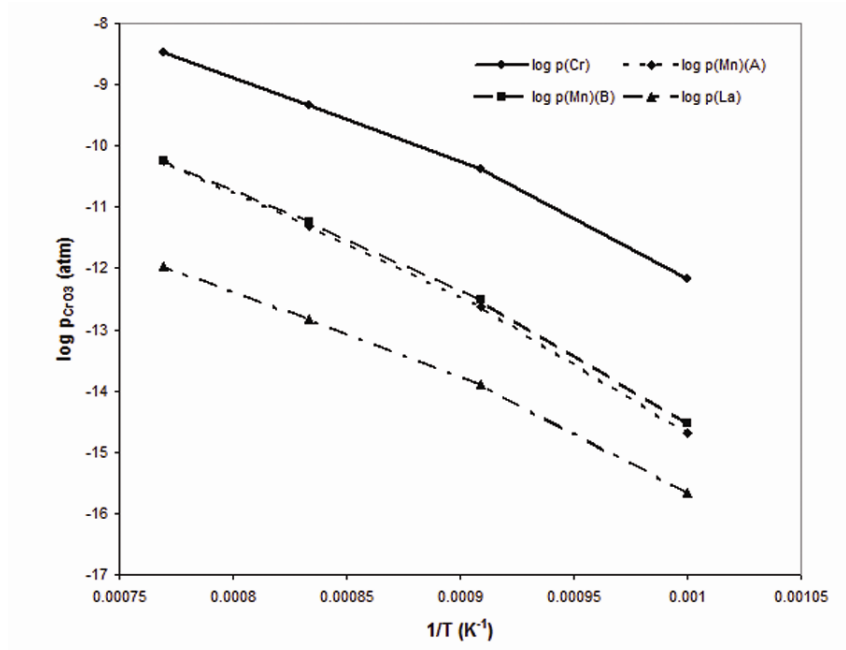
Figure 27   Partial pressures of CrO$_3$ in equilibrium with Cr$_2$O$_3$, La$_2$O$_3$-saturated LaCrO$_3$, and MnO-saturated MnCr$_2$O$_4$ as a function of temperature.
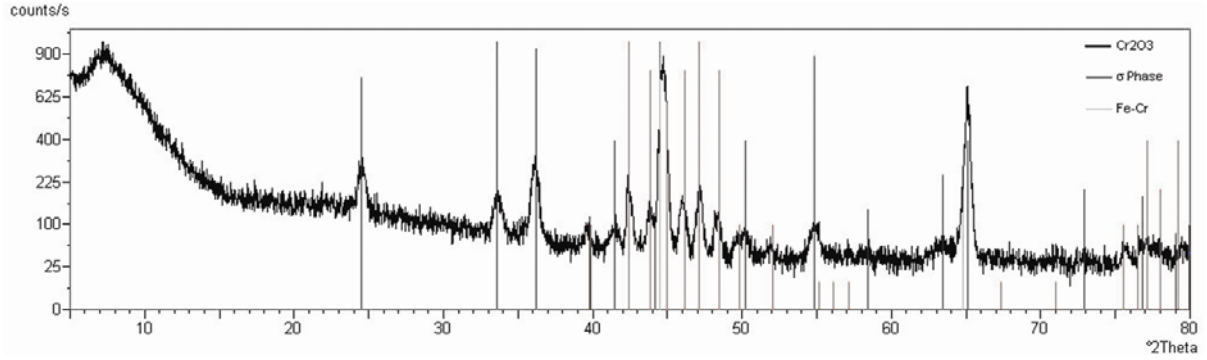
Figure 28.   X-ray diffraction pattern for 26 Cr Ferritic alloy exposed at 700˚C in air + 0.1 atm H_2O for 2000 hours.
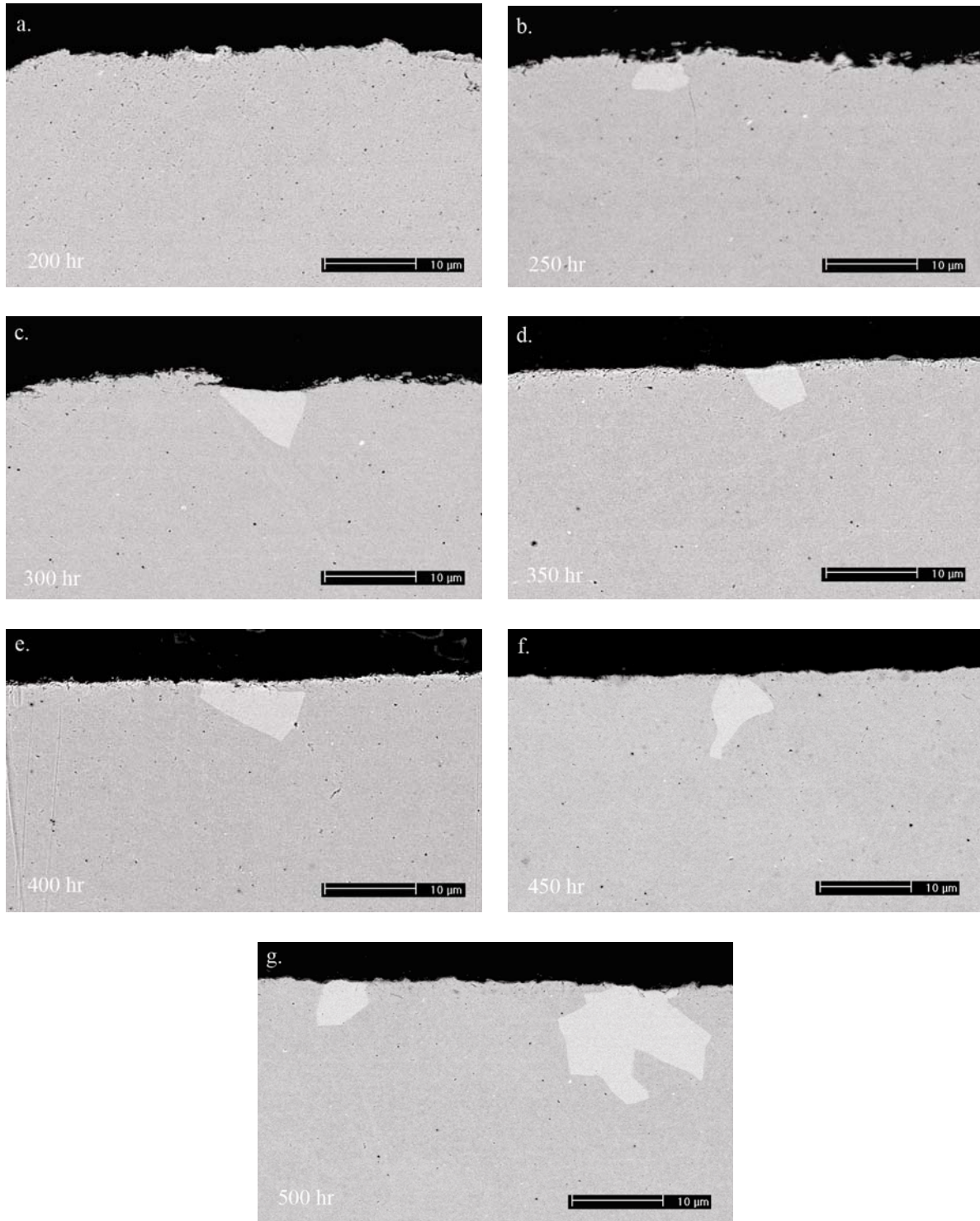
Figure 29.   Cross-sections of E-brite exposed at 700˚C in dry air in 50 hour increments after a) 200 hours, b) 250 hours, c) 300 hours, d) 350 hours, e) 400 hours, f) 450 hours, and g) 500 hours.
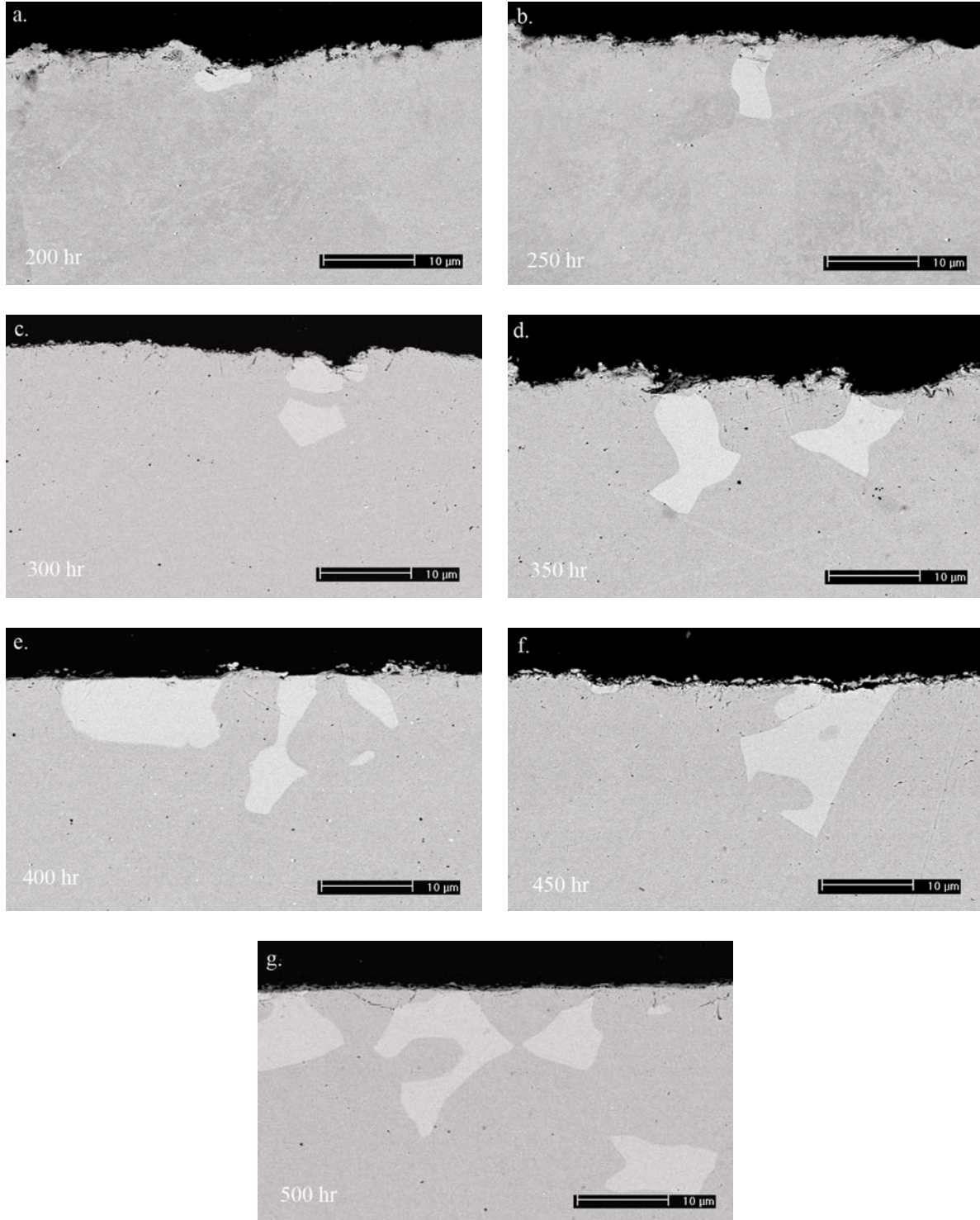
Figure 30.   Cross-sections of 26 Cr Ferritic exposed at 700˚C in dry air in 50 hour increments after a) 200 hours, b) 250 hours, c) 300 hours, d) 350 hours, e) 400 hours, f) 450 hours, and g) 500 hours.
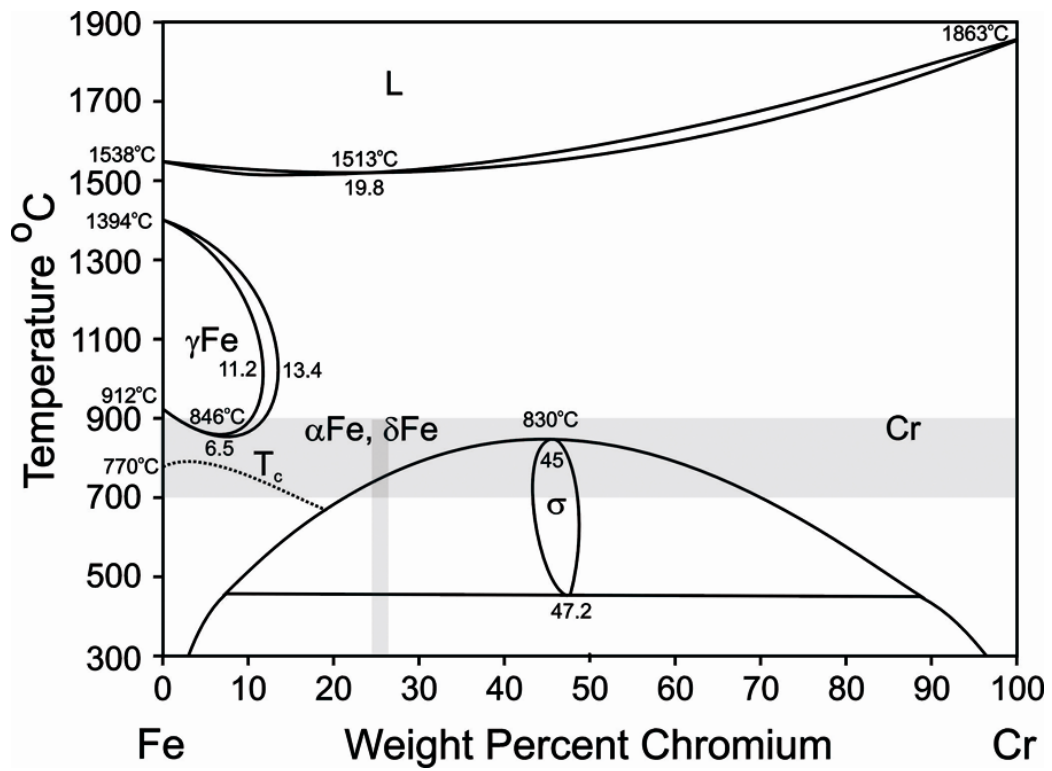
Figure 31. The Fe-Cr phase diagram showing regions in which σ-phase can form.
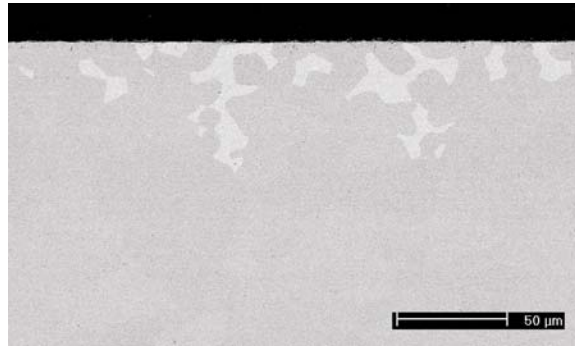
Figure 32.   Cross-section of 26 Cr Ferritic exposed at 700˚C in dry air for 2000 hours showing σ-phase only formed near the surface.
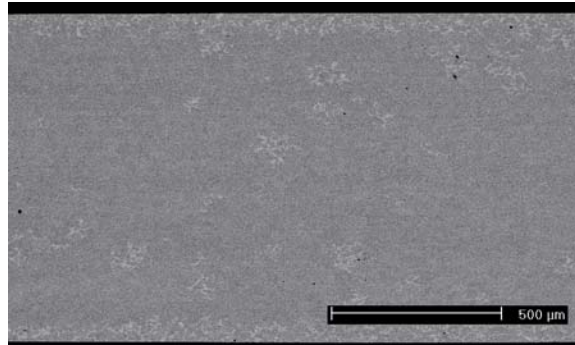
Figure 33.   Cross-section of 26 Cr Ferritic exposed at 700˚C in Ar/H$_2$/H$_2$O for 2000 hours showing σ-phase formed throughout the cross-section.
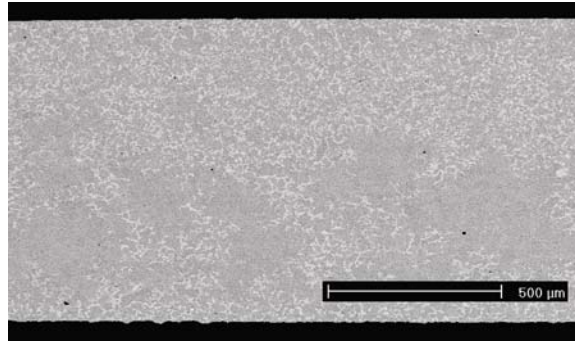
Figure 34.   Cross-section of 26 Cr Ferritic exposed at 700˚C in air + 0.1 atm H_2O for 2000 hours showing σ-phase formed throughout the cross-section.

APPENDIX B

Interfacial Fracture Testing to Evaluate the Durability of SOFC Interconnect Alloys

Nandhini Dhanaraj[1], Jack Beuth[1], Gerald Meier[2], Frederick Pettit[2], Julie Hammer[2] and Scot Laney[2]

[1]Department of Mechanical Engineering, Carnegie Mellon University, Pittsburgh, PA, 15213
[2] Department of Material Science and Engineering, University of Pittsburgh, Pittsburgh, PA, 15260

Keywords: Solid Oxide Fuel Cells, Interconnects, Indentation, Interfacial Fracture Toughness

Abstract

In this paper, fundamental thermo-mechanical aspects of the durability of solid oxide fuel cell (SOFC) interconnect alloys are investigated. A key failure mechanism for interconnects is the spallation of the chromia scale that forms on the alloy, as it is exposed to fuel cell environments. Indentation testing methods to measure the critical energy release rate (G_c) associated with the spallation of chromia scale/alloy systems are described, as are methods for analyzing the tests. Experimental results are then presented for the indentation of ferritic interconnect alloys with grown chromia scales. Results from specimens subjected to simulated SOFC environments are used to understand the mechanisms leading to scale spallation and the effects of different environments on scale/alloy durability. Results from short-term exposure indentation tests are related to results from longer-term exposure TGA experiments. This work forms the basis for understanding the interplay between chromia spallation and two other interconnect failure mechanisms.

Introduction

In order to perform its function, the optimal interconnect material for planar solid oxide fuel cells (SOFCs) should be impermeable to the anode and cathode gases, have high thermal conductivity, high electrical conductivity and good formability. Ferritic stainless steels, which have the above mentioned properties, have been identified as candidate materials for low temperature SOFC interconnects. Past studies have also shown that ferritic stainless steels have a better thermal expansion match with typical ceramic components of solid oxide fuel cells (SOFCs) than competing nickel-based alloys [1-3].

One of the major concerns associated with the successful operation of low temperature planar SOFCs is interconnect durability. The key factors affecting the life of interconnects are: (i) thickening of the chromia scale, which grows on the surfaces of the interconnect as it is exposed to the cathode and anode gases, leading to unacceptable electrical resistance levels; (ii) spallation of the chromia scale, leading to unacceptable increases in electrical resistance through the detached scale and alloy; and (iii) evaporation of the chromia scale where evaporated chromium can affect cathode function.

The problem of chromia evaporation associated with chromia forming alloys such as ferritic stainless steels, has been recognized and studied for many years [4]. Recent studies [1-3, 5] of chromia evaporation from SOFC interconnects have shown that the addition of elements like titanium and manganese to the ferritic interconnects can reduce evaporation. Coatings of $La_{0.9}Sr_{0.1}CrO_3$ have also been applied to ferritic alloys to limit CrO_3 evaporation [6]. Thickening of the chromia scale, leading to

increased resistance, has also been studied [1, 2] and it has been found that this problem can be controlled by the addition of elements like lanthanum, which tend to slow down the growth rate of chromia and also improve its adherence to the alloy substrate. Albeit the spallation problem has been considered from a metallurgical point of view, the mechanics of the adherence of chromia scales to interconnect alloys has not received widespread attention.

An accelerated testing protocol is presented in this paper to address the spallation issue. It involves performing indentation tests on specimens that are exposed to either simulated cathode gas (Air + 0.1 atm H_2O) or simulated anode gas (Ar/H_2/H_2O) environments for short time periods and using the results to predict long-term behavior. For the purposes of this paper, test results for a 26 Cr ferritic stainless steel exposed to the above mentioned environments at 900ºC are discussed.

Indentation Technique for Determining Chromia Scale Adhesion

Description of the Test

The indent test employed in this study was first proposed by Drory and Hutchinson [7] as a means for measuring interfacial toughness in brittle coating systems. It was then adapted for use on thermal barrier coating systems by Ma [8]. In this test, the specimen, which is typically a 16x5x1mm ferritic stainless steel wafer with an adherent chromia scale formed during cyclic exposure to either simulated cathode gas or anode gas, is placed in a Rockwell hardness tester. The specimen is indented in the tester using a brale C indenter.

A schematic diagram of the indentation process is shown in Figure 1. The chromia scale is penetrated by the indenter and the plastic deformation of the underlying substrate induces compressive radial strains in the substrate, away from the indent crater. This strain is transferred to the scale (the in-plane strains in the scale and substrate are matched at the interface) and the associated scale stress acts to drive the radial extension of an interface crack thereby inducing oxide scale debonding.
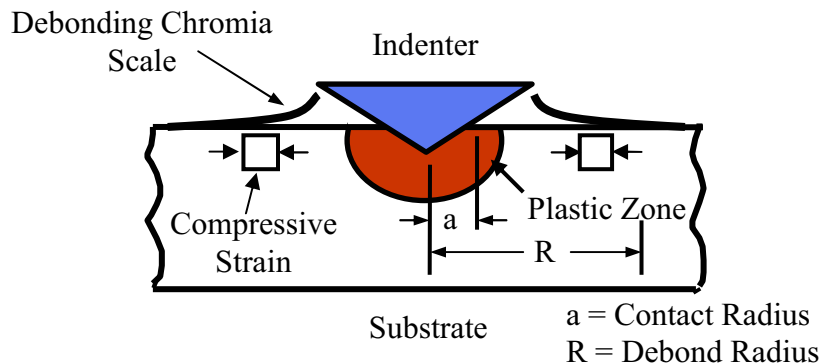
Figure 1 Schematic of the Indentation Test

Mechanics of Chromia Scale Spallation

The decoherence of a chromia scale from an interconnect alloy can be modeled as a fracture mechanics problem. Fracture mechanics principles require that a debond crack will grow along the oxide/alloy interface when $G=G_c$. The quantity G is the energy release rate, defined as the stored elastic energy in the scale that is released during debonding per unit newly created crack face area. G is the quantity driving debonding. G_c is the critical energy release rate, which can be treated as a property of the interface. G_c is the quantity resisting debonding. For the case of a residually stressed thin oxide scale on a thick substrate, the formula $G=G_c$ becomes:

$$\frac{\sigma^2 t(1-\nu)}{E} = G_c \quad , \tag{1}$$

where σ is the equal biaxial residual stress in the scale, t is the scale thickness, E is the scale elastic modulus and ν is the scale Poisson's ratio. In using this formula, it is assumed that the scale has completely spalled off, relaxing in-plane stresses and strains in both directions.

The chromia thickness is determined by the rates of diffusion of chromium and/or oxygen through the scale. The residual stress level in the scale is determined by stresses which arise during oxide formation (growth stresses), stresses produced during cool-down from elevated temperatures due to thermal expansion mismatch between the oxide and the alloy (thermal stresses), and any stress relaxation which may occur. In addition to equal biaxial residual stresses, stresses in the scale can also include uniaxial applied stresses from mechanical loading of the scale. The idea of the fracture testing described above is to increase the stress in the scale via mechanical loading, increasing the elastic energy stored in the scale and inducing spallation much earlier than it would normally occur.

Debond Behavior
The indentation test described above was performed on two sets of 26 Cr ferritic specimens with test loads of 60, 100 and 150 kg. Figures 2 and 3 show scanning electron microscope (SEM) images (viewed from above) of two indented specimens exposed to simulated cathode gas (SCG) and simulated anode gas (SAG), respectively. As indicated in Figs. 2 and 3, a change in the exposure environment greatly changes the debond behavior. The specimens exposed in simulated cathode gas (SCG) show a non-uniform flaking of the chromia scale in the near-indent region, with the density of the flaking decreasing with increasing distance from the center of the indentation (and decreasing energy release rate). This behavior suggests the presence of a non-uniform interfacial toughness and a scale that is easily broken up. In contrast, specimens exposed to simulated anode gas (SAG) show a more uniform peeling of an intact chromia scale. This debonding behavior is indicative of a more coherent scale and perhaps more uniform adhesion.
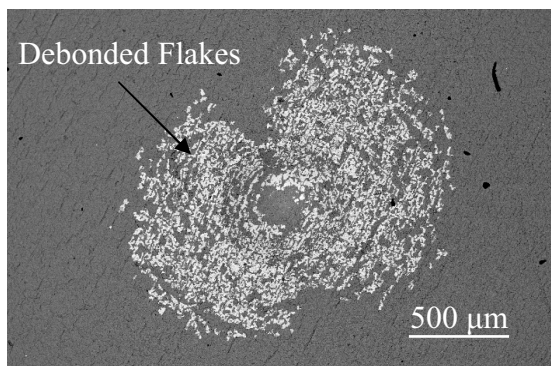
Figure 2 SEM Image of an Indented 26 Cr Ferritic Alloy Exposed to SCG at 900ºC for 100 hrs
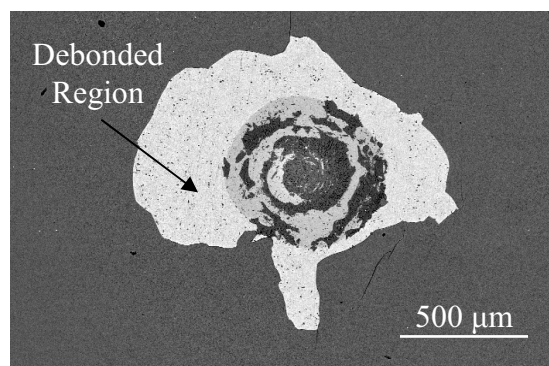
Figure 3 SEM Image of an Indented 26 Cr Ferritic Alloy Exposed to SAG at 900ºC for 264 hrs

These qualitative behaviors are consistent with long-term weight gain measurements on the same 26 Cr ferritic alloy (see Figure 4). For the SCG case, the specific weight measurements are nearly constant after 50 hrs of exposure. This is consistent with the idea that chromia evaporation may be limiting scale growth and/or that flaking of thicker or more weakly bonded portions of the scale is occurring. In contrast, for the SAG case, weight gains continue out to 2000 hrs of exposure. This is consistent with

there being less chromia evaporation and no flaking away of pieces of the chromia scale. Findings detailed in the section on experimental results also show essentially unchanging debond behavior for specimens exposed to SCG for 100 and 200 hrs (consistent with the steady-state specific weight data) and changing debond behavior for specimens exposed in SAG for 264 and 364 hrs (consistent with the weight gains seen in Figure 4 for this case).
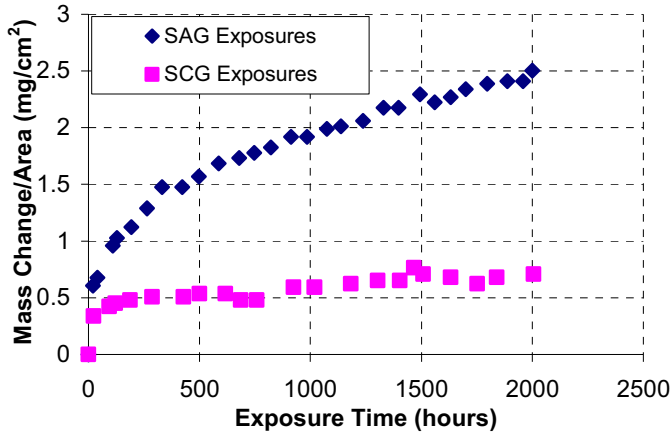

Figure 4 Specific Weight Gain Plots for the 26 Cr Ferritic Alloy Exposed to SAG and SCG at 900ºC
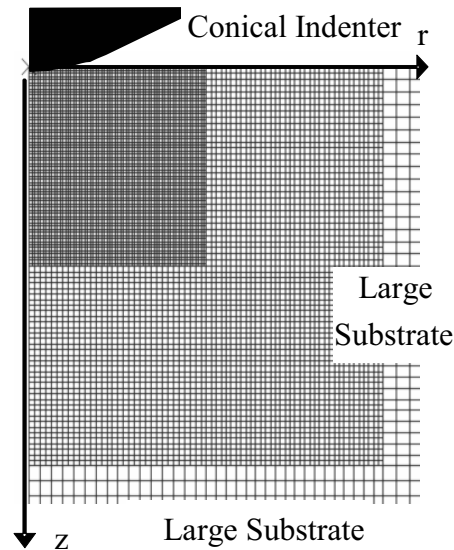
Figure 5 Typical Axisymmetric Finite Element Mesh Used in the Indentation Simulations

Analysis of the Test

Finite Element Model Description

The indentation test was simulated using the commercial finite element software ABAQUS. A 2-D axisymmetric model of an elastic-plastic substrate and a rigid indenter was used as shown in Figure 5. Two different sized substrates were studied, a large substrate model - large enough to experience strains and displacements identical to an infinitely large substrate and a typical SOFC test specimen model having a substrate radius of 8mm and a depth of 1mm. Surface strain results used in energy release rate calculations from these two types of models agreed, indicating that for indent loads up to 150kg, a 1mm thick SOFC specimen behaves like a large substrate. The rigid indenter was modeled to have an included angle and a tip radius identical to that of the actual conical indenter. The elastic-plastic behavior of the substrate was obtained from the stress-strain curve for the commercial alloy E-BRITE, a similar 26 Cr ferritic alloy with lower levels of Si.

The substrates were meshed with four-noded bilinear axisymmetric elements with a total of 12757 elements and 13058 nodes. The grid beneath the indenter was highly refined with element sizes ranging from 3-6 μm. In addition, elements were chosen to possess the characteristics of reduced integration and hybrid formulations, which help reduce run time and provide more accurate results in the near indent region, which is subjected to extensive plasticity and exhibits nearly incompressible behavior. The model is of the interconnect substrate, excluding the chromia scale on top. In the actual specimens, the chromia scale thickness is small compared to the size of the indentation strain field. As a result, the scale does not constrain the deformation of the substrate and a model excluding the scale is appropriate. In-plane substrate surface strains are transferred directly to the scale. Thus, in-plane surface strains from

the model are used within thin coating fracture mechanics formulas described in the next section to calculate energy release rate values.

Fracture Mechanics Calculations

The energy release rate, G, is calculated from the strains obtained from the top surface of the numerical indentation model. The equations used for G calculations were originally formulated for a single-layered coating system by Drory and Hutchinson [7]. The total radial strain, ε_r, and circumferential strain, ε_θ, in a single layered coating system can be calculated by combining a biaxial residual strain, ε_0, corresponding to the residual stress, with the strains obtained from the numerical indentation model, ε^n. The strains are given as

$$\varepsilon_r = \varepsilon_r^n + \varepsilon_o ; \qquad \varepsilon_\theta = \varepsilon_\theta^n + \varepsilon_o \quad , \tag{2}$$

where

$$\varepsilon_r^n = \frac{dU}{dr} ; \qquad \varepsilon_\theta^n = \frac{U}{r} \quad . \tag{3}$$

In eq (3), U is the radial displacement on the top surface of the substrate. Also the biaxial residual strain is given as

$$\varepsilon_o = \frac{\sigma_{oxide}(1 - \nu_{oxide})}{E_{oxide}} \quad . \tag{4}$$

The formula for calculating the critical energy release rate is given as:

$$G = \frac{1}{2(1 - \nu_{oxide}^2)} \left[E_{oxide} t_{oxide} (\varepsilon_r + \nu_{oxide} \varepsilon_\theta)^2 \right] \quad , \tag{5}$$

where it is assumed that only the radial stress and strain are released as the crack front extends in the radial direction.

In the above equations, E_{oxide}, t_{oxide} and ν_{oxide} are the Young's modulus, thickness and Poisson's ratio of the chromia scale and σ_{oxide} is the equal biaxial residual stress in the scale. Since the energy release rate, G, equals the critical energy release rate, G_c, resisting crack extension, the calculated G values in eq (5) yield G_c values in the tests. Because mechanical properties of chromia scales are not as readily available, as a first approximation the properties of an alumina scale have been used in the calculations. The thickness data were measured from cross section SEM images and residual stresses were obtained from x-ray diffraction (XRD) measurements performed at the University of Pittsburgh.

Indentation Test Analysis Results

The critical energy release rate, $G = G_c$, calculated from the simulation results is plotted against the radial distance, R, from the indenter normalized by the contact radius of the indenter, a (see Figure 1). Figure 6 shows such a plot for a large substrate model subjected to an indent load of 60 kg under frictionless conditions. The different curves represent different oxide thicknesses, with the lowermost curve corresponding to an oxide thickness of 0.25μm and the uppermost curve corresponding to a thickness of 4μm.
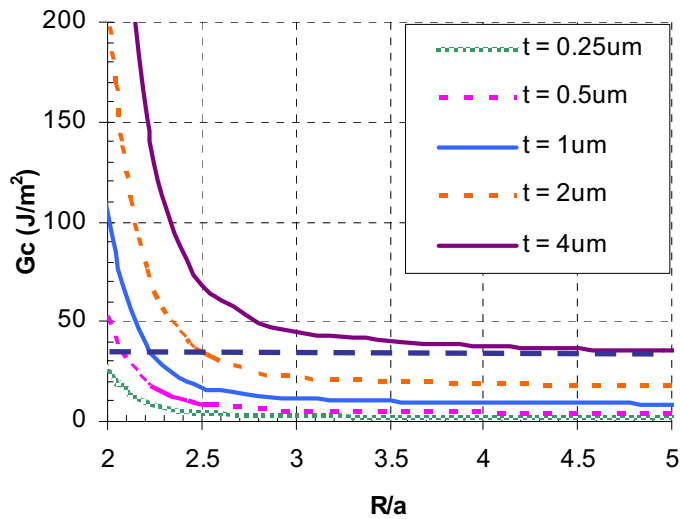
Figure 6 Simulation Results for a Large Substrate at
a Load of 60 kg under Frictionless Conditions

The plot shows G_c values which are large in the region close to the indent and trail off to constant values in the region far away from the indenter. The constant values of G_c away from the indenter correspond to the G due to residual strains only. Thus, for a given oxide thickness, spontaneous spallation occurs when the critical energy release rate reaches the minimum of the curve which corresponds to the energy release rate due to residual strains in the scale.

Indentation Test Experimental Results

SAG Exposed Specimens

As described in the earlier section, mechanical loading via indentation of the test specimen exposed to an SAG environment resulted in peeling of an intact chromia scale. The critical energy release rate associated with this type of debonding can be quantified by measuring the radial extent of the debond. Figure 7 shows an SEM image of the 26Cr ferritic alloy exposed to SAG for 264 hrs. The white region represents the debonded area and the dashed circle gives a rough estimate of the radius of the debond, R.
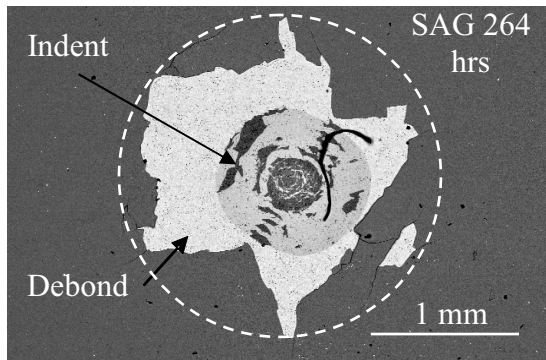

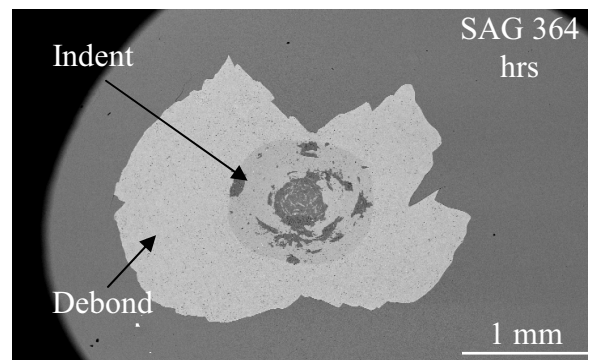Figure 7 SEM Image of an Indented Specimen
Exposed to SAG for 264 hrs

Figure 8 SEM Image of an Indented Specimen
Exposed to SAG for 364 hrs

In analyzing the debonded area, the important parameter is the ratio of the extent of debonding to the indent radius, R/a, which in the case of Figure 7 is approximately 2. Figure 8 shows an image from indentation of the same specimen, but after an exposure time of 364 hrs, with an approximate value of R/a = 2.5 (based on the maximum extent of debonding). From a fracture mechanics view point (as suggested by eq (1)) this increase in the extent of debonding could be due to an increase in the residual stress or loss of adhesion or scale thickening. The increasing weight gain exhibited by SAG-exposed specimens (Figure 4) suggests a growth in the oxide scale and thus part of the cause for extended debonding in the case of 364 hrs exposure compared to 264 hrs exposure is a thicker oxide scale.

A key concern associated with this type of visual quantification of the debond extent is that the oxide scale could be barely attached to the substrate but still appear bonded. To investigate this issue, a test specimen exposed to 464 hrs was indented using a 60 kg load and then tinted by exposing it at 700ºC for 10 minutes, followed by indentation at a higher load of 150 kg. Even though indentation at a higher load results in more extensive debonding compared to that at a lower load, the non-dimensional ratio of R/a remains unchanged. As can be seen from Figure 9, the process of tinting enables verification of the actual extent of debonding caused by the 60 kg load. The inner light gray region represents the debonded area from the indent load of 60 kg and the outer darker gray area is the debonded area from the indent load of 150 kg. The inner light gray area from the 60 kg indent has the same size and shape as what was observed immediately after the 60 kg indent was made. Because of this, it appears that observed debond sizes correlate well with the actual extent of scale debonding from the substrate.
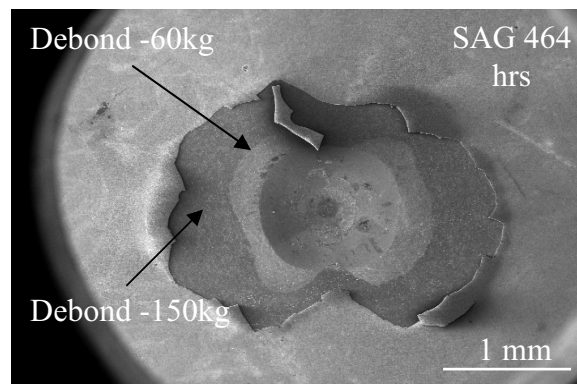

Figure 9 SEM Image Showing Debonding of
a Tinted Specimen, with an Inner, Lighter Gray
Region from a 60 kg Load and an Outer, Darker
Region from a 150 kg Load

The combined experimental and simulation results for G_c can be used to obtain a rough estimate of the exposure time at which spontaneous spallation will occur. In the case of a test specimen exposed for 364 hrs the maximum R/a was approximately 2.5, with an oxide scale thickness of approximately 2 μm (as obtained from cross section SEM thickness measurements). The corresponding critical energy release rate due to stresses induced by indentation and residual stress is found to be 34 J/m^2 as shown by the horizontal dashed line in Figure 6. Therefore, if for a given oxide scale thickness the energy release rate due to residual stress reaches a value of 34 J/m^2, spontaneous spallation would occur. From Figure 6 it can be seen that if the oxide thickness reaches a value of 4μm the energy release rate due to residual stresses only will reach this critical value. Cross section SEM measurements indicate that a 4 μm oxide thickness corresponds to an exposure time of 800 hrs, which suggests that the time to spontaneous spallation is approximately 800 hrs.

To test this prediction, indentation tests were performed on a specimen exposed for 822 hrs. As seen in Figure 10, out of the 3 indents, in 2 cases the debonding propagated across the specimen. Cross section images (Figure 11) revealed that the oxide scale was barely attached to the substrate, in which case any slight disturbance could cause the oxide scale to spall off. In fact, the detachment of the scale seen in Figure 11 is likely due to disturbance of the scale by the sectioning operation. Thus, indentation testing conducted at shorter exposure times has provided a good indication as to when to expect residual stress-induced spontaneous spallation.
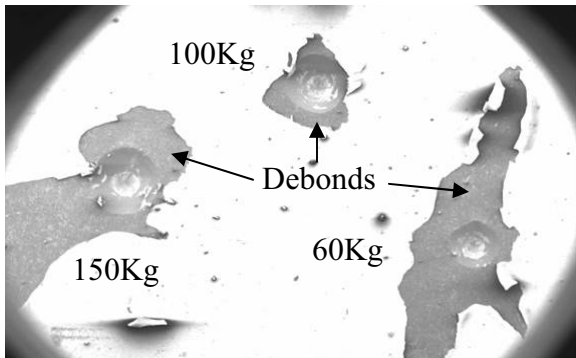

Figure 10 SEM Image of Indentation at Three Different Loads for an SAG Specimen Exposed for 822 hrs at 900ºC
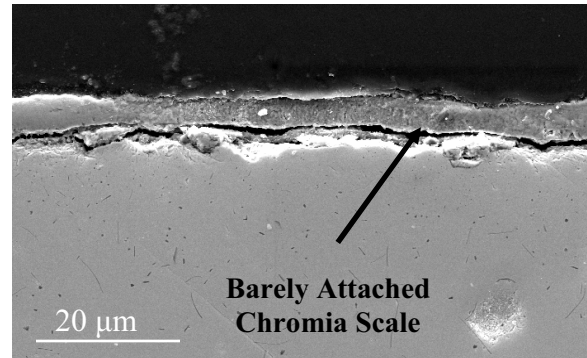

Figure 11 Cross Section SEM Image of SAG Specimen Exposed for 822 hrs at 900ºC

SCG Exposed Specimens

The non-uniform flaking of the oxide scale caused by the indentation of SCG-exposed specimens complicates the test analysis, as characterizing the adhesion by a single G_c value is no longer appropriate. Therefore, a methodology different from the one described for SAG-exposed specimens must be employed. An image analysis was formulated for this purpose, in which the debonded area outside the indent image was decomposed into three to seven concentric rings, with each ring having an average radius R as shown in Figure 12. A macro written in the image analysis software package SCION was used to obtain a percentage of debonded oxide scale in each ring. The percentage of debonded chromia scale was plotted for each ring against a normalized distance R/a, where a is the indent radius and R the average radius of the ring (see Figure 13).

The percentage debond plot suggests that the when R/a is small (close to the indent) the percentage of debonding is large and trails off with an increase in R/a. Also, the curves for 100 hrs and 200 hrs exposures (as indicated by 100 h and 200 h in the legend) are not very different, suggesting the attainment of a steady state with regard to susceptibility to debonding. The weight gain measurement plot Figure 4, shows that after approximately 50 hrs the weight gain curve for the SCG-exposed 26 Cr ferritic alloy reaches a more or less constant value. Two mechanisms can cause fracture behavior and specific weight measurements to reach a steady state. First, as the average scale thickness increases with exposure time, thicker or poorly bonded portions of the scale may spall, causing the average scale thickness to reach a steady state. Second, there is evidence to suggest that chromia evaporation, which can also reduce or eliminate scale thickening, can be significant in SCG environments. Fracture tests can yield insight into the role of the spallation mechanism in reaching a steady state.
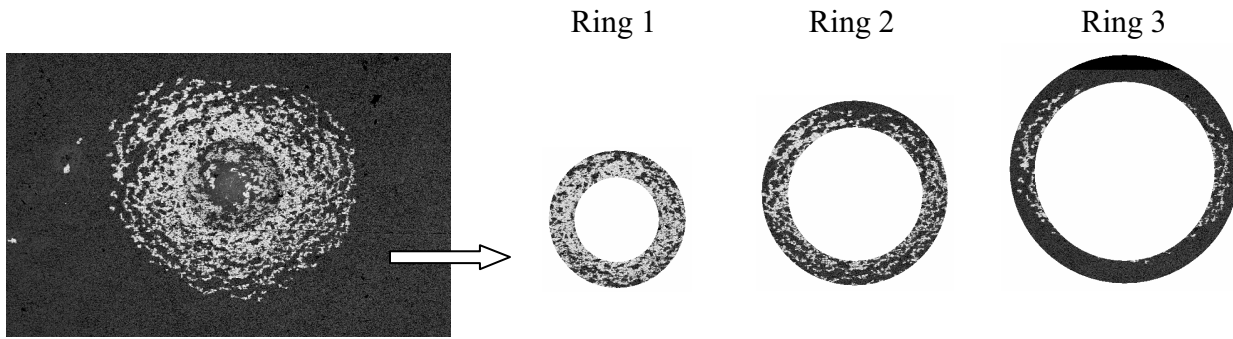
Figure 12 100 hr SCG Indent Image Decomposed into 3 Rings

Indentation tests on specimens subjected to a very short exposure time of 10 hrs have revealed initial debonding from compressive stress-induced shear cracks, as seen in Figure 14. Figure 13 shows percentage debond curves for the 10 hour exposure and the amount of debonding is significantly less compared to that at 100 and 200 hrs. It is planned to indent specimens exposed to up to 100 hrs to track the transition to steady state conditions.
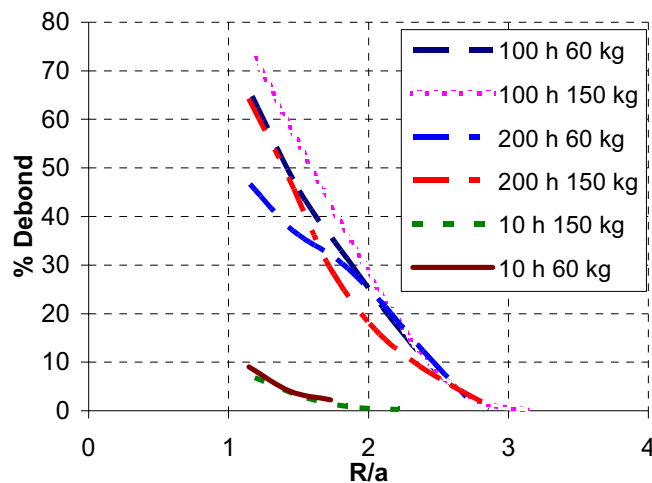

Figure 13 Percent Debond Plot for 10, 100 and 200 hour
SCG-Exposed Specimens Indented at 60 kg and 150 kg

Sensitivity of the image analysis could potentially influence the percentage debond results. In order to ensure that the image analysis would yield sensible results, the SEM image was studied qualitatively using EDS which confirmed that the white region in the image was indeed the debonded area (substrate) and the darker area was the bonded oxide scale. Since the pixel intensity was used to determine if a given pixel was bonded or debonded, as one gets close to the demarcation value, it gets harder to segregate them appropriately. For this purpose a sensitivity analysis was performed, in which a few pixel intensities close to the demarcation value were considered bonded in one case and debonded in the other. It was found that in both cases the percentage of debonding data was almost unaffected. The reason behind this is that the number of pixels with intensity values close to the demarcation value were on the order of 10-15, while the total number of pixels was in the order of thousands.
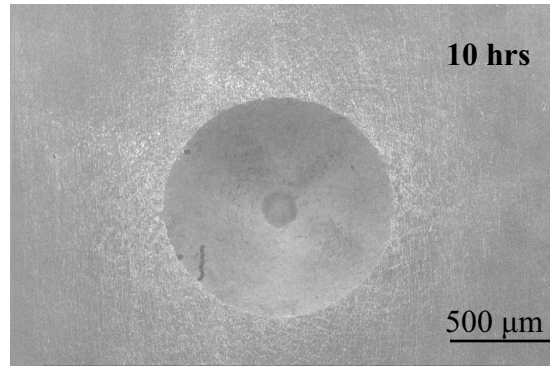
Figure 14 SEM Image of 10 hour SCG-Exposed Specimen
Showing Initial Debonding from Shear Cracks

Summary and Conclusions

The spallation of the chromia scale on interconnect alloys for planar solid oxide fuel cells has been modeled and analyzed as an interfacial fracture mechanics problem. An accelerated testing protocol employing indentation techniques has been established. Indentation tests performed on 26 Cr ferritic alloy test specimens exposed to short times in SAG and SCG environments at 900°C have indicated very different debond mechanics. The SAG-exposed specimens exhibited a peeling type debond of an intact chromia scale, while the SCG-exposed specimens exhibited a non-uniform flaking of the oxide scale. As a result, different techniques were employed to analyze specimens subjected to the two types of exposure environments.

The peeling type debond in SAG-exposed specimens was characterized by the extent of debonding and an estimate of the critical energy release rate associated with the debond was obtained from the numerical simulation results. It was found that for these specimens, although the weight gain measurements showed an increasing trend suggesting that the oxide scale was growing, accelerated testing revealed that mechanical failure was possible much earlier than the weight gain measurements suggested. Also, the mechanical testing gave an estimate of the thickness at which spontaneous spallation could occur. Cross-section SEM images were consistent with the indentation analysis in saying that mechanical failure is possible at an earlier time of just over 800 hrs, which was not obvious from the weight gain measurement data available up to 2000 hrs. Finally, the quantification of debond size based on a visual estimate of the extent of debonding from the SEM images was validated by employing a tinting technique.

In the case of SCG-exposed specimens, the non-uniform flaking of the oxide scale required a different analysis technique. An image analysis was performed to quantify the percentage of debonded area as a function of non-dimensional distance outside the indent. Results for 100 and 200 hrs exposures suggested that the radial distribution of debonding had reached a steady state, consistent with specific weight gain measurements. Experiments are underway to track the transition to this steady-state condition.

Chromia scale spallation is one of three potential failure mechanisms for fuel cell interconnects, the others being increased resistance from chromia scale growth and chromia evaporation. Changing the alloy system or exposure environment can cause a different mechanism to dominate, such that it is the

first to reach a critical value as exposure time is increased. The mechanisms are also coupled, where increased chromia scale growth also increases the likelihood of scale spallation, but increased chromia evaporation reduces the scale thickness and the likelihood of spallation. Overall, results from experiments to date suggest that scale spallation can be the dominant failure mechanism.

Acknowledgment

References

1. W. J. Quadakkers, T. Malkow, J. Pirón-Abellán, U. Flesch, V. Shemet, and L. Singheiser, "Suitability of Ferritic Steels for Application as Construction Materials for SOFC Interconnects," *Proc. Fourth European Solid Oxide Fuel Cell Forum*, A. J. McEvoy, ed., 2000, p. 827.
2. J. Pirón-Abellán, V. Shemet, F. Tietz, L. Singheiser, W. J. Quadakkers, and A. Gil, "Ferritic Steel Interconnect for Reduced Temperature SOFC," *Proc. Solid Oxide Fuel Cells VII*, H. Yokokawa and S. C. Singhal, eds., The Electrochem. Soc., 2001, p. 811.
3. W. J. Quadakkers, H. Greiner, and W. Köck, "Metals and Alloys for High Temperature SOFC Application," *Proc. First European Solid Oxide Fuel Cell Forum*, U. Bossel, ed., 1994, p. 525.
4. C. S. Tedmon, "The Effect of Oxide Volatilization on the Oxidation Kinetics of Cr and Fe-Cr Alloys," *J. Electrochem. Soc.*, 113, 1966, p. 766.
5. W. J. Quadakkers, H. Greiner, W. Köck, H. P Buchkremer, K. Hilpert, and D. Stöver, "The Chromium Base Metallic Bipolar plate – Fabrication, Corrosion and Cr Evaporation," *Proc. Second European Solid Oxide Fuel Cell Forum*, B. Thorstensen, ed., 1996, p. 297.
6. C. Gindorf, L. Singheiser, and K. Hilpert, "Determination of Chromium Vaporisation from Fe, Cr base Alloys Used as Interconnect in Fuel Cells (SOFC)," *Steel Research*, 72, 2001, p. 528.
7. M.D. Drory and J.W. Hutchinson, "Measurement of the Adhesion of a Brittle Film on a Ductile Substrate by Indentation," *Proc R Soc. London,* 452, 1996, p. 2319.
8. Q. Ma, *Indentation Methods for Adhesion Measurement in Thermal Barrier Coating Systems*, Ph.D. Thesis, Carnegie Mellon University, 2004.